

Internal and external colloidal anisotropy: pair interactions, sedimentation, and non-equilibrium lane formation

Von der Universität Bayreuth
zur Erlangung des Grades eines
Doktors der Naturwissenschaften (Dr. rer. nat.)
genehmigte Abhandlung

von

Thomas Geigenfeind

aus Burglengenfeld

1. Gutachter: Prof. Dr. Matthias Schmidt
2. Gutachter: Prof. Dr. Joachim Dzubiella

Tag der Einreichung: 19.06.2019
Tag des Kolloquiums: 08.10.2019

Abstract

This Thesis is devoted to the theoretical description of anisotropic effects in colloidal systems. We consider both internal anisotropy of the microscopic interactions between colloidal particles and external anisotropy originated from external fields [1–4].

First, we focus on internal anisotropy in hard body models in which the particles are not allowed to overlap. We investigate two-dimensional hard core systems with particles of arbitrary shape. The interaction between two hard particles is characterized by the excluded area, i.e. the area inaccessible to one particle due to the presence of another particle. The magnitude of the excluded area depends on the relative orientation between the two particles and it has a major impact on the bulk phase behaviour of a macroscopic system of hard particles. Using Principal Component Analysis we perform a statistical study of a large collection of excluded areas corresponding to randomly generated particle shapes. The study shows that the magnitude of the excluded area as a function of the relative particle orientation is dominated by global features of the particle shape such as the elongation of the particle. Hence, despite the vast diversity of particle shapes, the variety of possible excluded areas is more restricted. We identify limiting cases of particle shapes that form mesophases with different orientational symmetries. We complement the analysis with Monte Carlo simulations for selected particle shapes showing examples of the validity and the limitations of two-body Onsager-like theoretical approaches to describe hard core systems.

Anisotropy can also arise from external fields even if the interparticle interactions are isotropic. A prominent example is colloidal sedimentation, i.e. the equilibrium and migration of colloidal particles in a gravitational field. We develop a theory to study the effect of the height of the sedimentation test tube on the stacking sequence of binary colloidal mixtures. The stacking sequence is the sequence of macroscopic layers that appear under gravity in sedimentation-diffusion-equilibrium. We apply the theory to model binary mixtures and to mixtures of patchy colloids that differ either in the number or the types of patches. Patchy colloids are colloidal particles with anisotropic valence-based bonding interactions. We show that the height of the sample can change the stacking sequence of a colloidal mixture even if all other parameters such as the relative concentrations are fixed. For example, there can be stacking sequences that only appear for certain sample heights. We demonstrate that the sample height, which is often not systematically varied in experimental work, is an important parameter in sedimentation.

Besides the sedimentation-diffusion-equilibrium of colloidal mixtures we also consider the dynamics of sedimentation. We investigate an oppositely driven binary colloidal mixture in which two species migrate through each other. We identify three states depending on the driving strength. If the driving strength is low, then the two species diffuse through each other without any ordering effects. At sufficiently high driving strength, however, the two species demix and form dynamic lanes along the direction of the driving. For intermediate driving strengths the two species can block each other and form a quasi-static jammed state. Using Brownian dynamics simulations, we sample all the contributions to the one-body force field due to the internal interactions, the external fields, and the thermal diffusion. Of particular interest is the internal force field, which we split into adiabatic

and superadiabatic contributions. The adiabatic contribution is obtained by sampling a reference equilibrium system with the same one-body density as the non-equilibrium system. We demonstrate that laning is a purely superadiabatic effect and identify a species-dependent structural superadiabatic force that counteracts the entropy of mixing of both species. In addition, we develop a Power Functional Theory based on a velocity gradient approximation that reproduces the observed phenomenology.

As a practical example of self-assembly in a non-equilibrium colloidal system with both internal and external anisotropy we consider a system of patchy colloids with three patches adsorbed on a surface patterned with a square lattice of external potential wells. We investigate the effect of the width of the potential wells on the relaxation of a homogeneous state of patchy colloids. A competition between the potential energy of the cores, which is minimized if the particles aggregate in close packing near the centers of the potential wells, and the bonding energy of the patches, which is minimized if open networks with low packing fraction are formed, determines the dynamics of the system. For very narrow potential wells a close packed structure with six-fold symmetry is formed, whereas for wide potential wells the three-fold symmetry of the bonding sites of the patchy colloids leads to the formation of an open network. For intermediate widths a core-shell structure with a six-fold core and a three-fold shell appears. The relaxation times associated with the formation of both structures are significantly different, which can be used to dynamically control the self-assembly.

Kurzfassung

Diese Dissertation befasst sich mit der theoretischen Beschreibung von anisotropen Effekten in kolloidalen Systemen. Dabei werden sowohl interne Anisotropie der mikroskopischen Wechselwirkungen zwischen kolloidalen Teilchen, als auch von externen Feldern generierte externe Anisotropie betrachtet [1–4].

Zunächst wird interne Anisotropie in harten Modellen, in denen die Teilchen nicht überlappen können, untersucht. Es werden zweidimensionale harte Systeme mit Teilchen beliebiger Form betrachtet. Die Wechselwirkung zwischen zwei harten Teilchen ist charakterisiert durch die ausgeschlossene Fläche, d.h. die Fläche, die für ein Teilchen aufgrund der Anwesenheit des anderen Teilchens nicht zugänglich ist. Der Betrag dieser Fläche hängt von der relativen Orientierung beider Teilchen ab und hat für makroskopische harte Systeme großen Einfluss auf das Phasenverhalten im Volumen. Mit Hilfe von *Principal Component Analysis* erfolgt eine statistische Auswertung einer großen Anzahl an zufällig generierten Teilchenformen gehörigen ausgeschlossenen Flächen. Die Auswertung zeigt, dass die funktionelle Abhängigkeit des Betrags der ausgeschlossenen Fläche von der relativen Teilchenorientierung von globalen Eigenschaften der Teilchenform, wie beispielsweise der Elongation des Teilchens, dominiert wird. Folglich ist die Vielfältigkeit möglicher ausgeschlossener Flächen trotz der hohen Diversität an Teilchenformen eingeschränkt. Es werden Grenzfälle von Teilchenformen, die Mesophasen mit verschiedenen Orientierungssymmetrien bilden, identifiziert. Die Analyse wird ergänzt mit Monte Carlo-Simulationen ausgewählter Teilchenformen. Dabei werden Beispiele gezeigt, welche die Gültigkeit und Grenzen von theoretischen Onsager-ähnlichen Zweiteilchenansätzen zur Beschreibung von harten Systemen demonstrieren.

Anisotropie kann auch durch externe Felder erzeugt werden, selbst wenn die internen Wechselwirkungen isotrop sind. Ein zentrales Beispiel hierfür ist kolloidale Sedimentation, d.h. das Gleichgewicht oder die Migration von kolloidalen Teilchen in einem Gravitationsfeld. Es wird eine Theorie entwickelt um den Effekt der Probenhöhe auf die Stapelfolge von binären kolloidalen Mischungen zu untersuchen. Die Stapelfolge ist die Abfolge von makroskopischen Schichten, die sich unter dem Einfluss von Gravitation im Sedimentations-Diffusions-Gleichgewicht ausbilden. Die Theorie wird angewandt auf binäre Modellmischungen und auf Mischungen von Patch-Kolloiden, welche sich entweder in der Zahl oder den Typen von Patches unterscheiden. Patch-Kolloide sind kolloidale Teilchen mit anisotropen valenz-basierten Bindungswechselwirkungen. Es wird demonstriert, dass die Probenhöhe die Stapelfolge verändern kann, selbst wenn alle anderen Parameter wie beispielsweise die relativen Konzentrationen unverändert sind. So können zum Beispiel manche Stapelfolgen nur für bestimmte Probenhöhen auftreten. Es wird gezeigt, dass die Probenhöhe, welche in experimentellen Arbeiten oft nicht systematisch variiert wird, ein wichtiger Parameter der Sedimentation sind.

Neben dem Sedimentations-Diffusions-Gleichgewicht von kolloidalen Mischungen wird auch die Dynamik von Sedimentation betrachtet. Eine in entgegengesetzte Richtungen angetriebene binäre kolloidale Mischung, in der sich die beiden Spezies durcheinander bewegen, wird untersucht. Es werden drei Zustände abhängig von der Antriebsstärke identifiziert. Wenn der Antrieb gering ist, diffundieren die beiden Spezies durcheinander ohne Ord-

nungseffekte. Bei ausreichend hoher Antriebsstärke entmischen die beiden Spezies und formen dynamisches Spuren entlang der Richtung des Antriebs. Für mittlere Antriebsstärke können sich die Spezies gegenseitig blockieren und einen quasi-statischen blockierten Zustand (*"jammed state"*) bilden. Mit Hilfe von Brownscher Dynamik-Simulationen werden sämtliche Beiträge zum Einteilchenkraftfeld, welche von internen Wechselwirkungen, externen Feldern und thermischer Diffusion stammen, gesamlet. Von besonderem Interesse ist dabei das interne Kraftfeld, welches in adiabatische und superadiabatische Beiträge aufgespalten wird. Der adiabatische Beitrag wird erhalten, indem ein Referenzgleichgewichtssystem mit derselben Einteilchendichte wie das Nichtgleichgewichtssystem gesamlet wird. Es wird demonstriert, dass Spurbildung ein rein superadiabatischer Effekt ist und eine speziesabhängige strukturelle superadiabatische Kraft, die der Mischungsentropie beider Spezies entgegenwirkt, wird identifiziert. Zusätzlich wird eine Powerfunktionaltheorie, welche eine Approximation basierend auf dem Gradienten des Geschwindigkeitsfeldes beinhaltet und die beobachteten Phänomene reproduziert, entwickelt.

Als eine praktische Anwendung von Selbstorganisation in einem Nichtgleichgewichtssystem, das sowohl interne als auch externe Anisotropie beinhaltet, wird ein System von Patch-Kolloiden, die an eine Oberfläche mit gitterförmig angeordneten externen Potentialtöpfen adsorbiert sind, untersucht. Betrachtet wird der Effekt der Breite der Potentialtöpfe auf die Relaxation eines homogenen Zustands der Patch-Kolloiden. Ein Wettbewerb zwischen der potentiellen Energie der Kerne, welche minimal ist, wenn sich die Teilchen dichtgepackt nahe den Zentren der Potentialtöpfe anordnen, und der Bindungsenergie der Patches, welche minimal ist, wenn sich offene Netzwerke mit geringer Packungsdichte bilden, kennzeichnet die Dynamik des Systems. Für sehr enge Potentialtöpfe bildet sich eine dichtgepackte Struktur mit sechszähliger Symmetrie, wohingegen für breite Potentialtöpfe die dreizählige Symmetrie der Bindungsstellen der Patch-Kolloiden zur Bildung eines offenen Netzwerks führt. Für mittlere Breiten formiert sich eine Kern-Schale-Struktur mit sechszähligem Kern und dreizähliger Schale. Die Relaxationszeiten der Bildung beider Strukturen sind signifikant unterschiedlich, was genutzt werden kann, um die Selbstorganisation dynamisch zu kontrollieren.

Contents

Abstract	3
Kurzfassung	5
1 Introduction	9
1.1 Colloidal particles	9
1.1.1 Internal anisotropy	10
Particle shape	10
Patchy colloids	10
1.1.2 External anisotropy	12
Sedimentation of colloidal particles	13
Opposite driving in colloidal mixtures	13
1.2 Theoretical approaches and simulation techniques in Brownian systems . . .	16
1.2.1 Langevin and Brownian dynamics	16
1.2.2 Monte Carlo simulation	17
1.2.3 Smoluchowski equation	18
1.2.4 Density functional and power functional theories	18
1.2.5 Sedimentation-diffusion-equilibrium of binary colloidal mixtures . . .	22
1.2.6 Wertheim theory and percolation	24
1.2.7 Excluded volume and Onsager theory	26
1.2.8 Principal component analysis	28
2 Overview of the publications	31
2.1 Principal Component Analysis of the excluded area of two-dimensional hard particles	31
2.2 The role of sample height in the stacking diagram of colloidal mixtures under gravity	33
2.3 Superadiabatic demixing in nonequilibrium colloids	34
2.4 Crossover from three- to six-fold symmetry of colloidal aggregates in circular traps	34
2.5 Author contributions	36
References	37
3 Publications	41
3.1 Principal Component Analysis of the excluded area of two-dimensional hard particles	43
3.2 The role of sample height in the stacking diagram of colloidal mixtures under gravity	55
3.3 Superadiabatic demixing in nonequilibrium colloids	67
3.4 Crossover from three- to six-fold symmetry of colloidal aggregates in circular traps	83

1 Introduction

This Thesis addresses the behaviour of colloidal systems in which large numbers of nano- to micron-sized particles self-assemble into complex structures and patterns. We investigate how this self-assembly is influenced and promoted by different forms of anisotropy. Both anisotropy of the microscopic interactions between colloidal particles (internal anisotropy) and anisotropy that originates from external fields (external anisotropy) are considered.

In this introductory chapter the phenomenology in colloidal systems relevant to this Thesis is first presented, followed by the general methods and tools required for the theoretical description and for the computer simulation of the investigated model systems.

1.1 Colloidal particles

Colloids consist of small particles dispersed in a solvent like water or oil. The suspended particles, called colloidal particles, are of mesoscopic size, typically on the scale of several nano- to micrometers. Colloidal systems are ubiquitous in our daily lives. Prominent examples are milk, gelatin, blood, toothpaste, and paint [5–8].

A characteristic feature of colloids is Brownian motion. This phenomenon was originally described by Robert Brown in 1827 who noticed that pollen grains suspended in water perform random motion. In the early 20th century, Einstein and Sutherland found the origin of this motion in the interaction between molecules of the fluid and the pollen grains [9, 10]. The molecules of the solvent are in constant motion and collide with the colloidal particles, exerting on them at each point in time a random net force. This leads to a random walk of the suspended particles through the solvent known as Brownian motion.

Colloids can self-assemble into complex structures with utilization in technological applications. Examples are conductive ink [11], nanodiodes [12], and photonic crystals [13]. The electro-optical applications make use of the fact that colloids can form regular structures on a lengthscale at which visible light is diffracted. A natural example for this effect can be observed in opals, where small regions of regularly arranged silica particles create a beautiful play of colors [14]. Structures on the colloidal lengthscale can also be found in our bodies. For example, the transport of nutrients and chemical agents within body fluids depends on the fundamental properties of colloids. Hence, colloidal research is vital for medical applications such as drug delivery [15].

Colloidal particles are generally large and slow enough to be observed via optical microscopy. For this reason, colloids are used to model and understand other systems. For example, the mechanisms of protein assembly [16] that occur at the molecular lengthscale can be partially understood by studying colloidal systems. In contrast, insights from colloidal research can also be applied to large-scale systems. In this Thesis, for example, we study lane formation in a colloidal model system, a phenomenon that can also be observed in e.g. a dense group of pedestrians [17].

1.1.1 Internal anisotropy

The description of colloidal systems can be greatly simplified if the interaction between the particles is isotropic and hence depends only on the distance between the particle centers. Theoretical models for isotropic interactions such as the hard sphere model and the Lennard-Jones potential have great historical relevance and are to this day an active topic of research. These models already include an abundance of interesting phenomena. One central example is the freezing of the hard sphere fluid presented in 1957 by Alder and Wainwright [18]. This constitutes a purely entropically driven first order phase transition in which the particles assemble into a regular lattice.

However, the complexity of the structures formed by isotropic colloids cannot in general match the intricacy of configurations found at the molecular level, for example those formed by proteins. Yet, the variety of configurations increases drastically when colloidal particles with anisotropic interactions are considered. In this Thesis we examine systems with two types of internal anisotropy, as laid out in the following.

Particle shape

In Ref. [1] we investigate the effect of anisotropic particle shapes on the bulk equilibrium properties of 2D hard core systems. Studies of this topic are of prevailing experimental relevance, since recent experimental advances have allowed the synthesis of colloidal particles with arbitrary shapes using techniques such as photolithography [19,20]. Microscope images of colloidal particles with distinct shapes are presented in Fig. 1.1. Those images demonstrate the variety and precision with which the shape of colloidal particles can be controlled.

Colloidal particles with anisotropic shape possess not only positional, but also orientational degrees of freedom. This gives rise to new physics, such as the formation of mesophases with orientational order. Representative states of hard spherocylinders with sufficiently high aspect ratio are shown in Fig. 1.2. By increasing the density the particles undergo first an isotropic-nematic transition [21]. In the nematic state the particles are on average aligned along a preferred orientation, called the director [22]. However, the particles have no positional order. A further increase of the density leads to the formation of a smectic state with both orientational order and positional order in one dimension, as shown in Fig. 1.2c.

Substances that form this type of mesophases are known as liquid crystals to designate materials with properties intermediate between those of a crystal and of an isotropic liquid. A brief introduction to the theoretical description of such ordering effects is given in Sec. 1.2.7.

Patchy colloids

Anisotropy in the interactions between colloidal particles can also be introduced via directional bonding. Patchy colloids are nano- to micron-sized particles made of a hard core with discrete attractive sites, called patches, on the surface [23]. Originally, patchy particles were introduced as a theoretical concept in order to study the behaviour of molecules with highly anisotropic interactions [24,25]. The hydrogen bond is a prototypical example for such directional interactions. Advances in synthesis techniques have made the experimental realization of patchy colloids possible [26]. Due to their similarity with the directional interactions of particles at molecular lengthscales, patchy colloids are also re-

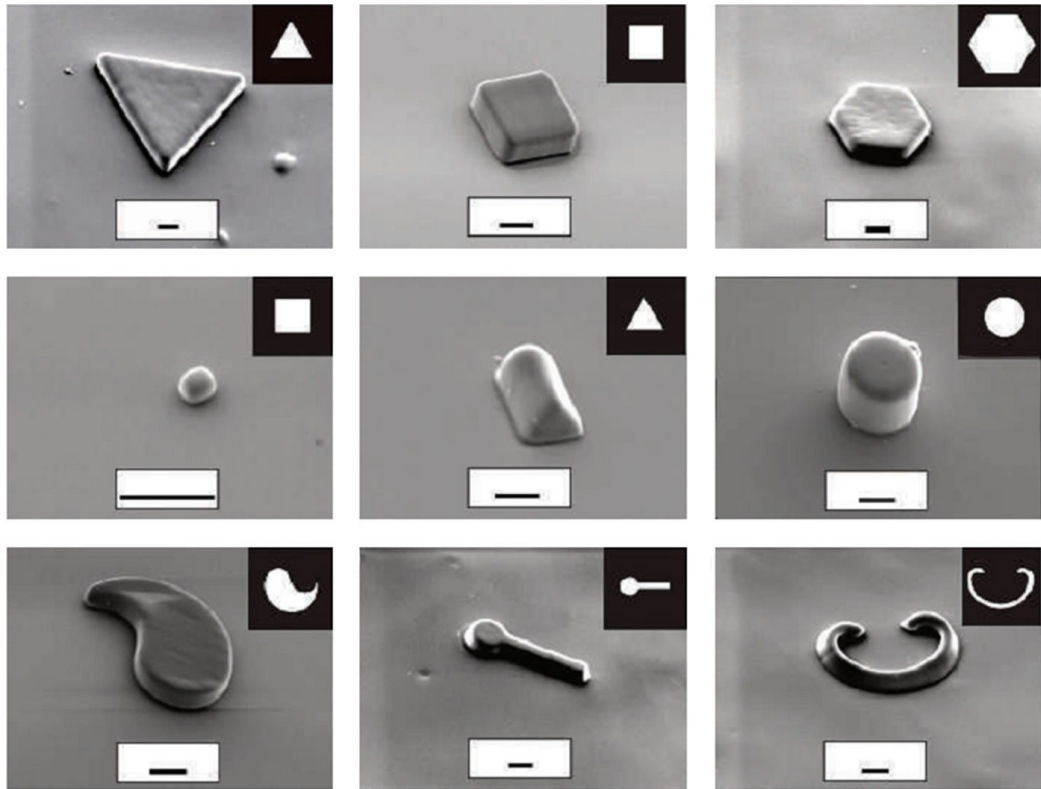


Figure 1.1: Scanning electron microscope images of anisotropic colloidal particles created with photolithography. Scale bars are $10\ \mu\text{m}$ long. Adapted from Ref. [19].

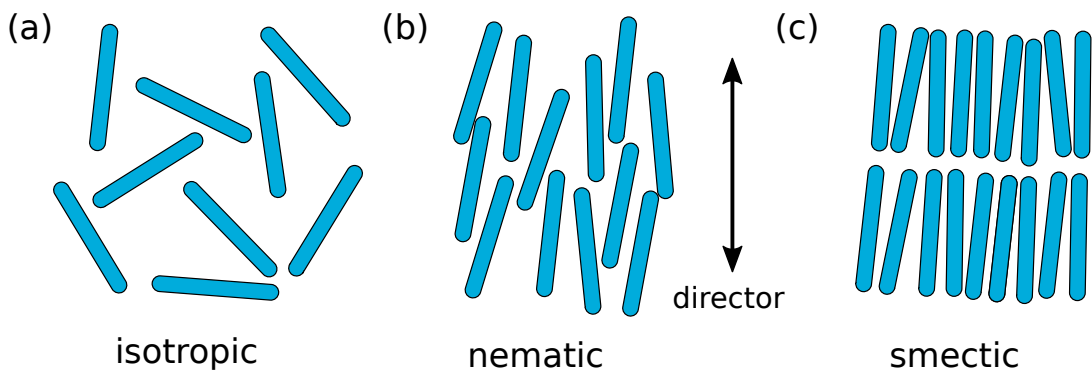


Figure 1.2: Schematic representations of hard spherocylinders in three different states. (a) Isotropic state at low density with neither positional nor orientational order. (b) Nematic state at intermediate densities. The particles have no positional order, but are on average oriented along the director. (c) Smectic state at high densities with both orientational and one-dimensional positional order.

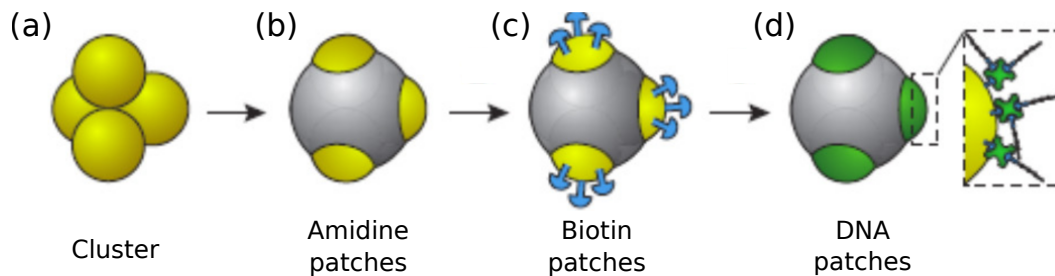


Figure 1.3: Schematic of the synthesis of patchy colloids using droplet polymerization. (a) A cluster of amidinated polystyrene microspheres with tetrahedral configuration. (b) Adding and polymerizing a styrene droplet creates the hard core of the patchy colloid. The parts of the microspheres that are not covered by the core act as amidine patches. (c) Preparation of the patches with biotin. (d) Adding DNA molecules with single stranded ends creates highly selective patches. Adapted from Ref. [31].

ferred to as colloidal molecules [27]. Today, there exist several methods for synthesizing patchy colloids [28–30]. One widely used technique is schematically shown in Fig. 1.3.

One starts with colloidal amidinated polystyrene microspheres that are attached to liquid emulsion droplets [31]. Emulsion evaporation, i.e. removing the fluid, leads to a shrinking of the droplets and therefore packing of the microspheres into clusters. In order to minimize the interfacial free energy [32], these clusters form defined structures such as tetrahedra [33], see Fig. 1.3a. Then, styrene monomer is added to the clusters. The monomer forms a spherical droplet around the clusters. Via polymerization, the droplet is turned into the spherical core of the patchy colloid, Fig. 1.3b. The size of the core is such that only the outmost parts of the monosphere cluster remain outside and form the patches. Preparation with biotin, Fig. 1.3c, allows then the attachment of DNA molecules, Fig. 1.3d. Typically, double stranded DNA molecules with single stranded ends are used. The sticky ends of the DNA molecules only bind to the complementary DNA molecules of other patches, which results in highly selective patchy interactions.

The phase behaviour of patchy colloids is determined by a competition between the free energy of the bonding of the patches and the free energy of the configurations of the cores. We discuss this in detail in Ref. [4], where we study the relaxation of patchy colloids adsorbed to a surface which is patterned with potential wells. In addition, in Ref. [2] we study the sedimentation-diffusion-equilibrium of binary mixtures of patchy colloids. Relevant parameters for patchy colloidal systems are the bonding energy, i.e. the change in internal energy when two patches form a bond, as well as the number of patches per particle, called the functionality. An introduction to the theoretical description of patchy colloids is given in Sec. 1.2.6.

1.1.2 External anisotropy

Colloidal particles might respond to different types of external fields, such as magnetic or electric fields. The external fields can be time-dependent and experimentally controlled. Even if no external fields are applied intentionally, experiments in colloidal science are in general influenced by the Earth’s gravitational field. Anisotropic external fields can break the global rotational symmetry of a bulk system and create macroscopically ordered structures, even if the internal interactions are isotropic. Constant driving with an ex-

ternal field keeps a system in a perpetual state of non-equilibrium. There, even a simple homogenous external force leads to complex patterns, as we demonstrate in Ref. [3].

Sedimentation of colloidal particles

Sedimentation is the equilibrium or migration of colloidal particles in a gravitational field. Although usually negligible on the molecular lengthscale, in colloidal systems sedimentation effects can be commonly observed because the gravitational energy of particles can be comparable to their thermal energy [34]. This is often expressed in terms of the gravitational length

$$\xi = \frac{k_B T}{mg}, \quad (1.1)$$

where k_B denotes the Boltzmann constant, T the absolute temperature, m the buoyant mass of one particle, and g the acceleration due to gravity. For colloidal systems, gravitational lengths typically are of the order of millimeters to centimeters. If experimentally preferable, gravitational effects can be increased using centrifuges.

In addition to the interest in sedimentation experiments due to technical applications such as using centrifugation as a separation technique [35], sedimentation experiments allow access to fundamental properties of colloids. Famous examples are the experiments by Perrin in 1916, which included the measurement of the Boltzmann constant [36], as well as the test of the bulk equation of state of hard spheres by Piazza et. al. in 1993 [37].

When colloidal mixtures are considered, the sedimentation-diffusion-equilibrium can be quite complex and can include the formation of multiple stacks [38] as well as counter-intuitive effects such as denser particles floating on top of lighter ones [39].

As an example we show in Fig. 1.4 photographs of a sedimentation experiment with mixtures of colloidal gibbsite platelets and silica spheres. Changing the size of the spheres completely alters the stacking sequence, i.e. the sequence of stacks of different layers that appear under gravity. For small spheres a nematic phase at the bottom with an isotropic one on top is found in sedimentation-diffusion-equilibrium. This sequence changes to a nematic phase floating between two isotropic phases for the case of bigger spheres [40].

In Ref. [2] we develop a theory for the sedimentation-diffusion-equilibrium of binary colloidal mixtures in vessels with finite height based on the theory of sedimentation paths for infinite vessels [41, 42], which is introduced in Sec. 1.2.5 .

Opposite driving in colloidal mixtures

Specific phenomena arise when the two species of a binary colloidal mixture are driven through each other in opposite directions. Such driving occurs for example when oppositely charged particles are subject to a homogenous electric field and also in the case of particles with different buoyant masses in a gravitational field. The driving can also originate from self-propelling with aligned velocities such as e.g. for bacteria in channels [43, 44].

Two characteristic states in a system of oppositely charged polymethylmethacrylate (PMMA) spheres subject to a homogenous electric field [45] are presented in Fig. 1.5. For high density and intermediate driving strength, the two species block each other and form a jammed state as shown in Fig. 1.5a. In this state the two species segregate and form bands perpendicular to the driving force in which the individual particles are almost static. In contrast, for intermediate densities and strong driving there is the so-called lane formation, see Fig. 1.5b. Here, the two species form lanes along the direction of the driving in which the particles are highly dynamic.

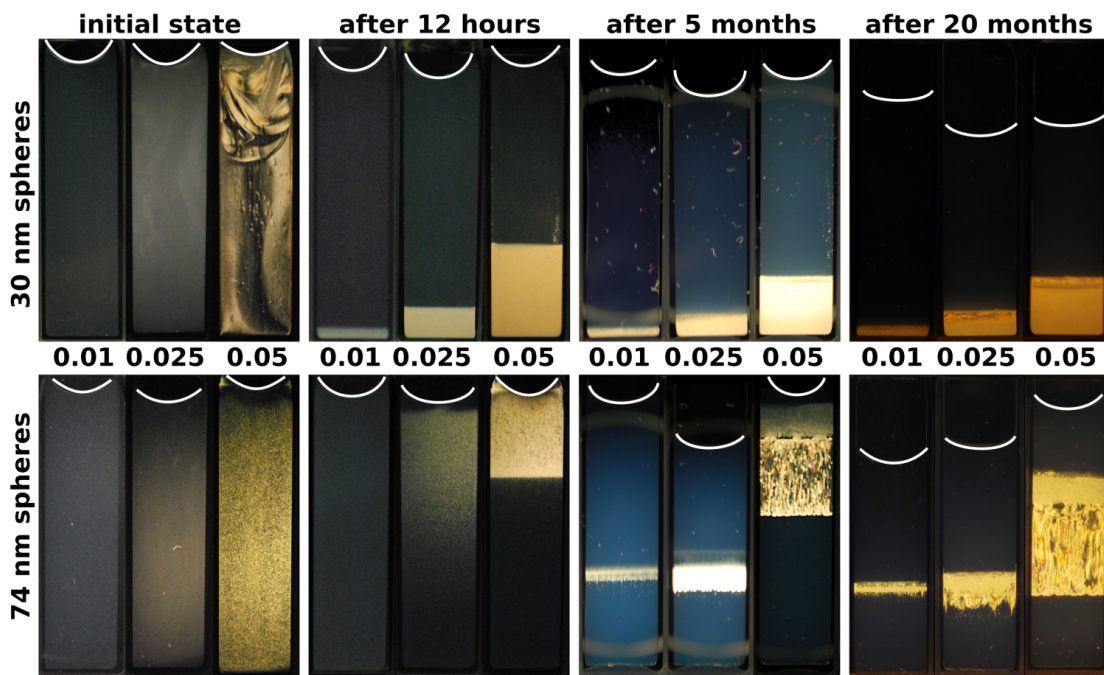


Figure 1.4: Photographs taken between crossed polarizers showing the time-evolution of samples in a sedimentation experiment with colloidal mixtures of gibbsite platelets (diameter of 186 nm) and silica spheres with diameters of 30 nm (top row) and 74 nm (bottom row). The initial bare packing fraction of the spheres is 0.05, and for the platelets 0.01, 0.025, and 0.05, as indicated. Changing the size of the spheres completely modifies the stacking sequence in sedimentation-diffusion-equilibrium from bottom nematic (orange) and top isotropic (black) in the case of small spheres (top right panel) to a nematic phase floating between two isotropic phases in the case of big spheres (bottom right). From Ref. [40].

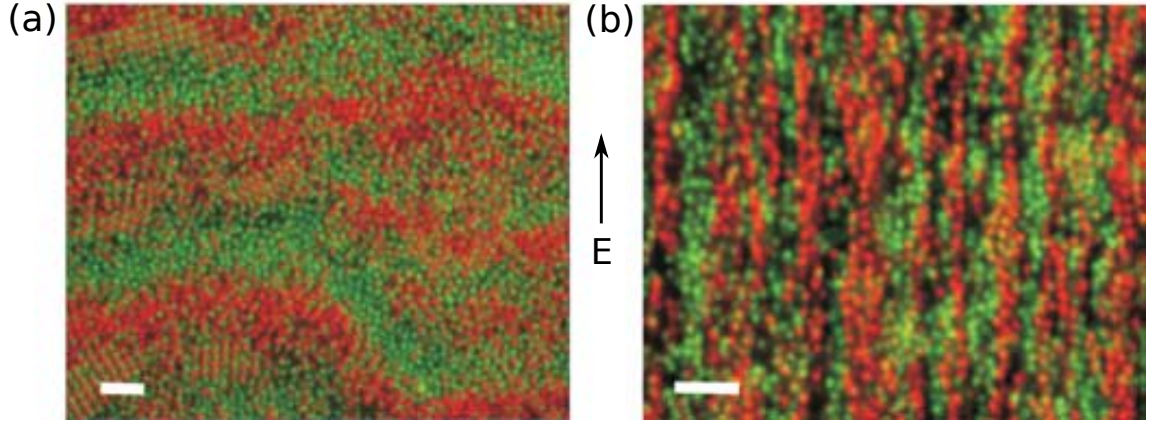


Figure 1.5: Confocal snapshots of a binary mixture of PMMA spheres with opposite charges (indicated by green and red color). In both panels a homogenous and static electric field \mathbf{E} in the direction indicated by the arrow is applied. (a) At very high density and intermediate field strength ($E = 20 \text{ Vmm}^{-1}$) the system is jammed and forms static bands perpendicular to the direction of the driving. (b) Dynamic lane formation with dynamic lanes along the direction of the driving at intermediate density and high field strength ($E = 80 \text{ Vmm}^{-1}$). In both panels the white scale bars are $10 \mu\text{m}$ long. Adapted from Ref. [45].

A particular property of lane formation is that it also appears in large-scale systems like pedestrian crowds [46, 47]. The research of lane formation in pedestrian crowds is of high importance for the planning of evacuation routes.

Many aspects of lane formation have been studied, for example the formation of tilted lanes when the driving is not opposite [48] and a reentrance effect in the formation of lanes that appears for increasing density [49]. For further details see also Ref. [3], where we study an oppositely driven binary colloidal mixture with computer simulations and theory. We focus on characterizing the contributions to the one-body force field in both the jammed state and the laned state.

1.2 Theoretical approaches and simulation techniques in Brownian systems

This section briefly introduces the concepts that provide the theoretical foundation for investigating and understanding the so far presented physical phenomena.

1.2.1 Langevin and Brownian dynamics

Langevin dynamics

Langevin dynamics is an approach for modeling the dynamics of colloidal systems. A system of N colloidal particles is considered at fixed temperature T and suspended in a solvent. The motion of the i -th colloidal particle is described by the Langevin equation

$$m_i \ddot{\mathbf{r}}_i(t) = \mathbf{f}_{\text{tot},i}(t) - \xi \dot{\mathbf{r}}_i(t) + \delta \mathbf{f}_i(t), \quad (1.2)$$

where m_i and \mathbf{r}_i are the buoyant mass and the position of particle i , ξ is the friction coefficient against the implicit solvent, and $\mathbf{f}_{\text{tot},i}$ denotes the total deterministic force acting on particle i , which originates from both internal interactions and external fields. The molecules of the solvent are not considered explicitly. However, the effect of the collisions between the solvent and the colloidal particles is included via a stochastic contribution, namely the random force $\delta \mathbf{f}_i$. This random force has zero mean, is uncorrelated between different particles, and has an infinitely short correlation time when acting on the same particle, i.e.

$$\langle \delta \mathbf{f}_i \rangle = 0, \quad (1.3)$$

$$\langle \delta \mathbf{f}_i(t) \delta \mathbf{f}_j(t') \rangle = 2\xi k_B T \delta_{ij} \delta(t - t') \mathbf{I}, \quad (1.4)$$

with Kronecker delta δ_{ij} , and $d \times d$ identity matrix \mathbf{I} , where d is the space dimension. Langevin dynamics does not consider hydrodynamic interactions between the particles, but includes friction via the term $-\xi \dot{\mathbf{r}}_i$.

Brownian dynamics

In the overdamped limit, inertial effects become negligible and one obtains from Langevin dynamics the simplified equations of motion of Brownian dynamics:

$$\xi \dot{\mathbf{r}}_i(t) = \mathbf{f}_{\text{tot},i}(t) + \delta \mathbf{f}_i(t). \quad (1.5)$$

In our simulations these equations are discretized and integrated in time via the standard Euler algorithm, i.e.

$$\mathbf{r}_i(t + \Delta t) = \mathbf{r}_i(t) + \frac{1}{\xi} \mathbf{f}_{\text{tot},i}(t) \Delta t + \delta \mathbf{r}_i(t), \quad (1.6)$$

where Δt denotes one discrete time step and $\delta \mathbf{r}_i$ is a random displacement sampled from a Gaussian distribution with zero mean and variance $\sqrt{2D\Delta t}$ with Einstein diffusion coefficient $D = k_B T / \xi$. In this Thesis we use BD to simulate the trajectories of colloidal systems. In Ref. [3] we perform simulations for a binary mixture of oppositely driven quasi-hard disks and in Ref. [4] we sample the relaxation of patchy colloids adsorbed to a surface with external potential wells.

1.2.2 Monte Carlo simulation

In this Thesis, we study colloidal systems in equilibrium and in non-equilibrium situations. Both Langevin and Brownian dynamics can be applied in both situations. In equilibrium, however, instead of sampling the actual time evolution of the system, it is often more efficient to use stochastic Monte Carlo (MC) methods. The equilibrium average of an observable A in the canonical ensemble, i.e. a system with fixed number of particles N , volume V , and temperature T , is given by [50]

$$\langle A \rangle = \frac{\int d\mathbf{r}^N \exp[-\beta U(\mathbf{r}^N)] A(\mathbf{r}^N)}{\int d\mathbf{r}^N \exp[-\beta U(\mathbf{r}^N)]}. \quad (1.7)$$

Here, the integrals run over all possible positional configurations $\mathbf{r}^N \equiv \{\mathbf{r}_1, \dots, \mathbf{r}_N\}$ of all particles, U denotes the potential energy that depends on the configuration, and $\beta = (k_B T)^{-1}$. In the calculation of the average value $\langle A \rangle$ each state contributes with a weight given by the Boltzmann factor $\exp[-\beta U(\mathbf{r}^N)]$. However, for increasing number of degrees of freedom it generally becomes impossible to consider all configurations of the system. Averages have therefore to be estimated with a finite number of configurations. The idea behind MC methods is to sample states with a probability proportional to their Boltzmann factor and therefore preferably generate states with a high Boltzmann factor and thus high statistical weight in the calculation of averages.

In the standard Metropolis approach, microstates of a canonical system are generated via the following algorithm. First, a random particle i is selected. Then, a new position \mathbf{r}'_i for the particle is proposed by adding a random displacement $\Delta\mathbf{r}$ to its previous position so that $\mathbf{r}'_i = \mathbf{r}_i + \Delta\mathbf{r}$. The new configuration \mathbf{r}'^N with the position \mathbf{r}'_i for the i -th particle is then accepted with probability

$$p_{\text{acc}}^{\text{tr}} = \min(1, \exp[-\beta[U(\mathbf{r}'^N) - U(\mathbf{r}^N)])]. \quad (1.8)$$

If the configuration with the new position \mathbf{r}'_i is not accepted, the old configuration with the position \mathbf{r}_i is restored.

We use MC simulation in the canonical ensemble in Ref. [3] to sample the adiabatic equilibrium reference system of a non-equilibrium steady state of a binary mixture of oppositely driven quasi-hard disks. In Ref. [1] we perform MC simulations for hard systems with arbitrary particle shapes and thus orientational degrees of freedom. To account for the orientational degrees of freedom we also change the particle orientations in each MC step. Additionally, the simulations in this publication are done in the isothermal-isobaric ensemble for which the pressure p is fixed and hence the volume V fluctuates. For these simulations, in addition to the already presented position (and orientation) updates at fixed volume, volume-changing moves are applied. A new volume $V' = V + \Delta V$ is proposed by adding a random volume change ΔV to the current system volume. As part of this, all particle coordinates are scaled by a factor $(V'/V)^{1/d}$, where d is the dimensionality of the system. This leads to an enthalpy change

$$\Delta H = \Delta U + p\Delta V - k_B T N \ln(V'/V), \quad (1.9)$$

where ΔU denotes the change in potential energy. The term $p\Delta V$ accounts for the mechanical work required to expand or compress the system and $-k_B T N \ln(V'/V)$ accounts for the change in the number of possible configurations of the system. The new volume is then accepted with probability

$$p_{\text{acc}}^{\text{V}} = \min(1, \exp[-\beta\Delta H]). \quad (1.10)$$

1.2.3 Smoluchowski equation

Equivalently to the above many-body approaches, in the Fokker-Planck description a colloidal system can be characterized via the many-body probability distribution $\Psi(\mathbf{r}^N, t)$ of finding a system of N particles in a microstate $\mathbf{r}^N \equiv \{\mathbf{r}_1, \dots, \mathbf{r}_N\}$ at time t , where \mathbf{r}_i denotes the position of the i -th particle.

The time evolution of $\Psi(\mathbf{r}^N, t)$ is given by the Smoluchowski equation [51]

$$\frac{\partial \Psi(\mathbf{r}^N, t)}{\partial t} = - \sum_i \nabla_i \cdot \mathbf{v}_i \Psi(\mathbf{r}^N, t), \quad (1.11)$$

with ∇_i indicating the partial derivative with respect to \mathbf{r}_i . The configuration space velocity \mathbf{v}_i is defined by

$$\xi \mathbf{v}_i = -\nabla_i U(\mathbf{r}^N) + \mathbf{f}_{\text{ext}}(\mathbf{r}_i) - k_B T \nabla_i \ln \Psi, \quad (1.12)$$

where U is the interparticle interaction potential, \mathbf{f}_{ext} is the external force field, and the term $-k_B T \nabla_i \ln \Psi$ accounts for diffusion due to the random motion. In the Fokker-Planck description the average of an observable A is built via integration over configuration space

$$\langle A \rangle = \int d\mathbf{r}^N A \Psi(\mathbf{r}^N, t). \quad (1.13)$$

This average is analogous to averaging in the Langevin description over a set of stochastic particle trajectories with different initial conditions and realizations of the random noise in Eq. (1.2).

1.2.4 Density functional and power functional theories

In this section we discuss two theories that describe colloidal systems on the one-body level. This leads to a drastically reduced number of variables that have to be taken into account. Furthermore, the structure in such one-body theories can give insight about the mechanisms behind the captured effects.

Density functional theory

Classical Density Functional Theory (DFT) was formulated in 1979 by Evans [52] based on the electronic Density Functional Theory developed by Hohenberg, Kohn and Sham in 1964 and 1965 [53, 54] and extended to nonzero temperatures by Mermin [55]. DFT is an essential tool for the investigation of the equilibrium properties of inhomogeneous systems. A central object in classical DFT is the equilibrium one-body density distribution

$$\rho_0(\mathbf{r}) = \left\langle \sum_{i=1}^N \delta(\mathbf{r} - \mathbf{r}_i) \right\rangle, \quad (1.14)$$

where δ denotes the Dirac distribution and the average is taken over all microstates according to their equilibrium probability distribution.

Cornerstone of DFT is that for given temperature T , volume V , and chemical potential μ , the grand potential is a functional $\Omega([\rho]; T, V, \mu)$ of the one-body density distribution. This functional satisfies a variational principle that states that the functional is minimal

when the trial density distribution $\rho(\mathbf{r})$ equals the equilibrium density distribution ρ_0 . That is,

$$\left. \frac{\delta\Omega[\rho]}{\delta\rho(\mathbf{r})} \right|_{\rho=\rho_0} = 0 \text{ (min)}. \quad (1.15)$$

Furthermore, the value of the functional evaluated at the equilibrium density profile coincides with the thermodynamic grand potential Ω_0

$$\Omega[\rho_0] = \Omega_0. \quad (1.16)$$

A Legendre transformation yields the intrinsic Helmholtz free energy functional

$$F[\rho] = \Omega[\rho] - \int d\mathbf{r} \rho(\mathbf{r})(V_{\text{ext}}(\mathbf{r}) - \mu), \quad (1.17)$$

where V_{ext} is the external potential. Applying the variational principle, Eq. (1.15), to the free energy gives

$$\left. \frac{\delta F[\rho]}{\delta\rho(\mathbf{r})} \right|_{\rho=\rho_0} = \mu - V_{\text{ext}}(\mathbf{r}). \quad (1.18)$$

The free energy depends only on intrinsic properties of the system, not on the external potential. The free energy can be split into ideal and excess (over ideal) contributions

$$F[\rho] = F_{\text{id}}[\rho] + F_{\text{exc}}[\rho]. \quad (1.19)$$

The ideal part is (exactly) given by

$$F_{\text{id}}[\rho] = k_B T \int d\mathbf{r} \rho(\mathbf{r})(\ln[\lambda^d \rho(\mathbf{r})] - 1), \quad (1.20)$$

with thermal wavelength λ . The excess part depends on the interparticle interactions and it is in general unknown. Only a few exceptions exist where an exact excess functional can be formulated, such as the free energy functional for one-dimensional hard rods developed by Percus [56]. In general, the excess free energy needs to be approximated. Finding good approximations for F_{exc} is the essential point in DFT. A number of common approaches exist, such as the mean-field approximation [57], weighted density approximations [58], and Rosenfeld fundamental measure theories [59–61].

We use DFT in Ref. [3] to calculate the adiabatic potential in the adiabatic reference systems. Furthermore, DFT with Onsager's functional for hard particles is connected to Ref. [1].

Power functional theory

Power Functional Theory (PFT) is an exact generalization of DFT to non-equilibrium situations. PFT is also built around a central functional, which is the unique time-dependent power functional $R_t[\rho, \mathbf{J}]$. The functional depends on two trial fields, the density profile $\rho(\mathbf{r}, t)$ and the current profile $\mathbf{J}(\mathbf{r}, t)$. By construction, at any time t the functional is minimum when evaluated at the actual current profile. That is, it satisfies the variational principle

$$\left. \frac{\delta R_t[\rho, \mathbf{J}]}{\delta\mathbf{J}(\mathbf{r})} \right|_{\rho, \mathbf{J}} = 0 \text{ (min)}, \quad (1.21)$$

where the density $\rho(\mathbf{r}, t)$ as well as the history $\rho(\mathbf{r}, t')$ and $\mathbf{J}(\mathbf{r}, t')$ for times $t' < t$ are fixed and given by the physical time evolution of the system. The functional can be split into three contributions

$$R_t[\rho, \mathbf{J}] = P_t[\rho, \mathbf{J}] + \dot{F}[\rho] - X_t[\rho, \mathbf{J}], \quad (1.22)$$

where $\dot{F}[\rho]$ is the total time derivative of the Helmholtz free energy and describes reversible intrinsic contributions, $X_t[\rho, \mathbf{J}]$ accounts for the external power, and $P_t[\rho, \mathbf{J}]$ accounts for superadiabatic effects such as dissipation and structural forces [62]. Both $\dot{F}[\rho]$ and $P_t[\rho, \mathbf{J}]$ are purely intrinsic functionals, i.e. they do not depend on the external field, and can be split into ideal and excess parts. For $\dot{F}[\rho]$ this splitting follows directly from Eq. (1.19), for $P_t[\rho, \mathbf{J}]$ we have

$$P_t[\rho, \mathbf{J}] = P_{\text{id}}[\rho, \mathbf{J}] + P_{\text{exc}}[\rho, \mathbf{J}]. \quad (1.23)$$

Here, the ideal part represents the free power dissipation of an ideal gas

$$P_{\text{id}}[\rho, \mathbf{J}] = \frac{\xi}{2} \int d\mathbf{r} \frac{\mathbf{J}(\mathbf{r}, t)^2}{\rho(\mathbf{r}, t)}, \quad (1.24)$$

with friction coefficient ξ . The variational principle, Eq. (1.21), yields the time-evolution of the one-body current

$$\frac{\xi \mathbf{J}(\mathbf{r}, t)}{\rho(\mathbf{r}, t)} = -\frac{\delta P_{\text{exc}}[\rho, \mathbf{J}]}{\delta \mathbf{J}(\mathbf{r}, t)} - \nabla \frac{\delta F[\rho]}{\delta \rho(\mathbf{r}, t)} - \nabla V_{\text{ext}}(\mathbf{r}, t) + \mathbf{X}(\mathbf{r}, t), \quad (1.25)$$

where $V_{\text{ext}}(\mathbf{r}, t)$ is a conservative external potential and $\mathbf{X}(\mathbf{r}, t)$ is a non-conservative external force field. Using Eq. (1.25) together with the continuity equation

$$\frac{\partial \rho(\mathbf{r}, t)}{\partial t} = -\nabla \cdot \mathbf{J}(\mathbf{r}, t), \quad (1.26)$$

one obtains the equation of motion for the one-body density $\rho(\mathbf{r}, t)$.

Similar to the excess part of the free energy in DFT, P_{exc} is a complex object that depends on the internal interactions in the system and therefore, analogously to F_{exc} in DFT, needs to be approximated. In Ref. [3] for example we develop an excess functional that describes lane formation in colloidal binary mixtures subject to a gravitational field and is based on the local velocity gradient as introduced in Ref. [63]. Since its original application to Brownian systems, PFT has also been formulated for quantum many-body systems [64] and inertial Newtonian systems [65].

If we neglect the term $\delta P_{\text{exc}}[\rho, \mathbf{J}]/\delta \mathbf{J}(\mathbf{r}, t)$ in Eq. (1.25), we recover the equation of motion of Dynamical Density Functional Theory (DDFT) [52, 66–69]

$$\frac{\xi \mathbf{J}_{\text{DDFT}}(\mathbf{r}, t)}{\rho(\mathbf{r}, t)} = -\nabla \frac{\delta F[\rho]}{\delta \rho(\mathbf{r}, t)} - \nabla V_{\text{ext}}(\mathbf{r}, t) + \mathbf{X}(\mathbf{r}, t), \quad (1.27)$$

where $\mathbf{J}_{\text{DDFT}}(\mathbf{r}, t)$ is the one-body current of DDFT. Neglecting $\delta P_{\text{exc}}[\rho, \mathbf{J}]/\delta \mathbf{J}(\mathbf{r}, t)$, i.e. the superadiabatic contributions to the power functional, is therefore equivalent to the so-called adiabatic approximation taken in DDFT. This approximation can also be understood on the level of internal forces as follows.

The one-body current $\mathbf{J}(\mathbf{r}, t)$ is generated by the total force field $\mathbf{f}(\mathbf{r}, t)$ via

$$\mathbf{J}(\mathbf{r}, t) = \xi^{-1} \rho(\mathbf{r}, t) \mathbf{f}(\mathbf{r}, t). \quad (1.28)$$

The total force field can be split into three contributions

$$\mathbf{f}(\mathbf{r}, t) = \mathbf{f}_{\text{int}}(\mathbf{r}, t) + \mathbf{f}_{\text{ext}}(\mathbf{r}, t) - k_B T \nabla \ln \rho(\mathbf{r}, t), \quad (1.29)$$

namely the internal force field $\mathbf{f}_{\text{int}}(\mathbf{r}, t)$ due to interactions between the (colloidal) particles, the external force field $\mathbf{f}_{\text{ext}}(\mathbf{r}, t)$, and the stochastic force field, which is captured in the diffusive term $-k_B T \nabla \ln \rho(\mathbf{r}, t)$.

The internal force field can be split into adiabatic and superadiabatic part

$$\mathbf{f}_{\text{int}}(\mathbf{r}, t) = \mathbf{f}_{\text{ad}}(\mathbf{r}, t) + \mathbf{f}_{\text{sup}}(\mathbf{r}, t). \quad (1.30)$$

Here, the adiabatic part is the internal force field in a reference equilibrium system (the adiabatic system) with the same one-body density as the non-equilibrium system. The remaining superadiabatic part can be identified with the previously discussed functional derivative

$$\mathbf{f}_{\text{sup}}(\mathbf{r}, t) = -\frac{\delta P_{\text{exc}}[\rho, \mathbf{J}]}{\delta \mathbf{J}(\mathbf{r}, t)}. \quad (1.31)$$

Via the adiabatic construction, developed in Ref. [70], it is possible to obtain the adiabatic and superadiabatic forces of a non-equilibrium system separately in simulations. In the adiabatic construction, the adiabatic reference system is explicitly sampled, e.g. with Monte Carlo methods. The adiabatic reference system is an equilibrium system subject to an adiabatic potential V_{ad} . The adiabatic potential is constructed in such a way that the adiabatic system has the same one-body density as the non-equilibrium system. The force balance in the adiabatic system is hence given by

$$\mathbf{f}_{\text{ad}}(\mathbf{r}) - \nabla V_{\text{ad}}(\mathbf{r}) - k_B T \nabla \ln \rho(\mathbf{r}) = 0, \quad (1.32)$$

where ∇ indicates the derivative with respect to the position \mathbf{r} . In Ref. [3] we extend the adiabatic construction to binary mixtures and explicitly sample adiabatic and superadiabatic forces in a binary mixture exhibiting non-equilibrium colloidal laning. As a result, we demonstrate that lane formation is a superadiabatic effect by identifying a superadiabatic force that counteracts the entropic mixing of the two species and hence leads to the formation of lanes. In addition, we introduce the novel and general concept of splitting the one-body force field in mixtures into a species-dependent and a species-independent part. We show that for lane formation this approach is very useful as only the species-dependent part, which affects concentrations, is relevant, whereas the species-independent part only affects the total density and does not contribute to the demixing into lanes.

1.2.5 Sedimentation-diffusion-equilibrium of binary colloidal mixtures

In Ref. [2] we extend the theory of sedimentation paths to finite sample heights and show that the sample height is a vital parameter in sedimentation experiments. Here, we show the basic concepts of the underlying theory of sedimentation paths for infinite samples [41, 42].

For a binary colloidal mixture subject to gravity, one can define height- and species-dependent local chemical potentials

$$\psi_i(z) = \mu_i^b - m_i g z, \quad i = 1, 2, \quad (1.33)$$

where μ_i^b is the bulk chemical potential of species i in absence of gravity, m_i is the buoyant mass of this species, g is the acceleration due to gravity, and z denotes the vertical coordinate in the system. Eliminating gz from the above equations yields

$$\psi_2(\psi_1) = a + s\psi_1, \quad (1.34)$$

with constants $a = \mu_2^b - s\mu_1^b$ and $s = m_2/m_1$. Eq. (1.34) describes a straight line in the $\psi_1 - \psi_2$ plane of local chemical potentials, the so called sedimentation path.

If all correlation lengths in the system are small compared to the gravitational lengths $\xi_i = \frac{k_B T}{m_i g}$, one can apply a local density approximation (LDA) [71]. Then, one can assume that the state of the system at height z is the same as the equilibrium state of a bulk system with chemical potentials μ_i , that is

$$\mu_i = \psi_i(z), \quad i = 1, 2. \quad (1.35)$$

In the limit of samples with very large (infinite) height, a sedimentation path is fully defined by its slope s , intercept a , and direction (given by the sign of the buoyant masses). The stacking sequence observed in a sample follows directly from its sedimentation path, since each time the sedimentation path crosses a boundary between two phases in the phase diagram, such as e.g. a binodal line, an interface appears in the vessel.

Fig. 1.6 shows a typical bulk phase diagram with characteristic sedimentation paths (a) and the resulting stacking diagram (b) in the $s - a$ plane. In this plane, each point corresponds to one sedimentation path in the plane of chemical potentials. The boundaries in the stacking diagram are defined by the fact that at these points an infinitesimal change in s and/or a of the sedimentation path qualitatively changes the stacking sequence.

There are three different types of boundaries in the stacking diagram. First, there are sedimentation binodals which are formed by the set of all sedimentation paths that are tangent to the binodal. Second, there are terminal lines for which the corresponding sedimentation paths cross an end point of the binodal, such as e.g. a critical point. And third, there are asymptotic terminal lines for which the corresponding sedimentation paths are parallel to the asymptotic behaviour of the binodal.

Fig. 1.6 shows how even a very simple bulk phase diagram already leads to a complex stacking diagram with several stacking sequences. In Ref. [2] we extend this theory to the experimentally relevant case of samples with finite height and analyze the stacking diagrams of mixtures of patchy colloids. For samples with finite height sedimentation paths are no longer infinite lines, but line segments. This qualitative distinction entails new types of boundaries in the stacking diagram, which we discuss in detail in the publication. We demonstrate that the sample height is an important parameter, as it changes the length of the sedimentation paths. As a consequence, there can for example be stacking sequences that only appear for certain sample heights when all other parameters like relative concentrations are fixed.

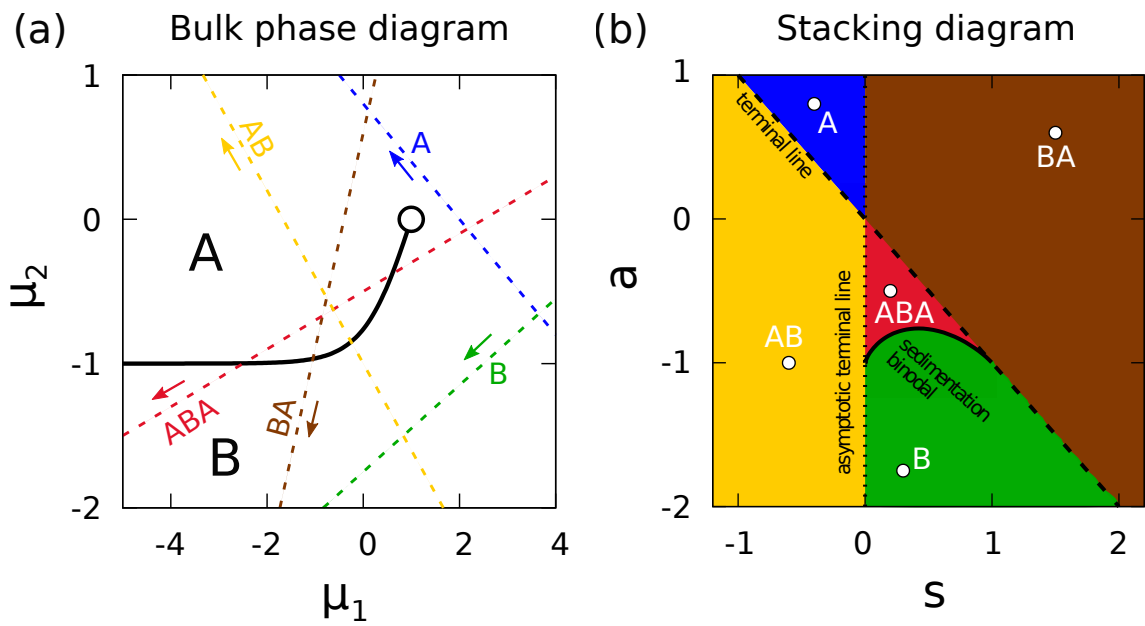


Figure 1.6: (a) Bulk phase diagram in the plane of chemical potentials of a model binary mixture. A binodal (solid black line) that ends at a critical point (circle) separates two phases A and B, as indicated by black letters. For each possible stacking sequence one selected sedimentation path is represented in the bulk phase diagram (dashed lines). The arrows of the paths indicate the direction from the bottom to the top of the sample. The colored letters indicate the stacking sequence corresponding to each sedimentation path. (b) Stacking diagram in the s - a plane for $m_1 > 0$ corresponding to the bulk phase diagram in (a). The circles indicate the position of the sedimentation paths highlighted in panel (a). Three different types of boundaries separate the regions of different stacking sequences, as indicated.

1.2.6 Wertheim theory and percolation

Wertheim's association theory [72] was originally intended to describe molecular fluids, but it has become an essential tool for the theoretical description of patchy colloids. In this section we introduce the basic concepts and results of this theory. In Ref. [2] we use this approach, which is also presented in e.g. Refs. [73,74], to calculate the phase diagram of binary mixtures of patchy colloids and subsequently obtain the stacking diagrams for these systems. Therefore, in the following we also discuss a binary mixture of patchy colloids.

Wertheim's first order perturbation theory describes a system of patchy colloids as a reference system, containing the repulsive forces of the cores, which is perturbed by the attractive bonds. The reference system is typically modeled via the hard sphere fluid, the properties of which are well known. In its basic form, Wertheim's theory is based on three assumptions: (i) there are no closed loops of bonds, (ii) one bond involves only two patches of two different particles, and (iii) the patches are randomly distributed over the surface of the particle core.

In Wertheim's theory the Helmholtz free energy F is expressed as the sum of the free energy of the unperturbed reference system (hard sphere fluid in our case) and the contribution due to the bonds

$$F/N = f_{\text{HS}} + f_b, \quad (1.36)$$

where $N = N_1 + N_2$ is the total number of particles of both species, f_{HS} is the free energy per particle of the reference hard sphere fluid, and f_b is the free energy per particle due to bonding. The free energy of the reference hard sphere fluid can be split into ideal and excess parts $f_{\text{HS}} = f_{\text{id}} + f_{\text{ex}}$, where the ideal part for a binary mixture is given exactly by

$$\beta f_{\text{id}} = \ln \eta - 1 + \sum_{i=1,2} x^{(i)} \ln \left(x^{(i)} \lambda_i^d \right). \quad (1.37)$$

Here, $x^{(i)} = N_i/N$ is the molar fraction of species $i = \{1, 2\}$, $\eta = \eta_1 + \eta_2$ is the total packing fraction, and λ_i is the thermal wavelength of the i -th species. For a fluid the excess part is well described with the quasi-exact Carnahan-Starling equation of state [75,76]

$$\beta f_{\text{ex}} = \frac{4\eta - 3\eta^2}{(1 - \eta)^2}, \quad (1.38)$$

where we have used that both species have the same diameter. With the above assumptions, the bonding free energy per particle is given by

$$\beta f_b = \sum_{i=1,2} x^{(i)} \left[\sum_{\alpha \in \Gamma(i)} \left(\ln X_{\alpha}^{(i)} - \frac{X_{\alpha}^{(i)}}{2} \right) + \frac{f^{(i)}}{2} \right], \quad (1.39)$$

where $X_{\alpha}^{(i)}$ is the probability that a patch of type α on species i is not bonded, $\Gamma(i)$ is the set of patches on a particle of species i , and $f^{(i)}$ is the total number of patches of a particle of species i , also known as functionality. The probabilities $\{X_{\alpha}^{(i)}\}$ are calculated via laws of mass action

$$X_{\alpha}^{(i)} = \left[1 + \eta \sum_{j=1,2} x^{(j)} \sum_{\gamma \in \Gamma(i)} X_{\gamma}^{(j)} \Delta_{\alpha\gamma}^{(ij)} \right]^{-1}. \quad (1.40)$$

Here, the constants $\Delta_{\alpha\gamma}^{(ij)}$ characterize a bond between a site α on a particle of species i and a site γ on a particle of species j . Their values depend on how one models the patches. For spherical patches interacting via square well potentials they are given by

$$\Delta_{\alpha\gamma}^{(ij)} = \Delta_{\alpha\gamma} = \frac{1}{v_s} \int_{v_{\alpha\gamma}} g_{\text{HS}}(\mathbf{r}) [\exp(\beta\epsilon_{\alpha\gamma}) - 1] d\mathbf{r}, \quad (1.41)$$

where v_s denotes the volume of a single particle, and $g_{\text{HS}}(\mathbf{r})$ is the radial distribution function of the reference hard sphere fluid. The integral is calculated over the bonding volume $v_{\alpha\gamma}$, and it is assumed that the depth of the square wells $\epsilon_{\alpha\gamma}$ only depends on the types of bonding sites (α and γ), but not on the particle species.

The formation of bonds in patchy colloidal systems can lead to percolation, also known as gelation. A system of patchy colloids is percolated if via bonding it forms a cluster that spans the whole system. When a system begins to percolate, it transforms from a viscous liquid into an elastic disordered solid [77], which in addition to the direct change of the viscoelastic properties can lead to drastic changes in e.g. the electric conductivity. A generalized Flory-Stockmayer theory of percolation [78–80] allows the calculation of the threshold at which a system of patchy colloids with an arbitrary number of distinct bonding sites percolates. Consistent with the assumptions made in Wertheim’s theory, this theory neglects closed loops and therefore assumes a tree-like bonding structure of the cluster as shown in Fig. 1.7. In this structure the patchy colloids can be organized in levels. A system is percolated if the number of bonds is constant or increases with increasing level. This can be expressed with a transition matrix containing the probabilities of forming a bond between distinct patches. The system is percolated if the highest eigenvalue of this matrix is higher or equal than one. For a detailed derivation see for example Ref. [74].

For binary mixtures each species can be individually percolated if one counts only those bonds between particles of this species. Consequently, there are four different percolated states. If the mixture is percolated when all bonds are considered but the individual species are not percolated, the system forms a mixed gel. In a bicontinuous gel the mixture and also both species individually are percolated. Finally, a standard gel 1 (2) is present if the mixture as well as only species 1 (2) are percolated.

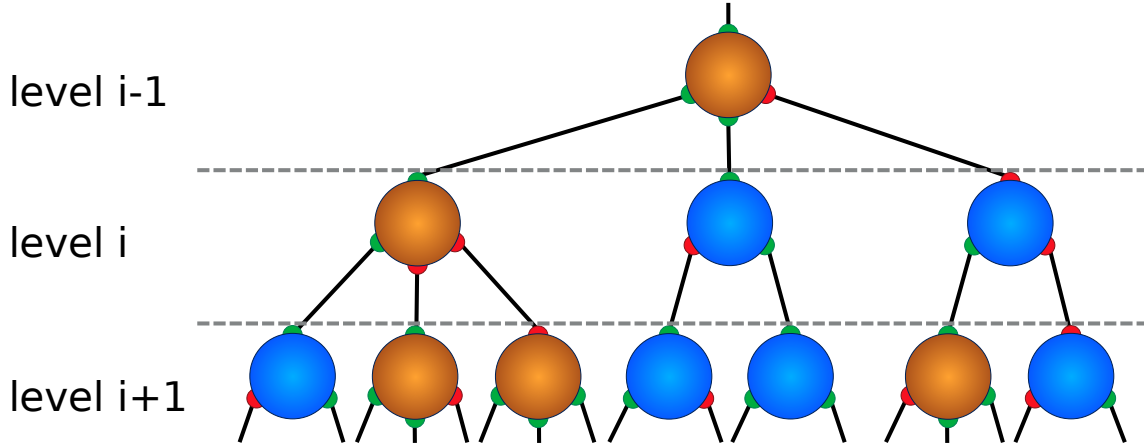


Figure 1.7: Schematic of the tree-like bonding structure assumed in Flory-Stockmayer theory. A binary mixture of patchy colloids is percolated if for increasing level the number of bonds (black lines) is constant or increases. In this figure all patches are bonded and the system is percolated. Color indicates species (blue and orange) as well as different types of patches (red and green).

1.2.7 Excluded volume and Onsager theory

Hard body models play a vital role in the theoretical description of colloids. Hard models assume that the interaction energy U for a pair of particles has the form

$$U = \begin{cases} \infty, & \text{if particles overlap,} \\ 0, & \text{otherwise.} \end{cases} \quad (1.42)$$

As a consequence, only configurations in which the particles do not overlap are possible. When considering two particles where the position of one of them is fixed, the potential gives rise to a volume inaccessible to the other particle. This volume is called excluded volume (excluded area for a two-dimensional system). The excluded area between two hard rectangles is shown in panels (a) and (b) of Fig 1.8 for two different particle orientations.

The magnitude of the excluded volume is a function of the orientation of both particles. In two dimensions this reduces to the magnitude of the excluded area $A_{\text{exc}}(\Phi)$ that only depends on the relative angle Φ between the particles. As an example, for two rectangles a plot is presented in panel (c) of Fig. 1.8. For rectangles, $A_{\text{exc}}(\Phi)$ is minimal if $\Phi = \{0, \pi\}$, which corresponds to the particles being parallel or antiparallel.

Onsager's theory for anisotropic particles [81] uses the concept of excluded volume to describe the isotropic-nematic phase transition introduced in Sec. 1.1.1. Applying the modern framework of DFT, we briefly introduce the basic concept here.

The ideal part of the free energy of a system of anisotropic particles can be written as

$$F_{\text{id}}[\rho] = k_B T \int d\mathbf{r} \int d\mathbf{\Omega} \rho(\mathbf{r}, \mathbf{\Omega}) (\ln[\lambda^d \rho(\mathbf{r}, \mathbf{\Omega})] - 1), \quad (1.43)$$

which is a direct generalization of Eq. (1.20) to a density distribution $\rho(\mathbf{r}, \mathbf{\Omega})$ that in addition to the position \mathbf{r} also depends on the orientation $\mathbf{\Omega}$.

For uniform phases, i.e. $\rho(\mathbf{r}, \mathbf{\Omega}) = \rho f(\mathbf{\Omega})$ with orientational distribution function $f(\mathbf{\Omega})$, the excess part of the free energy can be approximated via the virial expansion truncated to second order, which provides a very good description at sufficiently low densities. Hence,

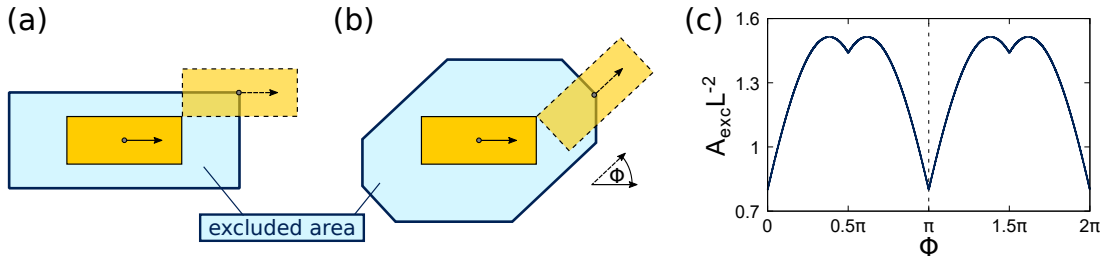


Figure 1.8: (a) Schematic of the excluded area between two hard rectangles. One rectangle (orange with solid frame) is fixed at the origin. The other rectangle (orange with dashed frame) is located at the border of the excluded area (blue). The arrows indicate the orientation of the two rectangles, which are parallel. (b) Analogous schematic for two rectangles with a relative orientation Φ . (c) Plot of the magnitude of the excluded area A_{exc} as a function of the relative orientation for two identical rectangles with aspect ratio $L/D = 5$, with L and D the length and the width of the rectangles, respectively.

for hard systems

$$\beta \frac{F_{\text{exc}}[f]}{N} = \frac{\rho}{2} \int d\Omega \int d\Omega' f(\Omega) f(\Omega') V_{\text{exc}}(\Omega, \Omega'), \quad (1.44)$$

where $V_{\text{exc}}(\Omega, \Omega')$ denotes the excluded volume between two particles with orientations Ω and Ω' . At low densities, the total free energy is dominated by the ideal term, which for a fixed bulk density ρ is minimal if $f(\Omega)$ is constant (isotropic phase). Therefore, the isotropic phase in which particles are randomly oriented is stable. At high densities, however, the excess part is the dominant term. The excess free energy is minimal if particles preferably occupy orientations for which V_{exc} is minimal. For two-dimensional rectangles, A_{exc} is minimal if the particles are parallel or antiparallel, as shown in Fig. 1.8c, which stabilizes the nematic phase. In other words, in the isotropic phase the orientational entropy is maximized and in the nematic phase the positional entropy is maximized since minimum excluded volume means the volume accessible to each particle is maximized.

The example of the isotropic-nematic transition demonstrates that minima of A_{exc} can promote orientational order. In Ref. [1] we systematically study the connection between the particle shape, the microscopic excluded area, and the macroscopic bulk behaviour. We numerically calculate A_{exc} for a large set of two-dimensional hard particles with randomly created particle shapes. Via Principal Component Analysis (see next section) we identify - despite the vast diversity of particle shapes - only a few qualitative types of A_{exc} for which the formation of states with different orientational order is expected according to two-body approaches like Onsager theory.

1.2.8 Principal component analysis

Principal component analysis (PCA) is a procedure that represents a given dataset in a new orthonormal basis. There, the basis vectors are chosen in a way that the variance of the data projected onto them is maximized. With PCA it can be possible to identify directions that have physical meaning and also to perform a dimension reduction of the data while keeping as much information as possible [82, 83].

For PCA the dataset is organized in an $n \times p$ matrix $\hat{\mathbf{X}}$. Each column of this matrix contains n realizations of one specific variable and each row contains one sample of the data, e.g. a measurement of all p relevant variables at a given time t . As a first step, the columnwise mean \mathbf{m} is subtracted from $\hat{\mathbf{X}}$

$$\mathbf{X} = \hat{\mathbf{X}} - \mathbf{h}\mathbf{m}^T, \quad (1.45)$$

where \mathbf{h} is an $n \times 1$ column vector with components $h_j = 1$ and \mathbf{m} a $p \times 1$ column vector with components

$$m_j = \frac{1}{n} \sum_{i=1}^n \hat{X}_{ij}. \quad (1.46)$$

This procedure, called centering, simplifies the following calculations and can be reversed after the transformation with PCA by adding back the transformed mean.

The centered data matrix \mathbf{X} is then expressed in a new basis. In this basis the first basis vector \mathbf{w}_1 is chosen so that the variance of the projection of the data onto this vector is as large as possible

$$\mathbf{w}_1 = \arg \max_{\|\mathbf{w}_1\|=1} \{\|\mathbf{X}\mathbf{w}_1\|^2\} := \arg \max_{\|\mathbf{c}_1\|=1} \{\|\mathbf{c}_1\|^2\}. \quad (1.47)$$

Along all following basis vectors the variance of the data is also maximized, but under the constraint that the vectors are orthogonal to all preceding ones. The new basis vectors \mathbf{w}_i are called principal axes and the components of a vector expressed in this basis are the principal components. The vector \mathbf{c}_1 defined in Eq. (1.47) contains the first principal component of each sample.

As a toy example for the illustration of the method, consider a two-dimensional experiment in which the position $(\hat{x}_{m_0}, \hat{y}_{m_0})$ of a point mass m_0 attached to an ideal spring is measured. The spring is oriented along a random direction, the measurement is subject to experimental error, and the position of m_0 is measured at several random points in time. This experimental setup is schematically presented in Fig. 1.9a. The resulting dataset is shown in panel (b) of Fig. 1.9 and can be represented with an $n \times 2$ matrix.

After centering, the data are expressed via the mean-free variables (x_{m_0}, y_{m_0}) , shown in panel (c). Panel (d) shows the dataset in the new basis of the principal axes.

In this toy example it is clear that the direction of the first principal axis is along the orientation of the spring, while in the direction of the second principal axis there is only noise due to the experimental errors. Therefore, PCA has revealed that there is an underlying physical structure to the data. This allows us to neglect the second principal component without losing any relevant information and therefore reduce the dimensionality of the data to its single physical dimension.

Mathematically, PCA is an eigenvalue problem. The principal axes \mathbf{w}_i are the normalized eigenvectors of the covariance matrix \mathbf{C} of \mathbf{X} , which is defined as

$$\mathbf{C} = \frac{1}{n-1} \mathbf{X}^T \mathbf{X}. \quad (1.48)$$

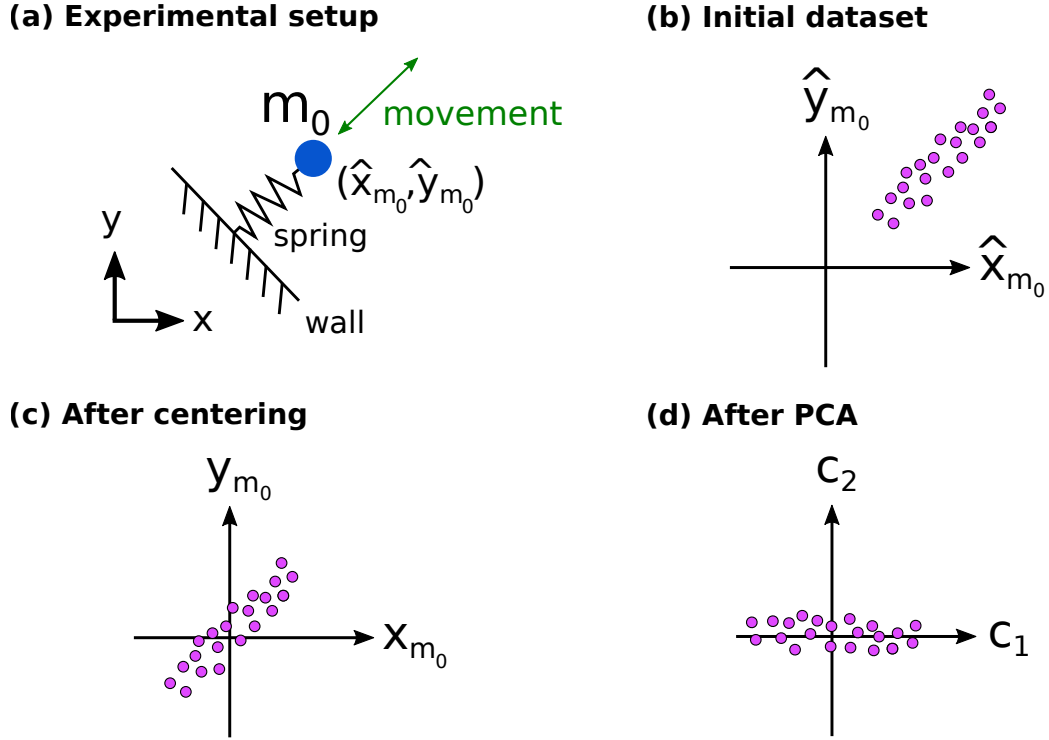


Figure 1.9: (a) Experimental setup where the position $(\hat{x}_{m_0}, \hat{y}_{m_0})$ of a point mass m_0 attached to an ideal spring is measured with a small experimental error. (b) The resulting dataset before PCA, (c) after centering, (d) represented with principal components in the new basis.

The projection of \mathbf{X} onto a vector \mathbf{v} is given by $\mathbf{X}\mathbf{v}$. The variance of such a projection is

$$\text{var}\{\mathbf{X}\mathbf{v}\} = \frac{1}{n-1}(\mathbf{X}\mathbf{v})^T \mathbf{X}\mathbf{v} = \mathbf{v}^T \frac{1}{n-1} \mathbf{X}^T \mathbf{X} \mathbf{v} = \mathbf{v}^T \mathbf{C} \mathbf{v}. \quad (1.49)$$

By construction \mathbf{C} is real and symmetric and hence, according to the spectral theorem, there exists an orthonormal basis of eigenvectors of \mathbf{C} in which \mathbf{C} has the form of a diagonal matrix with positive eigenvalues λ_i as entries on the diagonal [84]. PCA labels the eigenvalues λ_i such that their magnitude increases with the label i . In this basis, Eq. (1.49) simplifies to

$$\text{var}\{\mathbf{X}\mathbf{v}\} = \mathbf{v}^T \mathbf{C} \mathbf{v} = \sum_i \lambda_i v_i^2. \quad (1.50)$$

At this point it is clear that for a unit vector \mathbf{v} this variance is maximized if \mathbf{v} expressed in the eigenbasis has the form $\mathbf{v} = (1, 0, 0, \dots)$, which is precisely the normalized eigenvector \mathbf{w}_1 belonging to the largest eigenvalue λ_1 . Sequentially, all other eigenvectors are the vectors which maximize the variance under the constraint that they are orthogonal to all preceding vectors, i.e. the second principal axis is given by $\mathbf{w}_2 = (0, 1, 0, \dots)$ and so on. In Eq. (1.50) one can also see that the variance is directly given by the eigenvalue λ_i provided that \mathbf{v} is the principal axis \mathbf{w}_i .

A measure that is often used when doing a dimension reduction via PCA is how much variance is kept when the data are expressed with only the first k principal components.

The so called explained variance σ_k is defined as [85]

$$\sigma_k = \frac{\sum_{i=1}^k \lambda_i}{\sum_{i=1}^p \lambda_i}, \quad (1.51)$$

and it has per definition values between 0 (no variance explained) and 1 (all variance explained). The value of σ_k increases monotonically with k .

In Ref. [1] we use PCA to analyze the excluded area of randomly generated hard particles. We apply PCA to a data matrix for which each row contains for one randomly generated particle shape the magnitude of the excluded area $A_{\text{exc}}(\phi)$ for p relative orientations (e.g. what is plotted in Fig. 1.8c for the example of a rectangle could be one row), while in each column the relative orientation is fixed, but different particle shapes are considered. Our analysis reveals that with only three principal components one can surprisingly well approximate the data ($\sigma_3 \approx 0.98$). We show that this result is caused by the fact that global features of the particle shape like the elongation of the particle dominate the shape of $A_{\text{exc}}(\phi)$ rather than local features like small bumps and dents. As a consequence, we identify a number of relevant limiting cases for the possible shapes of $A_{\text{exc}}(\phi)$.

2 Overview of the publications

This section gives an overview of the publications contributing to this cumulative Thesis. The order in which the publications are presented is chronological according to the time when we started working on them, which also gives a coherent sequence. Nevertheless, all publications are self-contained projects and can therefore be read in any order.

The four publications are closely intertwined, as schematically presented in Fig. 2.1. In all cases anisotropy plays a major role and leads to the formation of complex and interesting structures. Our research helps understanding how and why those structures are formed.

The first publication [1] discusses the effect of anisotropic particle shapes on the bulk phase behaviour of two-dimensional hard models. Using PCA we investigate different types of excluded volume interactions in such systems.

The second publication [2] deals with sedimentation, a process that is inherently anisotropic due to the external gravitational field. We develop a theory for sedimentation in finite vessels in order to predict the sedimentation-diffusion-equilibrium stacking sequences of colloidal mixtures. We investigate characteristic mixtures of patchy colloids with directional anisotropic interactions under the influence of gravity, which induces a very rich phenomenology.

Gravity has a strong effect on colloidal systems in both equilibrium and out-of-equilibrium situations. In the third publication [3] we study a non-equilibrium system in which a binary colloidal mixture of hard particles oppositely driven by gravity separates into macroscopic lanes. Although in this work we only consider a model with isotropic interparticle interactions, the directional external driving induces anisotropy in the system.

Another non-equilibrium system is investigated in the last publication [4]. Here, we again study the behaviour of patchy colloids. In particular, the relaxation of patchy colloids on a surface patterned with potential wells is examined. Hence, anisotropy is present here in both the internal particle interactions and the external field.

In this Thesis we also develop new methods for the theoretical study and computer simulation of colloidal systems. This includes a novel way of applying PCA to soft matter systems, a theory of sedimentation in finite samples, a power functional for binary mixtures, and the construction of the adiabatic system in mixtures.

2.1 Principal Component Analysis of the excluded area of two-dimensional hard particles

In this publication [1] we study the possible types of interactions in two-dimensional hard systems via the excluded area between two particles in order to make predictions about the structures that might appear in bulk. Such theoretical understanding is motivated by recent experimental advances like those presented in Sec. 1.1.1, which allow the synthesis of colloidal particles with arbitrary shape and thus complex steric interactions. The aim of

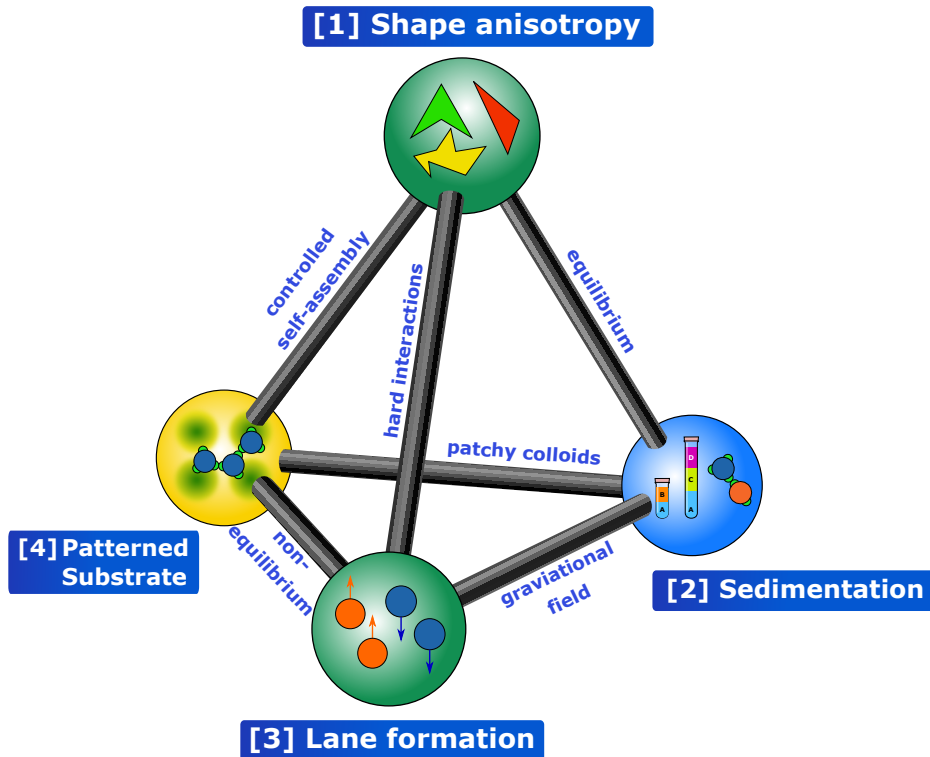


Figure 2.1: Schematic overview of the four topics addressed in the Thesis: [1] shape anisotropy, [2] sedimentation, [3] lane formation, and [4] patterned substrate. The links between the topics are also presented. The color of the spheres indicates our approach to each topic: theory (light blue), simulation (yellow), or both (green).

this work is to systematically understand the interplay between the particle shape, the excluded area, and the macroscopic bulk behaviour, as well as to identify the particle shapes that lead to interesting self-assembly scenarios. To this end, we study two-dimensional hard systems in which the particles are modelled via randomly generated polygons or star lines, which are line segments radiating from a common origin. Based on edge intersection, we develop a general method for the numerical calculation of the excluded area between two particles of arbitrary shape at a given relative orientation. We show that for regular polygons the variance of the magnitude of the excluded area as a function of the relative orientation (in the following for simplicity referred to as just "excluded area") decreases rapidly when the number of vertices is increased. This finding indicates that weaker orientational ordering is expected by increasing the number of vertices, and it is in line with the finding that e.g. melting properties of hard models of regular polygons quickly converge to that of hard disks when the number of vertices is increased [86].

Subsequently, we perform a statistical analysis of a large set of excluded areas (and therefore particle shapes) via Principal Component Analysis. This analysis reveals that the excluded area can be described very well with only three principal components. In the subspace of the first three principal components all excluded areas are contained in a structure that is limited by a hierarchy of excluded areas that are characterized by an increasing number of global minima that appear at regular relative orientations. We find that the general elongation of a particle, which for example can drive an isotropic-

nematic transition, has the by far highest influence for determining the excluded area. Furthermore, we show that the global minimum of the value of the excluded area appears for all shapes in our set when the two particles are antiparallel. As a result of our statistical analysis, we identify several particle shapes with excluded areas that might self-assemble into interesting structures. An example is a class of particles that can continuously be deformed in a way that a transition from a triatic to an uniaxial structure might occur. With NpT Monte Carlo simulations we show examples of the validity and of the limitations of theoretical approaches that incorporate only two-body interactions to investigate hard systems.

2.2 The role of sample height in the stacking diagram of colloidal mixtures under gravity

Any experiment performed on the Earth is subject to gravity. In colloidal systems, due to the comparability of thermal and gravitational energies, gravity leads to sedimentation effects on lengthscales that are typically around the order of millimeters to centimeters. Common situations in which such effects manifest are the undesired phase separation in food products such as milk drinks, and also medical tests, particularly those in which blood sedimentation is involved.

This manuscript [2] is based on a recently proposed theory [41, 42] linking the bulk phase behaviour to the sedimentation-diffusion-equilibrium in colloidal mixtures. The theory predicts the stacking diagram, i.e. the set of all possible sequences of different layers in colloidal mixtures due to sedimentation, from the bulk phase diagram of the mixture. The original theory was formulated with the assumption of very large (infinite) samples and is introduced in Sec. 1.2.5. Here, we extend the theory to systems with finite sample heights. Using a local density approximation (LDA) [71] for each species one can define a height-dependent local chemical potential. This defines a so called sedimentation path which can be represented with a line in the plane of chemical potentials $\mu_1 - \mu_2$ for infinite vessels and a line segment for samples with finite height. An interface appears in the vessel each time the respective sedimentation path crosses a boundary in the phase diagram, e.g. a binodal. For fixed vessel height and buoyant masses of both species, the length as well as the slope and direction of the sedimentation path are determined. The sedimentation path then only depends on the bulk chemical potentials. Consequently, one can represent the stacking diagram in the plane of average chemical potentials, where the average is taken over the whole sample. Alternatively, one can transform the stacking diagram to the plane of average packing fractions of both species for better comparison with experiments. In the stacking diagram areas with the same stacking sequence are separated by boundaries that correspond to limiting cases for the sedimentation paths which are discussed in detail in the manuscript.

We apply the theory first to a model system and then to mixtures of patchy colloids that either differ in the number or the types of patches. We obtain the bulk phase diagrams of the mixtures using Wertheim's theory and Flory-Stockmayer theory of polymerization. The resulting stacking diagrams show an abundance of different stacking sequences. A comparison between the stacking diagrams of two systems that differ only in their sample heights reveals that there can be qualitative differences between them, e.g. stacking sequences that only appear for certain sample heights. We therefore conclude that the sample height, which has received very little attention in experimental work, is an important parameter in sedimentation experiments that should at least be always specified.

2.3 Superadiabatic demixing in nonequilibrium colloids

In this publication [3] we use computer simulation and Power Functional Theory to provide deep theoretical insight into the microscopic mechanism behind non-equilibrium lane formation and jamming in binary mixtures of oppositely driven colloids.

With BD simulations we investigate a model of monodisperse quasi-hard disks subject to an external driving in opposite directions, originated by a gravitational field acting on two particle species with opposite buoyant masses. The one-body force field $\mathbf{f}^\alpha(\mathbf{r}, t)$ acting on particles of species α at location \mathbf{r} and time t is measured. The total force field is split into three contributions

$$\mathbf{f}^\alpha(\mathbf{r}, t) = \mathbf{f}_{\text{int}}^\alpha(\mathbf{r}, t) + \mathbf{f}_{\text{ext}}^\alpha(\mathbf{r}, t) - k_B T \ln \rho_\alpha(\mathbf{r}, t). \quad (2.1)$$

Here, $\mathbf{f}_{\text{int}}^\alpha$ arises from the internal interactions, $\mathbf{f}_{\text{ext}}^\alpha$ from the external driving, and the term $-k_B T \ln \rho_\alpha(\mathbf{r}, t)$ from ideal diffusion with ρ_α being the density of species α . The internal interactions are further split into adiabatic and superadiabatic parts

$$\mathbf{f}_{\text{int}}^\alpha(\mathbf{r}, t) = \mathbf{f}_{\text{ad}}^\alpha(\mathbf{r}, t) + \mathbf{f}_{\text{sup}}^\alpha(\mathbf{r}, t). \quad (2.2)$$

The adiabatic force field is obtained in Monte Carlo simulations by explicitly sampling the equilibrium adiabatic system which has the same one-body densities as the actual driven non-equilibrium system. In the equilibrium system, the external forces are generated by adiabatic potentials which we estimate with a simple Density Functional Theory.

At fixed high density, depending on the driving strength, the system is in one of three states. At low drivings the two species diffuse homogenously through each other. At high driving strength lane formation appears. In this state the internal force field is highly non-trivial and has several species-dependent and species-independent contributions. A species-dependent structural force counteracts the entropic tendency of the mixture to mix. This superadiabatic force is responsible for the lane formation. We also identify a species-independent superadiabatic force that acts on the total density and opposes the adiabatic excess force, and superadiabatic viscous and drag forces that act in the direction of the external driving.

At intermediate driving strengths the system forms a jammed state where the two species block each other. By using the same approach as for the laned state we show the general applicability of our concepts. We demonstrate that the phenomenologically important adiabatic contribution for the jammed state is the adiabatic excess force related to the total density, which is in contrast to the ideal demixing vital to the lane formation.

For the laned state we develop a Power Functional theory that is able to reproduce all listed force contributions. It is based on the velocity gradient approximation presented in Ref. [63].

2.4 Crossover from three- to six-fold symmetry of colloidal aggregates in circular traps

In this publication we study the dynamics of patchy colloidal particles decorated with three patches. The particles are adsorbed to a surface which is covered with a square pattern of attractive potential wells. The wells have a circular Gaussian profile. Similar setups can experimentally be realized using e.g. an array of optical tweezers.

The system is in the overdamped regime. The interparticle potential consists of a spherical repulsive interaction between the particle cores as well as an attractive patch

interaction, where the patches have Gaussian form and do not interact with the cores. In addition to the internal interactions, there are external forces generated by the Gaussian potential wells that only act on the cores.

We study the relaxation of the patchy colloidal particles after a homogenous initialization as a function of the width of the potential wells. The behaviour of the particles is characterized by a competition between the potential energy of the cores, which is minimized if the particles aggregate in close packing near the centers of the potential wells, and the bonding energy of the patches, which is minimized if open networks with low packing fraction are formed.

For wider traps, which lead to weak confinement forces, the particles form networks with the three-fold symmetry of the patches. For very narrow traps a close packing around the trap centers with six-fold symmetry arises. At intermediate trap widths a core-shell structure with six-fold symmetric packing near the core surrounded by a three-fold network forms. We furthermore investigate the time-scales of the relaxation process and show that the outer network dynamics is slower than that of the close-packed core.

In order to test the dynamical properties of the system, we study its response to dynamically oscillating widths of the potential wells. The behaviour strongly depends on the oscillation frequency and the temperature. The latter influences the intrinsic timescales of diffusion and bonding. At high temperatures and low oscillation frequencies the intrinsic timescales are short enough such that the system can adapt instantaneously to the changes in trap width. In contrast, at low temperatures and high oscillating frequencies, the system remains almost unchanged in its initial state. At intermediate parameters the system responds to changes of the potential width with some delay.

In summary, our simulations provide insight on how to dynamically control the self-assembly of the system into different structures.

2.5 Author contributions

In all four publications contained in this Thesis I am the first author, responsible for the generation and interpretation of the data in close collaboration with the involved supervisors.

In Ref. [1] my contributions are (i) the development and implementation of a flexible numerical method for the calculation of the excluded area between randomly generated hard particles, (ii) the implementation of the unsupervised learning algorithm of Principal Component Analysis, as well as (iii) the implementation and realization of Monte Carlo simulations of polygons with arbitrary shape in the isothermal-isobaric ensemble. Furthermore, I contributed to the text and created all the figures of the manuscript.

In Ref. [2] I implemented the theoretical approaches presented in Ref. [73] including Wertheim's theory and a generalized Flory-Stockmayer theory in order to obtain the bulk phase diagrams and the percolation properties of the investigated mixtures of patchy colloids. Furthermore, the theory of finite sedimentation paths was developed and implemented in order to find the stacking diagrams of binary mixtures at finite height. I created the figures of the manuscript and contributed to the text.

In Ref. [3] I performed both BD simulations of the non-equilibrium system and Monte Carlo simulations of the adiabatic equilibrium system. A main focus lied on the careful splitting of the different force contributions to the one-body force field. Furthermore, I implemented a Power Functional Theory based on the velocity gradient approximation as well as the adiabatic construction in binary systems. I also contributed to the text and created all the figures of the manuscript.

Ref. [4] is the result of my stay at the University of Lisbon for a collaboration with the groups of N. Araújo and M. M. Telo da Gama. I obtained all the results using large scale parallel simulations. In addition, I designed and implemented an analysis with suitable order parameters that reveals the local bonding structure and symmetry of the system. I contributed to the text and the figures of the manuscript.

References

- [1] T. Geigenfeind and D. de las Heras, *J. Chem. Phys.* **150**, 184906 (2019).
- [2] T. Geigenfeind and D. de las Heras, *J. Phys.: Condens. Matter* **29**, 064006 (2017).
- [3] T. Geigenfeind, D. de las Heras, and M. Schmidt, *submitted* (2019).
- [4] T. Geigenfeind, C. Dias, M. Telo da Gama, D. de las Heras, and N. Araújo, *Soft Matter* **14**, 9411 (2018).
- [5] M. Alexander, L. F. Rojas-Ochoa, M. Leser, and P. Schurtenberger, *J. Colloid Interface Sci.* **253**, 35 (2002).
- [6] D. Brutin, B. Sobac, B. Loquet, and J. Sampaol, *J. Fluid Mech.* **667**, 85 (2011).
- [7] I. S. Arvanitoyannis, A. Nakayama, and S. Aiba, *Carbohydr. Polym.* **37**, 371 (1998).
- [8] K. B. Singh, L. R. Bhosale, and M. S. Tirumkudulu, *Langmuir* **25**, 4284 (2009).
- [9] A. Einstein, *Ann. Phys.* **322**, 549 (1905).
- [10] W. Sutherland, *Philos. Mag.* **9**, 781 (1905).
- [11] X. F. Tang, Z. G. Yang, and W. J. Wang, *Colloids Surf. A Physicochem. Eng. Asp.* **360**, 99 (2010).
- [12] J. G. Veinot, H. Yan, S. M. Smith, J. Cui, Q. Huang, and T. J. Marks, *Nano Lett.* **2**, 333 (2002).
- [13] C. E. Reese, C. D. Guerrero, J. M. Weissman, K. Lee, and S. A. Asher, *J. Colloid Interface Sci.* **232**, 76 (2000).
- [14] J. V. Sanders, *Philos. Mag. A* **42**, 705 (1980).
- [15] I. I. Slowing, J. L. Vivero-Escoto, C.-W. Wu, and V. S.-Y. Lin, *Adv. Drug Deliv. Rev.* **60**, 1278 (2008).
- [16] H. Liu, S. K. Kumar, and F. Sciortino, *J. Chem. Phys.* **127**, 084902 (2007).
- [17] J. Cividini, H. J. Hilhorst, and C. Appert-Rolland, *J. Phys. A Math. Theor.* **46**, 345002 (2013).
- [18] B. J. Alder and T. E. Wainwright, *J. Chem. Phys.* **27**, 1208 (1957).
- [19] D. Dendukuri, D. C. Pregibon, J. Collins, T. A. Hatton, and P. S. Doyle, *Nat. Mater.* **5**, 365 (2006).
- [20] S. Sacanna and D. J. Pine, *Curr. Opin. Colloid Interface Sci.* **16**, 96 (2011).
- [21] M. A. Bates and D. Frenkel, *J. Chem. Phys.* **112**, 10034 (2000).

- [22] Y. Martínez-Ratón, S. Varga, and E. Velasco, *Phys. Rev. E* **78**, 031705 (2008).
- [23] P. I. Teixeira and J. M. Tavares, *Curr. Opin. Colloid Interface Sci.* **30**, 16 (2017).
- [24] H. Andersen, *J. Chem. Phys.* **59**, 4714 (1973).
- [25] M. S. Wertheim, *J. Stat. Phys.* **35**, 19 (1984).
- [26] A. van Blaaderen, *Nature* **439**, 545 (2006).
- [27] E. Bianchi, J. Largo, P. Tartaglia, E. Zaccarelli, and F. Sciortino, *Phys. Rev. Lett.* **97**, 168301 (2006).
- [28] Y.-S. Cho, G.-R. Yi, S.-H. Kim, S.-J. Jeon, M. T. Elsesser, H. K. Yu, S.-M. Yang, and D. J. Pine, *Chem. Mat.* **19**, 3183 (2007).
- [29] D. J. Kraft, J. Groenewold, and W. K. Kegel, *Soft Matter* **5**, 3823 (2009).
- [30] Q. Chen, S. C. Bae, and S. Granick, *Nature* **469**, 381 (2011).
- [31] Y. Wang, Y. Wang, D. R. Breed, V. N. Manoharan, L. Feng, A. D. Hollingsworth, M. Weck, and D. J. Pine, *Nature* **491**, 51 (2012).
- [32] H. Pham Van, A. Fortini, and M. Schmidt, *Materials* **10**, 361 (2017).
- [33] V. N. Manoharan, M. T. Elsesser, and D. J. Pine, *Science* **301**, 483 (2003).
- [34] A. P. Philipse, *Curr. Opin. Colloid Interface Sci.* **2**, 200 (1997).
- [35] P. Li, A. Kumar, J. Ma, Y. Kuang, L. Luo, and X. Sun, *Sci. Bull.* **63**, 645 (2018).
- [36] J. Perrin. *Atoms*. Constable, London, 1916.
- [37] R. Piazza, T. Bellini, and V. Degiorgio, *Phys. Rev. Lett.* **71**, 4267 (1993).
- [38] L. Luan, W. Li, S. Liu, and D. Sun, *Langmuir* **25**, 6349 (2009).
- [39] R. Piazza, S. Buzzaccaro, E. Secchi, and A. Parola, *Soft Matter* **8**, 7112 (2012).
- [40] D. de las Heras, N. Doshi, T. Cosgrove, J. Phipps, D. I. Gittins, J. S. van Duijneveldt, and M. Schmidt, *Sci. Rep.* **2**, 789 (2012).
- [41] D. de las Heras and M. Schmidt, *Soft Matter* **9**, 8636 (2013).
- [42] D. de las Heras and M. Schmidt, *J. Phys.: Condens. Matter* **27**, 194115 (2015).
- [43] F. Kogler and S. Klapp, *Europhys. Lett.* **110**, 10004 (2015).
- [44] A. M. Menzel, *J. Phys.: Condens. Matter* **25**, 505103 (2013).
- [45] M. E. Leunissen, C. G. Christova, A. P. Hynninen, C. P. Royall, A. I. Campbell, A. Imhof, M. Dijkstra, R. Van Roij, and A. Van Blaaderen, *Nature* **437**, 235 (2005).
- [46] D. Helbing, P. Molnár, I. J. Farkas, and K. Bolay, *Environ. Plann. B Plann. Des.* **28**, 361 (2001).
- [47] X. D. Liu, W. G. Song, F. Z. Huo, and Z. G. Jiang, *Procedia Eng.* **71**, 343 (2014).

- [48] J. Dzubiella and H. Löwen, *J. Phys.: Condens. Matter* **14**, 9383 (2002).
- [49] J. Chakrabarti, J. Dzubiella, and H. Löwen, *Phys. Rev. E* **70**, 012401 (2004).
- [50] D. Frenkel and B. Smit. *Understanding Molecular Simulation*. Academic Press, London, 2002.
- [51] R. Zwanzig. *Nonequilibrium Statistical Mechanics*. Oxford University Press, New York, 2001.
- [52] R. Evans, *Adv. Phys.* **28**, 143 (1979).
- [53] P. Hohenberg and W. Kohn, *Phys. Rev. B* **136**, 864 (1964).
- [54] W. Kohn and L. J. Sham, *Phys. Rev. A* **140**, 1133 (1965).
- [55] N. D. Mermin, *Phys. Rev. A* **137**, 1441 (1965).
- [56] J. K. Percus, *J. Stat. Phys.* **15**, 505 (1976).
- [57] A. J. Archer, B. Chacko, and R. Evans, *J. Chem. Phys.* **147**, 034501 (2017).
- [58] P. Tarazona, *Phys. Rev. A* **31**, 3148 (1985).
- [59] Y. Rosenfeld, *Phys. Rev. Lett.* **63**, 980 (1989).
- [60] Y. Rosenfeld, M. Schmidt, H. Löwen, and P. Tarazona, *Phys. Rev. E* **55**, 4245 (1997).
- [61] R. Roth, R. Evans, A. Lang, and G. Kahl, *J. Phys.: Condens. Matter* **14**, 12063 (2002).
- [62] N. C. X. Stuhlmüller, T. Ecker, D. de las Heras, and M. Schmidt, *Phys. Rev. Lett.* **121**, 098002 (2018).
- [63] D. de las Heras and M. Schmidt, *Phys. Rev. Lett.* **120**, 028001 (2018).
- [64] M. Schmidt, *J. Chem. Phys.* **143**, 174108 (2015).
- [65] M. Schmidt, *J. Chem. Phys.* **148**, 044502 (2018).
- [66] U. M. D. Marconi and P. Tarazona, *J. Chem. Phys.* **110**, 8032 (1999).
- [67] N. D. Mermin, *J. Phys.: Condens. Matter* **12**, 413 (1999).
- [68] A. J. Archer and R. Evans, *J. Chem. Phys.* **138**, 214101 (2004).
- [69] J. Dzubiella and C. N. Likos, *J. Phys.: Condens. Matter* **15**, L147 (2003).
- [70] A. Fortini, D. de las Heras, J. M. Brader, and M. Schmidt, *Phys. Rev. Lett.* **113**, 167801 (2014).
- [71] J. P. Hansen and I. R. McDonald. *Theory of Simple Liquids*. Elsevier Science, London, 2013.
- [72] M. S. Wertheim, *J. Stat. Phys.* **42**, 477 (1986).
- [73] D. de las Heras, J. M. Tavares, and M. M. Telo da Gama, *Soft Matter* **7**, 5615 (2011).

- [74] D. de las Heras, J. M. Tavares, and M. M. Telo da Gama, *Soft Matter* **8**, 1785 (2012).
- [75] N. F. Carnahan and K. E. Starling, *J. Chem. Phys.* **51**, 635 (1969).
- [76] G. A. Mansoori, N. F. Carnahan, K. E. Starling, and T. W. Leland, *J. Chem. Phys.* **54**, 1523 (1971).
- [77] A. Coniglio, L. de Arcangelis, E. del Gado, A. Fierro, and N. Sator, *J. Phys.: Condens. Matter* **16**, S4831 (2004).
- [78] P. J. Flory, *J. Am. Chem. Soc.* **63**, 3083 (1941).
- [79] W. H. Stockmayer, *J. Chem. Phys.* **11**, 45 (1943).
- [80] J. M. Tavares, P. I. Teixeira, and M. M. Telo da Gama, *Phys. Rev. E* **81**, 010501 (2010).
- [81] L. Onsager, *Ann. N. Y. Acad. Sci.* **51**, 627 (1949).
- [82] S. Wold, K. Esbensen, and P. Geladi, *Chemom. Intell. Lab. Syst.* **2**, 37 (1987).
- [83] N. H. Timm. *Applied Multivariate Analysis*. Springer, New York, 2002.
- [84] P. R. Halmos, *Am. Math. Mon.* **70**, 241 (1963).
- [85] I. T. Jolliffe. *Graphical representation of data using principal components*. Springer, New York, 2002.
- [86] J. A. Anderson, J. Antonaglia, J. A. Millan, M. Engel, and S. C. Glotzer, *Phys. Rev. X* **7**, 021001 (2017).

3 Publications

This chapter contains the full versions of the four papers contributing to the cumulative Thesis. To this moment, three of those papers have already been published and one has been submitted.

[1]	<i>Principal Component Analysis of the excluded area of two-dimensional hard particles.</i> T. Geigenfeind and D. de las Heras, <i>J. Chem. Phys.</i> 150 , 184906 (2019)	43
[2]	<i>The role of sample height in the stacking diagram of colloidal mixtures under gravity.</i> T. Geigenfeind and D. de las Heras, <i>J. Phys.: Condens. Matter</i> 29 , 064006 (2017)	55
[3]	<i>Superadiabatic demixing in nonequilibrium colloids.</i> T. Geigenfeind, D. de las Heras, and M. Schmidt, <i>submitted</i> (2019)	67
[4]	<i>Crossover from three- to six-fold symmetry of colloidal aggregates in circular traps.</i> T. Geigenfeind, C. S. Dias, M. M. Telo da Gama, D. de las Heras, and N. A. M. Araújo, <i>Soft Matter</i> 14 , 9411 (2018)	83

Principal component analysis of the excluded area of two-dimensional hard particles

Cite as: J. Chem. Phys. 150, 184906 (2019); doi: 10.1063/1.5092865

Submitted: 15 February 2019 • Accepted: 22 April 2019 •

Published Online: 14 May 2019



View Online



Export Citation



CrossMark

Thomas Geigenfeind and Daniel de las Heras^{a)} 

AFFILIATIONS

Theoretische Physik II, Physikalisches Institut, Universität Bayreuth, D-95440 Bayreuth, Germany

^{a)}delasheras.daniel@gmail.com. URL: www.danieldelasheras.com

ABSTRACT

The excluded area between a pair of two-dimensional hard particles with given relative orientation is the region in which one particle cannot be located due to the presence of the other particle. The magnitude of the excluded area as a function of the relative particle orientation plays a major role in the determination of the bulk phase behavior of hard particles. We use principal component analysis (PCA) to identify the different types of excluded areas corresponding to randomly generated two-dimensional hard particles modeled as non-self-intersecting polygons and star lines (line segments radiating from a common origin). Only three principal components are required to have an excellent representation of the value of the excluded area as a function of the relative particle orientation for sufficiently anisotropic particles. Independent of the particle shape, the minimum value of the excluded area is always achieved when the particles are antiparallel to each other. The property that affects the value of the excluded area most strongly is the elongation of the particle shape. PCA identifies four limiting cases of excluded areas with one to four global minima at equispaced relative orientations. We study selected particle shapes using Monte Carlo simulations.

Published under license by AIP Publishing. <https://doi.org/10.1063/1.5092865>

I. INTRODUCTION

Hard body models, for which the interaction potential is infinite if two particles overlap and zero otherwise, are excellent candidates to model colloidal particles, which are dominated by excluded volume. Hard body models are also relevant to understand how the microscopic properties at the particle level determine the macroscopic properties of the system such as its bulk phase behavior. Since the then unexpected classical result of fluid-solid phase transition in a system of hard spheres,¹ the bulk phase behavior of several three-dimensional hard body models has been analyzed by both computer simulations and theoretical approaches such as density functional theory. Anisotropic hard particles form a surprisingly rich variety of mesophases such as uniaxial, biaxial, and cubatic nematics, as well as cholesteric, smectic, and columnar phases. We refer the reader to Ref. 2 for a recent review on phase equilibria of hard body models.

The phase behavior of several two-dimensional hard models has been also reported in the literature. Examples are hard disks,^{3–5} needles,⁶ rectangles,^{7–9} discorectangles,^{7,10,11} triangles,^{12,13} squares,¹⁴ rounded squares,¹⁵ pentagons,¹⁶ hexagons,^{17,18} ellipses,¹⁹ zigzags,²⁰ hockey sticks,²¹ bananalike,²² and allophiles.²³

Phase transitions in hard bodies are driven by entropy. At sufficiently low density, the entropy of the ideal gas dominates, and the system remains isotropic with neither positional nor orientational order. As the density increases, excluded volume effects become more important and the gain in configurational entropy can drive a transition to a phase with orientational and/or positional order.

The study of excluded volume effects in hard bodies starts with the properties of the excluded volume between two particles, which plays a role similar to the pair interaction potential in soft systems (i.e., with continuous interaction potentials). Here, we restrict ourselves to two-dimensional particles. As a result of the potential being infinite if two particles overlap, there exists around each particle an exclusion region in which no other particle can be located. The phase behavior of the system is determined by the ideal gas entropy and the properties of this complicated many-body exclusion region, which depends on the positions and orientations of all particles in the system. Within a mean fieldlike approach, the properties of the many-body exclusion region are fully characterized by the excluded area, which is the area inaccessible to one particle due to the presence of another particle. The excluded area alone does not determine

the complete phase behavior of the system, but it plays a vital role in the determination of the type of stable phases. The value of the excluded area, A_{exc} , depends on the particle shape. For a given particle shape, A_{exc} is a function of the relative orientation between the two particles, ϕ . For example, the value of the excluded area between two rectangles is minimum if their relative angle ϕ is either 0 (parallel) or π (antiparallel). For squares, the value of the excluded area is minimum if $\phi = 0, \pi/2, \pi,$ and $3\pi/2$. Although different particle shapes might generate different excluded areas, it is evident that not any function $A_{\text{exc}}(\phi)$ corresponds to a valid particle shape (e.g., the value of the excluded area cannot be negative). We investigate here the admissible shapes of the function $A_{\text{exc}}(\phi)$. To this end, we apply principal component analysis^{24,25} (PCA) to a set of excluded areas corresponding to randomly generated two-dimensional hard bodies. PCA is an unsupervised learning algorithm intended to simplify the complexity of a high-dimensional data set. Mathematically, PCA is an orthogonal transformation of the data to a new basis in which the basis vectors are sequentially chosen such that the variance of the projection of the original data onto the new basis vectors is as large as possible. As a result of our PCA, we identify four special or limiting types of excluded area with one to four global minima as a function of the relative orientation. Finally, we perform Monte Carlo (MC) simulations for selected particle shapes.

II. METHODS

We aim to find the relevant types of excluded areas $A_{\text{exc}}(\phi)$ in two dimensions. To this end, we first generate random hard particles, and then apply principal component analysis to the excluded area between two identical particles.

A. Particle generation

We generate two-dimensional hard particles following either of two procedures. In the first one, each particle is modeled as a simple (non-self-intersecting) polygon, as sketched in panels (a) and (b) of Fig. 1. A polygon is defined by a closed and ordered set of m random vertices connected via straight edges. For each polygon, the

coordinates of each vertex $\mathbf{x}_i, i = 1, \dots, m$ are obtained by sampling from uniform distributions a random radius $r_i \in (0, 1]$ and a random angle $\phi_i \in [0, 2\pi]$. We allow both convex and concave shapes, but restrict the set to simple, non-self-intersecting, polygons, i.e., the line segments connecting the vertices of a polygon are not allowed to intersect (apart from the end points of two neighboring edges that are joint at one vertex). Furthermore, no two vertices have the exact same coordinates. If the random creation of vertices of a polygon leads to self-intersections, we perform Lin 2-opt moves until all intersections are removed. The algorithm was initially proposed to solve the salesman problem,^{26,27} and it works as follows: Assume the line segment connecting vertices \mathbf{x}_{i-1} and \mathbf{x}_i and the line segment connecting vertices \mathbf{x}_{j-1} and \mathbf{x}_j intersect ($j - i > 1$ and periodic vertices). Then, we reverse the order of all vertices between i and j , i.e., the sequence $\{i - 1, i, \dots, j - 1, j\}$ becomes $\{i - 1, j - 1, \dots, i, j\}$. We perform as many Lin 2-opt moves as required to remove all self-intersections.

To increase the spectrum of particle shapes, we also generate particles modeled as star lines; see Fig. 1(c). A star line has a center \mathbf{x}_0 connected via line segments to m vertices located at $\mathbf{x}_i, i = 1, \dots, m$. The simple polygons contain the star lines as a limiting case of polygons with zero area. However, it is very unlikely to generate a star line with the method we use to generate polygons.

As a final step, each particle (polygons and star lines) is rescaled to the maximum possible size that fits in a square bounding box of length $h = 1$, which defines our unit of length.

B. Computation of the excluded area

In what follows and for simplicity, we refer to $A_{\text{exc}}(\phi)$ as simply the excluded area. To calculate the excluded area between two particles (let them be polygons or star lines) at a given relative orientation ϕ , we use the fact that whenever two identical particles overlap then at least two edges intersect. We first fix the relative orientation between two particles ϕ , and the position of particle 1 (at the origin).

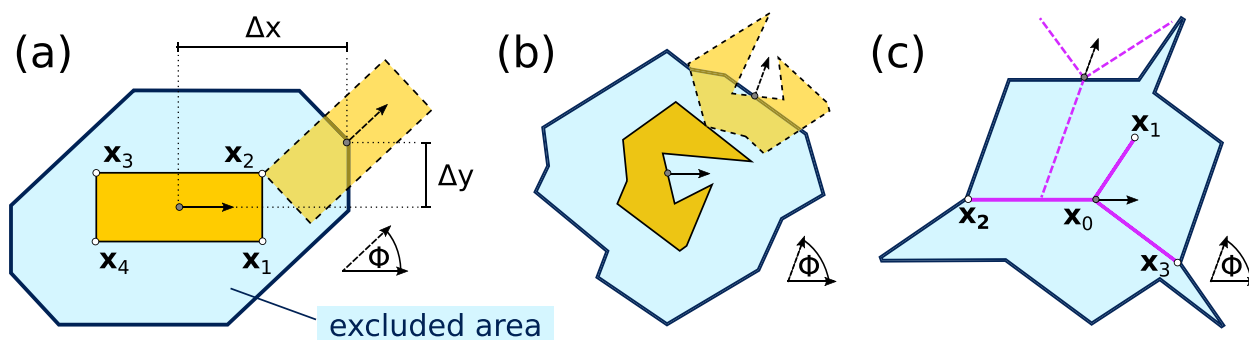


FIG. 1. Excluded area. (a) A rectangle (solid orange) with vertices (empty circles) at $\mathbf{x}_i, i = 1, 2, 3, 4$ and a second identical rectangle (dashed orange) shifted by $(\Delta x, \Delta y)$ and rotated by ϕ with respect to the first particle. The blue area is a graphical representation of the excluded area for the center of the second rectangle at this relative orientation. The black arrow indicates the orientation of the particles (with respect to an arbitrary axis). (b) Graphical representation of the excluded area (at a given relative orientation) of a non-self-intersecting polygon with 10 randomly generated vertices. (c) Excluded area of a randomly generated star line (magenta) with three vertices \mathbf{x}_i connected to the point \mathbf{x}_0 .

Next, we fix the y -distance between the two particles Δy and calculate the interval(s) in x for which the two particles overlap. We loop over all pairs of edges between particles 1 and 2 checking for which x -distances between the particles Δx the edges overlap. The distance Δx (Δy) is calculated as the separation in \hat{x} (\hat{y}) between two reference points located in the particles such as, e.g., the centers of masses. For a fixed value of Δy , a pair of edges intersects either not at all or in at most one connected interval of Δx . The bounds of this interval represent the cases for which a vertex of one edge lies on top of the other edge. Hence, the interval in Δx for which two edges overlap can be obtained by checking the values of Δx for which each of the four involved vertices lies on top of the other edge. Combining the overlapping intervals of all possible pairs of edges gives the complete overlap in the x -direction for a given value of Δy .

Next, we move particle 2 in the y -direction in discrete steps of size $\Delta h \approx 5 \times 10^{-4}$ between $\Delta y_{\min}(\phi)$ and $\Delta y_{\max}(\phi)$ which are the minimum and maximum values of Δy for which overlap is possible, respectively. Δy_{\min} (Δy_{\max}) occurs when the vertex with the highest (lowest) y -coordinate of particle 2 and that with the lowest (highest) y -coordinate of particle 1 have the same y -coordinate.

Integrating the overlapping intervals between Δy_{\min} and Δy_{\max} yields the excluded area for the selected orientation. Finally, we repeat the process for $n_\phi = 360$ relative orientations $\phi \in [0, 2\pi]$ between the particles and normalize the excluded area according to

$$\frac{1}{2\pi h^2} \int_0^{2\pi} A_{\text{exc}}(\phi) d\phi = 1. \quad (1)$$

C. Principal component analysis

We apply principal component analysis^{24,25} to the excluded areas $A_{\text{exc}}(\phi)$ generated by the above method. All data are organized in a data matrix \mathbf{X} . Each row contains one sample, i.e., the excluded area as a function of the relative orientation for one randomly generated particle. In each column, we store the values of the excluded areas at a given relative orientation for all samples in the system. First, the data are centered to facilitate the following calculations. That is, from each column of \mathbf{X} , the mean is subtracted. We then apply the PCA algorithm. PCA uses an orthogonal transformation to represent the data in a new orthogonal basis. In this basis, the first basis vector \mathbf{w}_1 (first principal axis) is chosen such that the variance of the projection of the data onto this vector is as large as possible, that is,

$$\mathbf{w}_1 = \arg \max_{\|\mathbf{w}_1\|=1} \{\|\mathbf{X}\mathbf{w}_1\|^2\} = \arg \max_{\|\mathbf{c}_1\|=1} \{\|\mathbf{c}_1\|^2\}. \quad (2)$$

Here, the i th component of the vector \mathbf{c}_1 is the first principal component of the i th sample. The variance of the following basis vectors, \mathbf{w}_j with $j > 1$, is also maximized under the constraint that each vector is orthogonal to the preceding ones. The new basis vectors are called principal axes, and the components of a vector expressed in this basis are the principal components. It is often the case that only the first principal components have high variance and are therefore relevant to describe the data. Hence, PCA allows a meaningful dimension reduction, while retaining as much information as possible.

Mathematically, the principal axes are the (normalized) eigenvectors of the covariance matrix \mathbf{C} of the data, which is defined as

$$\mathbf{C} = \frac{1}{n_s - 1} \mathbf{X}^\top \mathbf{X} \quad (3)$$

with n_s being the number of samples (rows) of the data matrix \mathbf{X} . The variance of the projection of \mathbf{X} onto a principal axis is

$$\text{var}\{\mathbf{X}\mathbf{w}_i\} = \mathbf{w}_i^\top \mathbf{C} \mathbf{w}_i. \quad (4)$$

The covariance matrix is symmetric and therefore diagonal in the basis formed by its eigenvectors. Hence, using Eq. (4), one can see that the eigenvalues of \mathbf{C} are simply the variance of the respective principal component.^{25,28} For the actual implementation of PCA, we use the OpenCV library.²⁹

III. RESULTS

We start the results section analyzing the excluded area of regular polygons. Next, we show the PCA of the excluded area of randomly generated particles. We end the section with Monte Carlo simulations of selected particle shapes.

A. Regular polygons

The normalized values of the excluded areas for a line segment and for the regular polygons with 3–6 vertices are presented in Fig. 2. To check the accuracy of the numerical calculation of the excluded area, we have compared the numerical results against analytic expressions for line segments, equilateral triangles, and squares; see Figs. 2(b) and 2(c).

For regular polygons, the excluded area contains as many minima (and maxima) as vertices of the polygon since the rotational symmetry of the particle is also present in the excluded area. The excluded area of the line segment is a direct extension of this trend as it contains two minima (and two maxima).

All the excluded areas are symmetric with respect to the relative orientation $\phi = \pi$. This is a general property of the excluded area between any two identical particles that can be easily understood as follows. The relative orientations $-\phi$ and ϕ are degenerated as they correspond to an (irrelevant) swap of the two identical particles. Hence, the excluded area is symmetric with respect to $\phi = 0$, which implies also the symmetry with respect to $\phi = \pi$. Therefore, although in Fig. 2 we present the excluded area of particles with mirror symmetry, the symmetry of the excluded area around $\phi = \pi$ is also present for particles with no spatial symmetries.

As expected, the difference between the maximum value and the minimum value of the excluded area of regular polygons decreases by increasing the number of vertices of the regular polygon. The limit of a regular polygon with an infinite number of vertices is a disk, for which the excluded area does not depend on the relative orientation. The difference in the excluded area for different orientations is correlated with the increase in configurational entropy that occurs when the particles organize in a state with orientational order. Hence, ordering effects are stronger for particles with more variance in $A_{\text{exc}}(\phi)$. For example, in Ref. 30, Anderson *et al.* found that regular polygons with more than 6 vertices already melt like disks.

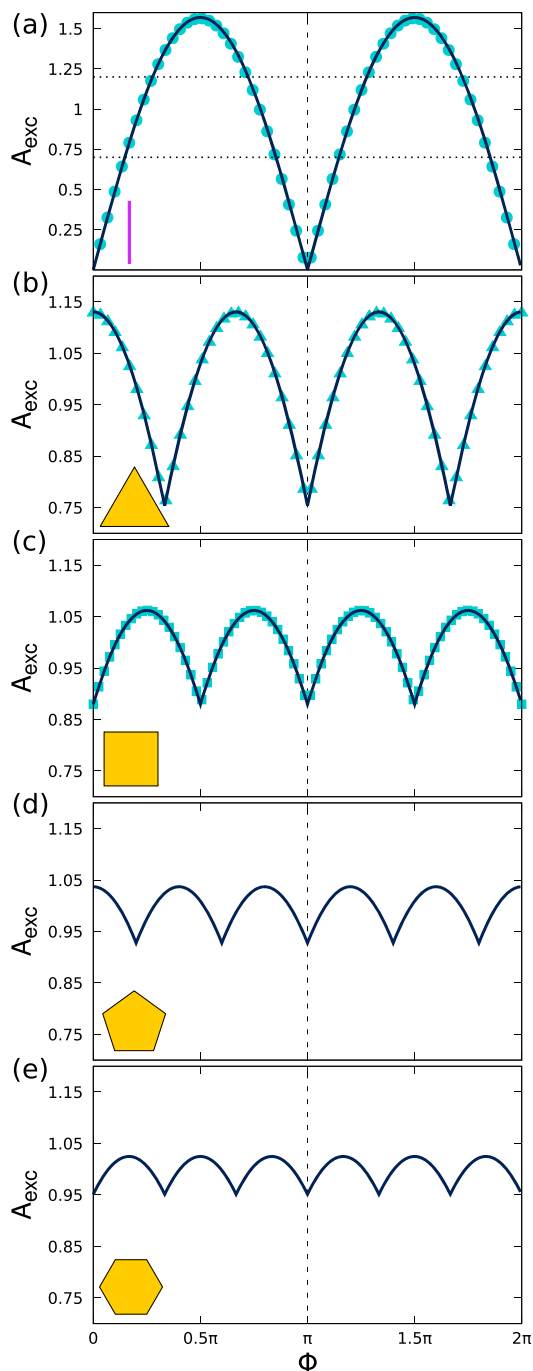


FIG. 2. Normalized excluded area for regular polygons as a function of the relative orientation ϕ : (a) line segment, (b) equilateral triangle, (c) square, (d) pentagon, and (e) hexagon. The insets show the particles. Solid lines are numerical results. The symbols are analytic expressions of the excluded area of a line segment (a), an equilateral triangle (b), and a square (c). The dotted horizontal lines in (a) indicate the vertical range used in panels (b)–(e).

B. Principal component analysis

In what follows, we show the result of the PCA applied to a set of 9.3×10^4 randomly generated particles of which 4.8×10^4 are polygons with a number of vertices uniformly distributed between 3 and 10, and 4.5×10^4 are star lines. An example of a non-self-intersecting polygon with 10 vertices is shown in Fig. 1(b). The number of vertices of the star lines is uniformly distributed between 2 and 10. We investigated 10 different sets, each one containing the same number of randomly generated particles. All sets produced the same results up to small numerical inaccuracies.

As described in Sec. II C, the first step in PCA consists of centering the data by removing the column-wise mean of the data matrix. The mean excluded area $m(\phi)$ [see Fig. 3(a)] has a global minimum at $\phi = \pi$ and a local minimum at $\phi = 0$. The mean excluded area manifests a common feature of all excluded areas we have calculated. The excluded area between two identical particles has always the global minimum at $\phi = \pi$, regardless of the shape of the particles. This intuitive feature has been proven for convex shapes.³¹ Our particles are both convex and concave, and we have always observed the global minimum to be located at $\phi = \pi$.

Panels (b)–(d) of Fig. 3 show the first three principal axes $w_i(\phi)$, $i = 1, 2, 3$. The first (b) and third (d) principal axes have qualitatively similar shapes to the excluded area of a line segment [Fig. 2(a)] and of an equilateral triangle [Fig. 2(b)], respectively. The second principal axis $w_2(\phi)$ [Fig. 3(c)] has a pronounced minimum at $\phi = \pi$. Excluded areas with this feature play an important role in the PCA analysis, as we discuss below. A data file with the mean excluded area and the first three principal components can be found in the [supplementary material](#).

In Fig. 4, a semilogarithmic plot of the eigenvalues of the first 10^2 principal axes is presented. The first and the second eigenvalue differ in one order of magnitude, and higher order eigenvalues decrease very fast in magnitude. Given that (i) the eigenvalue of a principal axis is the variance of the respective principal component^{25,28} and that (ii) the eigenvalues decrease very fast in magnitude (Fig. 4), we achieve a good representation of the excluded area using only the first three principal components. A measure of how well the data are represented using the first n components is the explained variance σ_n , which is the sum of the eigenvalues associated with the n first principal components divided by the sum of all eigenvalues. In our case, using three principal components, we find $\sigma_3 \approx 0.98$ and therefore we are confident that most of the full information is already contained in the first three components. Using the principal components of a given particle, its approximated excluded area can be reconstructed by calculating the sum of the first three principal axes [see Figs. 3(b)–3(d)] multiplied with their respective principal components and adding the mean [Fig. 3(a)]. In other words, the reconstructed excluded area $A_{\text{exc}}^{\text{rec}}$ is a linear combination of the principal axes and the mean (see Fig. 3), with the principal components being the coefficients of the linear combination

$$A_{\text{exc}}^{\text{rec}}(\phi) = m(\phi) + \sum_{i=1}^3 c_i w_i(\phi). \quad (5)$$

The average L_1 error

$$s_{L_1} = \langle |A_{\text{exc}}(\phi) - A_{\text{exc}}^{\text{rec}}(\phi)| \rangle \quad (6)$$

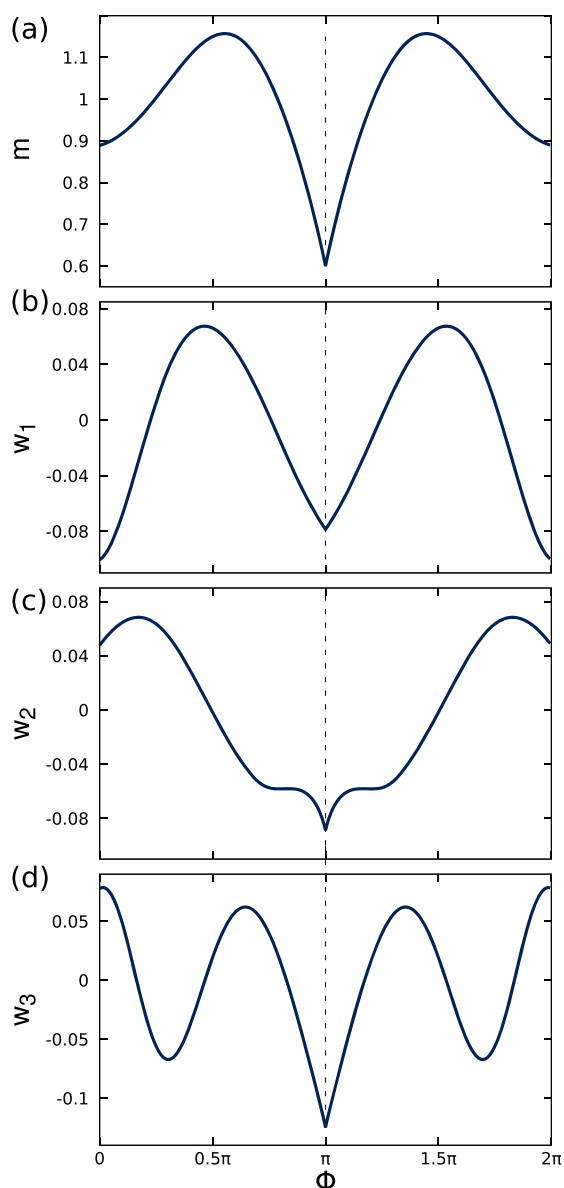


FIG. 3. Mean excluded area m (a), first w_1 (b), second w_2 (c), and third w_3 (d) principal axes as a function of the relative orientation between particles ϕ .

between the calculated values of the excluded areas $A_{\text{exc}}(\phi)$ and their reconstructions $A_{\text{exc}}^{\text{rec}}(\phi)$ is 0.012. Here, the average is taken over all orientations ϕ and over all samples. We show examples of the reconstructed excluded area for relevant particle shapes below.

In Fig. 5, we present the first three principal components c_i , $i = 1, 2, 3$ of the excluded area of all particles in the set. Each point represents the excluded area $A_{\text{exc}}(\phi)$ of one particle of the set.

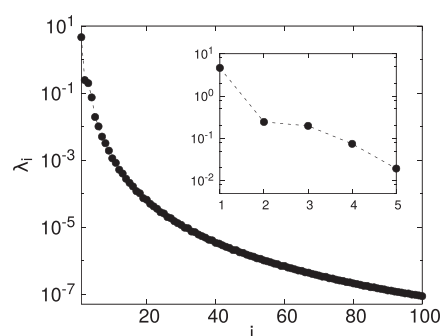


FIG. 4. Semilog plot of the first 10^2 eigenvalues λ_i vs the index i . The inset is a close view of the first five eigenvalues.

We also show two-dimensional projections onto the c_1 - c_2 , c_1 - c_3 , and c_2 - c_3 planes. The excluded areas are contained in a simply connected region with no holes and a well-defined boundary with four prominent limiting cases (highlighted by red squares in Fig. 5). We discuss in what follows these special limiting excluded areas found with PCA, together with their associated particle shapes.

1. First limiting case

As indicated by the eigenvalues, the first principal component c_1 has the by far highest variance with values between -3 and 7.5 . One vertex of the 3D projection of the excluded area [Fig. 5] corresponds to the line segment, which is the limiting case for which c_1 is maximized. In general, the value of the c_1 component increases with the elongation of the particles. According to PCA, the elongation of a particle is therefore the most important geometric feature influencing the excluded area. The excluded areas of the particles near this limiting case possess two well-defined minima, like in the case of a line segment shown in Fig. 2(a).

2. Second limiting case

Maximizing the second principal component c_2 is another limiting case of the 3D projection; see Fig. 5. An illustrative excluded area and its corresponding particle shape are presented in Fig. 6. The excluded areas in this region are characterized by a pronounced global minimum located at $\phi = \pi$ and a global maximum near $\phi = 0$. In Fig. 6, both the actual excluded area and the reconstruction using only the first three principal components are shown. The real excluded area has secondary minima that are not captured by the reconstructed excluded area. However, the overall agreement is very good and it justifies the use of only three principal components. The secondary features that are not reproduced by the reconstructed excluded area might play a role in the determination of the structure of phases with positional order, but it is less likely that they will affect the relative stability of fluid mesophases with only orientational order.

The particles in this region of the 3D projection are line stars with three arms. It might be possible to eliminate the secondary minima using shapes with curved lines (similar to the symbol ϵ). The shape of the excluded area $A_{\text{exc}}(\phi)$ suggests that the particles prefer a state where the neighboring particles are antiparallel.

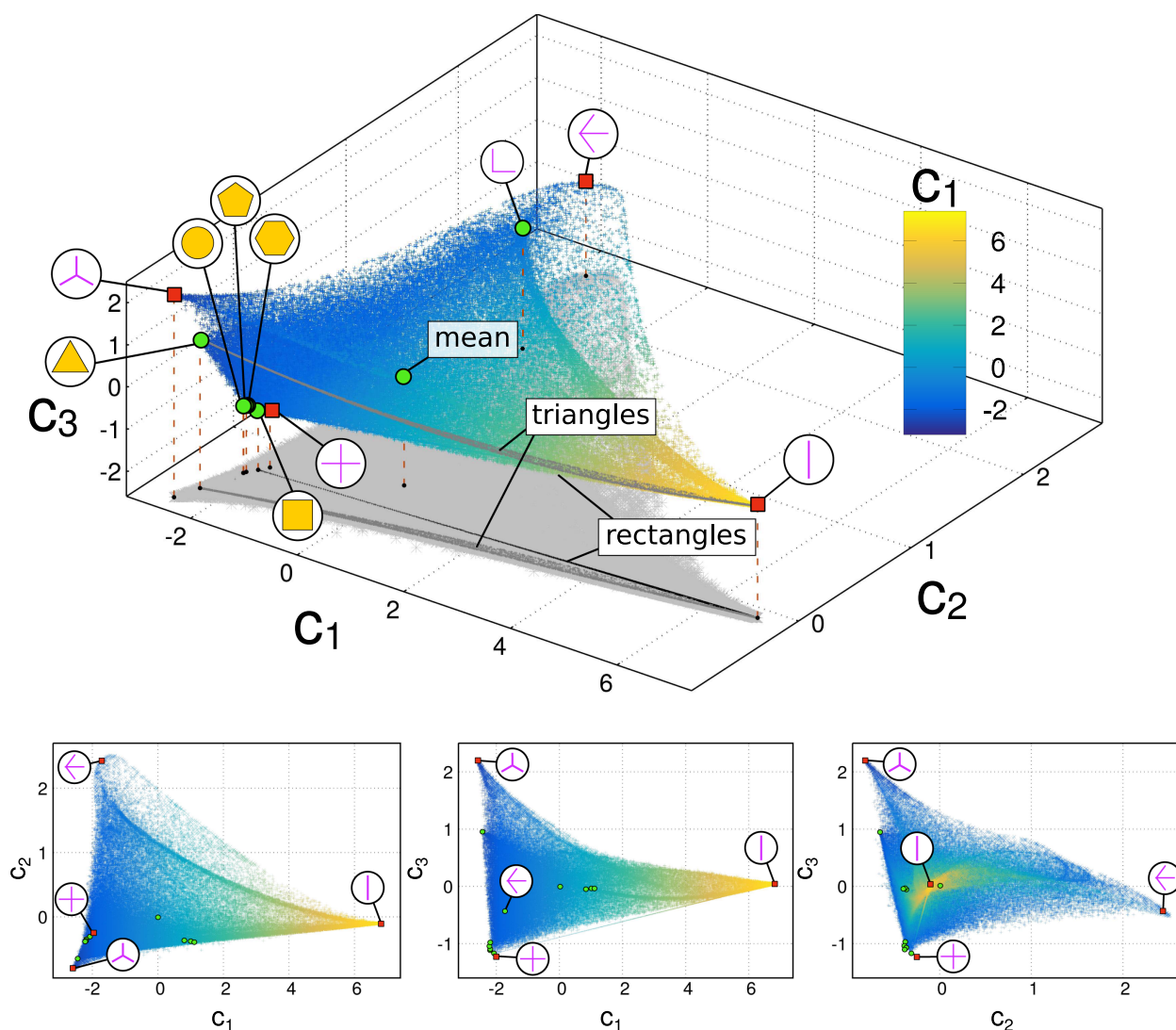


FIG. 5. Excluded areas in the space of the first three principal components. Top: The set of all values of the excluded area $A_{\text{exc}}(\phi)$ represented with the first three principal components c_i , $i = 1, 2, 3$. Each point represents one excluded area of the data set and is therefore associated to one particle shape. The color code indicates the value of the first principal component c_1 . Green circles show the values of the excluded areas of selected particles, as indicated. Red squares indicate the four limiting cases analyzed in the text. In light gray, a projection onto the c_1 - c_2 plane is shown. In dark gray, a projection of the excluded areas of triangles and rectangles is shown. Bottom: Two dimensional projections of the excluded areas onto the c_1 - c_2 (left), c_1 - c_3 (middle), and c_2 - c_3 planes.

A fluid of three-dimensional hard boomeranglike particles can form a biaxial nematic phase.³² In two dimensions, boomeranglike particles can be created by a star line with two arms at an angle of approximately 90° . In the space of the first three principal components, these particles are located relatively close to the second limiting case (see Fig. 5). The excluded area (not shown) has a prominent minimum at $\phi = \pi$, a local minimum if the particles are parallel $\phi = 0$, and depending on the relative angle between the two arms local minima at $\phi \approx \pi/2$ and $3\pi/2$. The presence of these local minima could stabilize a tetratic phase.

3. Third limiting case

For the third limiting case emphasized by PCA, both c_1 and c_2 are minimal. The excluded areas located in this region have three pronounced equidistant minima. Before further discussing this case, we first have a look at the excluded areas for polygons with three vertices, i.e., triangles, which are closely related.

The excluded areas of triangles in the base of the first three principal axes are highlighted in dark gray in Fig. 5 and also represented in Fig. 7(a). All the excluded areas of triangles form a

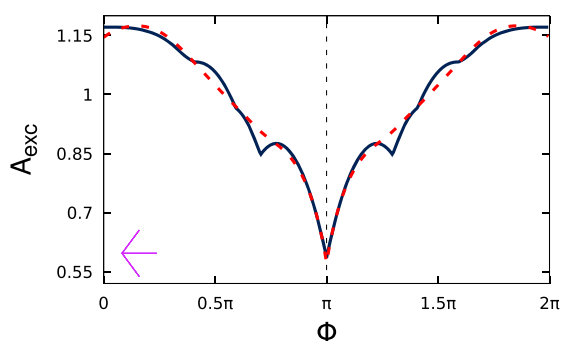


FIG. 6. Excluded area (solid black line) and reconstructed excluded area using the first three principal components (dashed red line) as a function of the relative orientation ϕ for the particle presented in magenta (left bottom corner).

simply connected two-dimensional region which spans between the two limiting cases given by a line segment and an equilateral triangle. These limiting cases correspond to triangles with the maximum (line segment) and minimum (equilateral triangle) possible aspect ratios. Going from the equilateral triangle to the line segment implies increasing the aspect ratio of a regular triangle. There are two special ways of elongating an equilateral triangle: (i) taking one side and

moving it away from the opposite vertex, making the angle at the apex in the resulting acute isosceles triangle very small, and (ii) taking one side and moving its two corresponding vertices away from each other along the direction of this side, creating an obtuse isosceles triangle where the angle at the apex is very large. In both cases, the intermediate triangles are isosceles and their excluded areas form the boundary of the 3D projection in the base of principal components; see Fig. 7(a). We have shown in Fig. 2(b) the excluded area of an equilateral triangle, which has three global minima at $\{\pi/3, \pi, 5\pi/3\}$ and three global maxima. In Fig. 7(b), we present the excluded area of other representative triangles. In panel (b1), we show an obtuse isosceles triangle. The excluded area has only one global minimum at $\phi = \pi$. The global minima of A_{exc} at $\pi/3$ and $5\pi/3$ of an equilateral triangle are now local minima and have moved to a different relative orientation. In panel (b2), we represent the excluded area of an acute isosceles triangle. There is only one global minimum at $\phi = \pi$, and the position of the secondary minima is also shifted with respect to that in an equilateral triangle. In panel (b3), we present a non-isosceles triangle, which in the PCA analysis is located between the two previous cases (b1) and (b2); see Fig. 7(a). The excluded area has characteristics of both acute and obtuse triangles. In all three cases, the reconstructions of the excluded areas neglect small features like the presence of local minima and kinks, but the overall agreement between the actual excluded area and that obtained with only three principal components is excellent.

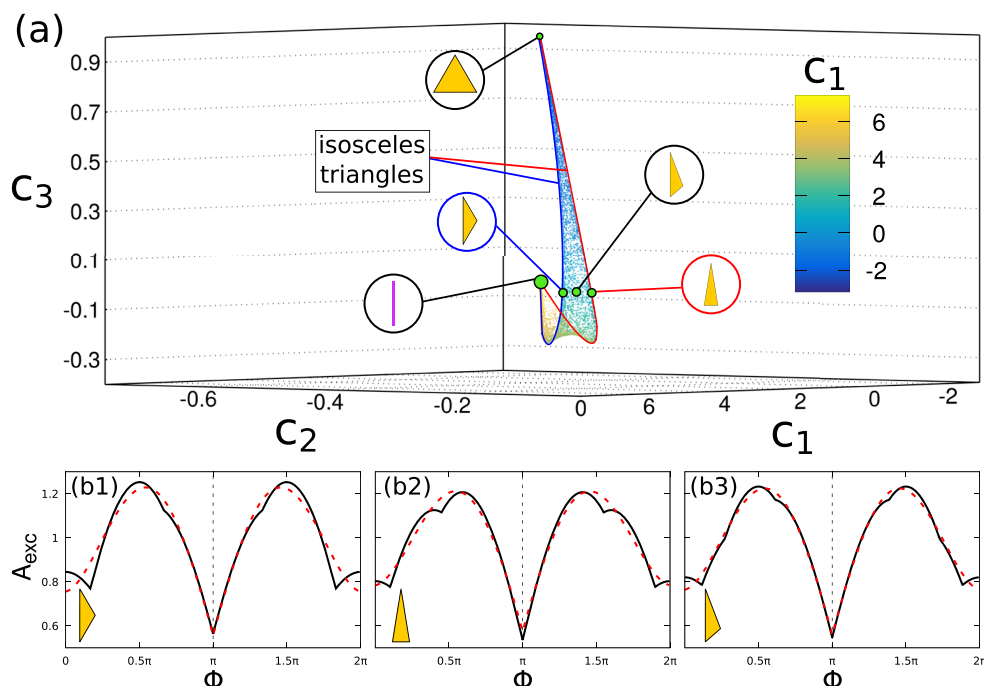


FIG. 7. (a) Excluded areas of triangles represented with the first three principal components, c_1 , c_2 , and c_3 . Each point represents the excluded area of one randomly generated triangle. The color indicates the value of the first principal component c_1 . Green circles indicate the position in the space of principal components of the excluded areas corresponding to the depicted particle shapes. The blue (red) curve indicates the location of all obtuse (acute) isosceles triangles. Bottom panels: Excluded areas (solid black line) and reconstructions using the first three principal components (dashed red line) as a function of the relative orientation ϕ for three particular triangles (represented in the left bottom corner of each panel).

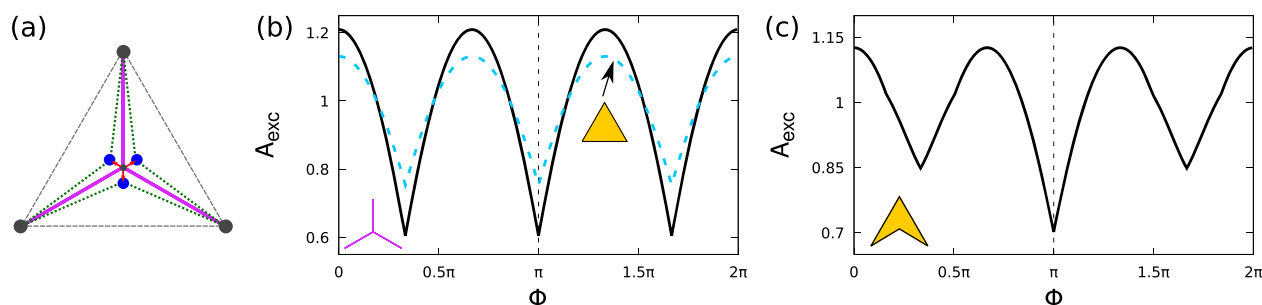


FIG. 8. (a) Schematic of the third limiting case highlighted by PCA: a star line with three identical segments rotated by $2\pi/3$ (magenta) such that the outer vertices lie on top of an equilateral triangle (dashed gray). Splitting the inner vertex into three vertices (blue dots) creates a new particle shape (dotted green). (b) Excluded area for a star line with three identical segments (solid black) and an equilateral triangle (dashed blue) as a function of the relative orientation ϕ . The star line is represented in magenta (bottom left corner). (c) Excluded area of an arrowlike particle, as shown in the bottom left corner.

In the space of principal components (see Fig. 5), the excluded area of an equilateral triangle is located in the region where both c_1 and c_2 are low, near the third limiting case for which c_1 and c_2 are minimal and c_3 is maximal. At this location, we find the excluded area of a star line particle made of three identical segments, any two of them forming an angle of $2\pi/3$. A sketch of the particle is presented in Fig. 8(a) together with the corresponding excluded area [Fig. 8(b)]. The excluded area resembles that of an equilateral triangle (also shown in the figure for comparison). Due to the normalization [Eq. (1)], the excluded area of the star line appears to have a larger variance (difference between the maximum and the minimum values of the excluded area). However, when normalizing the excluded area with the height of the particles, both excluded areas have the same variance. Strong differences are expected for three-body interactions and higher order terms. Hence, a comparison between the bulk phase behavior of this particle shape and that of equilateral triangles might help to understand the role of higher than two-body correlations on the bulk phase behavior.

Another interesting property of this kind of particles is that the star line can be continuously deformed by splitting its center and moving the resulting vertices radially toward the sides [see Fig. 8(a)]. As a special case, this includes particles where two of the inner vertices are located on top of the connecting line between two of the outer vertices. The resulting particles have four vertices and the shape of an arrow. The excluded area of such arrowlike particles is shown in Fig. 8(c). The main difference compared to the undeformed star particle is that the depth of two of the minima has decreased. However, the minima are still located at the same orientations as in the initial star line. This is in contrast to the case of triangles discussed above, for which any deformation simultaneously changes the depth of the two secondary minima as well as the relative orientations at which they occur. In this case, there is a complete family of particles in which the depth of the secondary minima can be tuned while keeping their location (relative orientation) fixed. Particles of this type could present an isotropic-triatic transition by increasing the density and then a second transition toward a uniaxial state at even higher densities.

4. Fourth limiting case

The last limiting excluded area according to PCA (see Fig. 5) occurs when c_3 is minimal. In this region, a number of special particles are located. Among them, we find disks, which have a completely flat excluded area independent of the relative orientation. Regular pentagons and hexagons together with other regular polygons with more vertices are located near the disk. This can be explained with the decreasing variance of the excluded area of regular polygons by increasing the number of sides, cf. Fig. 2. For example, the difference between the maximum and the minimum value of the excluded area for a line segment is approximately 1.57, whereas for the hexagon, it is approximately 0.07. It is therefore not surprising that extra principal components are required to have a good representation of the excluded areas in this region. As an example, we show in Fig. 9 the excluded area of pentagons and hexagons together with their reconstructed excluded areas. Up to six principal components are required to have a good approximation of the excluded area of hexagons.

The regular polygon with the lowest value of c_3 is the square. In the space of principal components [Fig. 5], there is a continuous curve containing all possible rectangles. At the end points of this curve, we find the square and the line segment, which are the rectangles with the minimal and maximal length-to-width aspect ratios, respectively.

We have shown above two particle shapes, an equilateral triangle and a star line with three identical segments that share very similar excluded areas; see Fig. 8(a). A similar behavior occurs for the case of a square and a star line with four identical segments forming the shape of a plus; see Fig. 10. The excluded area of the plus particle resembles that of the square but with higher variance (see a comparison in Fig. 10). The observed trend of decreasing variance in the excluded area for regular polygons as the number of sides increases holds also for the case of regular star lines.

The particle shapes of the four limiting excluded areas we have discussed above are well defined. This, however, is not the case for most excluded areas since different particle shapes can give rise to the same or almost the same excluded area. That two different hard bodies can produce the same excluded volume has been recently proven for convex bodies.³³

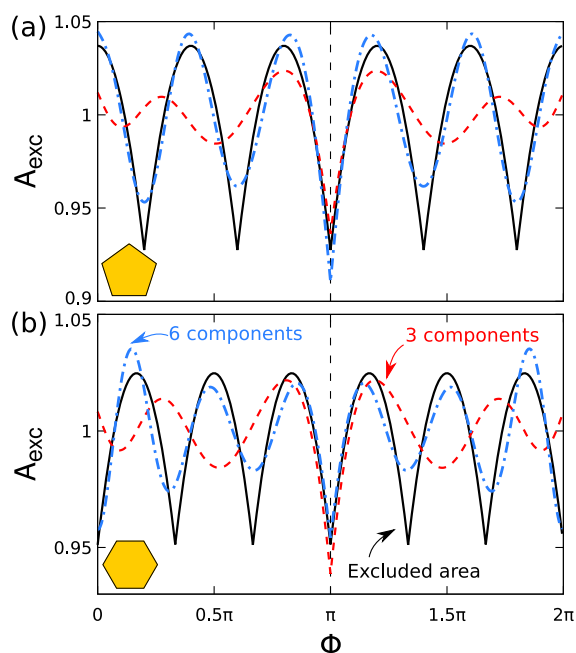


FIG. 9. Excluded area (black solid line) and reconstructed excluded area using three (red dashed line) and six (blue dotted line) principal components as a function of the relative orientation ϕ for the case of regular pentagons (a) and regular hexagons (b).

C. Monte Carlo simulations

We have shown above how PCA is useful to characterize the excluded areas of hard bodies (which play the role of the pair interaction potential in soft systems). The next natural step is a complete analysis of the bulk phase behavior of those particle shapes highlighted by PCA using, e.g., computer simulations or density functional theory. Some of the relevant shapes we have found, like rectangles^{7–9} and triangles,^{12,13} have been extensively studied, while others like the star lines have, to the best of our knowledge, not been

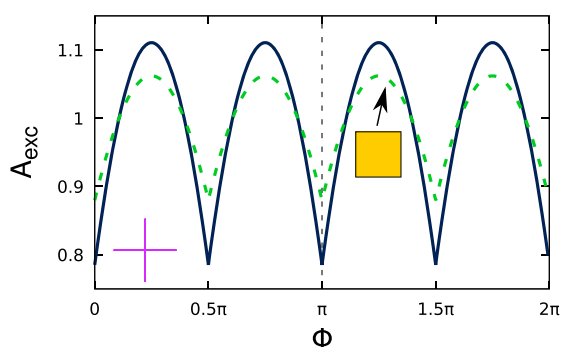


FIG. 10. Excluded area for the fourth limiting case highlighted by PCA, a star line with the shape of a plus (solid black line) and excluded area of a square (dashed green line) as a function of the relative orientation ϕ . The star line particle is shown in the bottom left corner.

analyzed yet. Although such analysis is not the scope of this work, we have also performed short Monte Carlo simulations for selected particle shapes in order to have an initial understanding of how the particle shape affects the bulk behavior.

We performed Monte Carlo (MC) simulations in the NpT (isothermal-isobaric) ensemble. We set a very high value of the pressure such that only steps that decrease the volume are accepted in order to compress the system from the ideal gas limit to very high packing fractions. In each simulation, a system of $N = 200$ particles is compressed at constant pressure. The particles are randomly initialized at sufficiently low density so that the stable state is isotropic. Then $\sim 5 \times 10^7$ Monte Carlo sweeps (MCS) are performed. Here, one MCS is an attempt to individually move and rotate all particles in the system. After every 1.5×10^4 MCS, an attempt to slightly change the volume of the system is performed. To this end, all particle positions are scaled accordingly. The maximum translation and rotation that each particle is allowed to perform in one MCS as well as the maximum volume change in one step are chosen such that the total acceptance probability is approximately 0.25. To detect if two particles overlap, we simply check for the intersection between all pairs of edges.⁶

We present here simulations for (i) particles that resemble an inverted umbrella [result of a deformation of a star line with three segments as indicated in Fig. 8(a)], (ii) arrow particles, and (iii) the polar particles we showed in Fig. 6. The shapes of the selected particles together with their excluded areas are shown in panel (a) of Fig. 11. Representative snapshots of particle configurations at high density are presented in panels (b) and (c). The particles ($i = 1, \dots, N$) are colored according to their $q_2^{(i)}$ (b) and $q_6^{(i)}$ (c) orientational order parameters, defined as

$$q_k^{(i)} = \left| \frac{1}{N_l} \sum_{j=1}^{N_l} e^{-ik\theta_j} \right|, \quad k = \{2, 6\}, \quad (7)$$

where θ_j is the orientation of particle j with respect to a fixed and arbitrary axis, and the sum runs over the N_l particles located at a distance smaller than approximately two particle lengths from particle i (including the i th particle). Note that the order parameter does not change if the relative orientation between the particles θ_{ij} is used in Eq. (7) instead of the absolute orientation of the particle θ_j (provided that the sum includes the i th particle).

The orientational order of the inverted umbrella particles is triatic (three directors forming an angle of $\pi/3$ between them), as indicated by the low q_2 [Fig. 11(b) left] and high q_6 [Fig. 11(c) left] values. By contrast, the orientational order of the arrowlike particles is uniaxial (particles oriented on average along one direction), with high values of both q_2 [Fig. 11(b) middle] and q_6 [Fig. 11(c) middle]. The different behavior between these two particle shapes can be explained with the properties of the excluded area. The excluded areas of both particles have the global minimum at $\phi = \pi$ and two local minima at $\phi = \pi/3$ and $5\pi/3$; see Fig. 11(a). The difference lies in the ratio between the depths of the local minima and the global minimum (measured from the global maximum), which is 0.77 for the inverted umbrella [Fig. 11(a) left] and 0.65 for the arrowlike particle [Fig. 11(a) middle].

The relative stability of phases with triatic and uniaxial orientational order is the result of a competition between orientational and configurational entropies. In a triatic phase, the particles populate

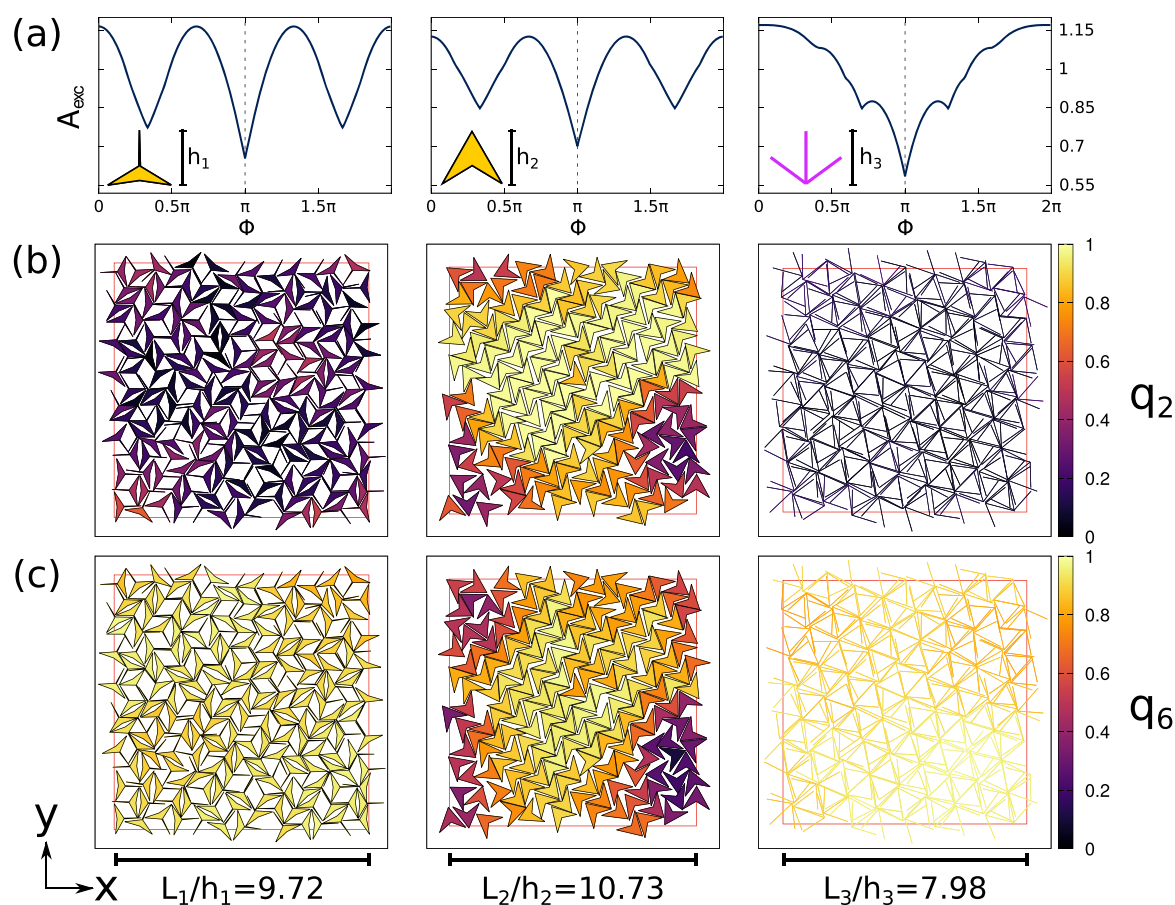


FIG. 11. (a) Excluded areas and geometry of three selected particles. Panels (b) and (c) show selected snapshots of a Monte Carlo simulation of $N = 200$ particles. The color code of the particles indicates the local particle-based order parameters q_2 (b) and q_6 (c). The order parameters of each particle are computed taking into account all particles located in a circular region of diameter two particle lengths centered at the particle of interest.

the three possible minima of the excluded area and hence the orientational entropy is higher than that in the uniaxial phase. However, in a uniaxial phase, only the global minimum of the excluded area is populated (for which the packing is more efficient), which results in higher configurational entropy compared to the triatic phase. The result of this competition depends on the relative depth between the local and the global minima. This parameter can be continuously tuned via deformation of the particle shape.

Note also that there is no minimum at $\phi = 0$ for the excluded area of the arrow particles. Therefore, in the uniaxial phase of the arrow particles, neighboring particles always point in opposite directions. Our simulations suggest a possible coexistence between this ordered state and an isotropic state for the arrow particles. Note that a small region of the simulation box remains isotropic. However, further longer and larger simulations are required to study this in detail.

For the third type of particles [Fig. 11(a) right], the excluded area has a well pronounced minimum at $\phi = \pi$. According to this

observation, one could expect a uniaxial state similar to that found for the arrow particles. The simulations, however, reveal that the particles prefer a state with triatic order. It is then clear that higher than two-body correlations are required to predict the bulk phase behavior for this particle shape. This resembles the case of hard rectangles. There, particles with length-to-width aspect ratio smaller than ~ 7 form small clusters of a few particles each. The cluster formation leads to a global tetratic order^{34–36} with two perpendicular directors in which the symmetry differs from that of the particle shape.

IV. DISCUSSION AND CONCLUSIONS

We have used principal component analysis to investigate the excluded area of two-dimensional hard-bodies. We have restricted the analysis to particle shapes given as non-self-intersecting polygons and star lines. In both cases, the particle shapes were randomly generated. Our analysis shows that the magnitude of the

excluded area as a function of the relative particle orientation is dominated by global features. Hence, despite the vast diversity of particle shapes, the variety of possible excluded areas is more restricted. A clear indication of this is that only three principal components are required to produce a good approximation of the magnitude of the excluded area as a function of the relative particle orientation.

One feature shared by all excluded areas is the position of the global minimum, which in our $\sim 10^6$ randomly generated samples always occurs when the two particles are antiparallel, forming a relative angle $\phi = \pi$. This result, known for convex bodies,³¹ seems to also hold for nonconvex particles.

The dimension reduction via PCA identifies the elongation of the particles as the most prominent feature affecting the excluded area. Furthermore, when represented with the first three principal components, all excluded areas are located on a simply connected three-dimensional region with no holes. At the boundaries, we find four well-defined limiting cases corresponding to shapes of the excluded area with one to four equidistant prominent minima. The relative depth between these prominent minima is a parameter that can be adjusted by varying the particle shape. In contrast to this flexibility, there is not much freedom to vary the relative angle at which the prominent minima of the excluded area occur. However, other features of the excluded area such as the position and number of secondary minima can be tuned. While we do not expect a high impact on the fluid phases, the secondary features might play an important role on the stability of phases with positional order.

We have identified different particle shapes with very similar excluded areas. These particles are ideal candidates to investigate the role of higher than two-body correlations on the bulk phase behavior. Higher than two-body correlations can even dominate the behavior of the system, in which case Onsagerlike theoretical approaches³⁷ that rely entirely on two-body correlations might fail to describe the phenomenology of the system. We have shown an example using MC simulation in which the excluded area possesses a unique global minimum at $\phi = \pi$, but the orientational order of the particles is triatic.

The phase behavior of three particle shapes highlighted in our PCA analysis has been studied: line segments form uniaxial nematic phases,⁶ a fluid of squares¹⁴ or rectangles with short aspect ratio form a tetratic phase,⁷ and triangles form triatic phases.¹² That is, the particle shapes highlighted in the PCA analysis give rise to the formation of mesophases with different orientational properties. PCA is therefore a powerful technique to classify the interaction in hard models and to anticipate the particle shapes of potential interest. PCA can complement other approaches intended to understand self-assembly in colloidal systems such as the inverse design of pair potentials³⁸ and the systematic study of regular shapes using computer simulations.^{39,40} Recently it has been shown how PCA can be applied to detect phase transitions in lattice⁴¹ as well as in continuous⁴² systems.

Promising extensions of the current work are the application of PCA to the excluded area of three-dimensional hard bodies and binary mixtures. Regarding binary mixtures, we expect a much richer variety of shapes. Note, for example, that the excluded area between two different particles does not have to be symmetric with respect to a certain relative orientation (in contrast to the excluded

area between identical particles, which is always symmetric with respect to $\phi = \pi$).

SUPPLEMENTARY MATERIAL

See [supplementary material](#) for a data file with the principal components.

ACKNOWLEDGMENTS

We thank M. Schmidt, E. Velasco, and Y. Martínez-Ratón for feedback and stimulating discussions.

REFERENCES

- ¹B. J. Alder and T. E. Wainwright, *J. Chem. Phys.* **27**, 1208 (1957).
- ²L. Mederos, E. Velasco, and Y. Martínez-Ratón, *J. Phys.: Condens. Matter* **26**, 463101 (2014).
- ³Y. Rosenfeld, M. Schmidt, H. Löwen, and P. Tarazona, *Phys. Rev. E* **55**, 4245 (1997).
- ⁴A. L. Thorneywork, J. L. Abbott, D. G. A. L. Aarts, and R. P. A. Dullens, *Phys. Rev. Lett.* **118**, 158001 (2017).
- ⁵R. Roth, K. Mecke, and M. Oettel, *J. Chem. Phys.* **136**, 081101 (2012).
- ⁶D. Frenkel and R. Eppenga, *Phys. Rev. A* **31**, 1776 (1985).
- ⁷Y. Martínez-Ratón, E. Velasco, and L. Mederos, *J. Chem. Phys.* **122**, 064903 (2005).
- ⁸A. Donev, J. Burton, F. H. Stillinger, and S. Torquato, *Phys. Rev. B* **73**, 054109 (2006).
- ⁹T. Geigenfeind, S. Rosenzweig, M. Schmidt, and D. de las Heras, *J. Chem. Phys.* **142**, 174701 (2015).
- ¹⁰M. A. Bates and D. Frenkel, *J. Chem. Phys.* **112**, 10034 (2000).
- ¹¹J. Dzubiella, M. Schmidt, and H. Löwen, *Phys. Rev. E* **62**, 5081 (2000).
- ¹²A. P. Gantapara, W. Qi, and M. Dijkstra, *Soft Matter* **11**, 8684 (2015).
- ¹³Y. Martínez-Ratón, A. Díaz-De Armas, and E. Velasco, *Phys. Rev. E* **97**, 052703 (2018).
- ¹⁴K. Wojciechowski and D. Frenkel, *Comput. Methods Sci. Technol.* **10**, 235 (2004).
- ¹⁵C. Avendaño and F. A. Escobedo, *Soft Matter* **8**, 4675 (2012).
- ¹⁶T. Schilling, S. Pronk, B. Mulder, and D. Frenkel, *Phys. Rev. E* **71**, 036138 (2005).
- ¹⁷W. van der Stam, A. P. Gantapara, Q. A. Akkerman, G. Soligno, J. D. Meeldijk, R. van Roij, M. Dijkstra, and C. de Mello Donega, *Nano Lett.* **14**, 1032 (2014).
- ¹⁸Z. Hou, K. Zhao, Y. Zong, and T. G. Mason, *Phys. Rev. Mater.* **3**, 015601 (2019).
- ¹⁹J. A. Cuesta and D. Frenkel, *Phys. Rev. A* **42**, 2126 (1990).
- ²⁰S. Varga, P. Gurin, J. C. Armas-Perez, and J. Quintana-H, *J. Chem. Phys.* **131**, 184901 (2009).
- ²¹J. A. Martínez-González, S. Varga, P. Gurin, and J. Quintana-H, *J. Mol. Liq.* **185**, 26 (2013).
- ²²J. A. Martínez-González, S. Varga, P. Gurin, and J. Quintana-H., *Europhys. Lett.* **97**, 26004 (2012).
- ²³E. S. Harper, R. L. Marson, J. A. Anderson, G. Van Anders, and S. C. Glotzer, *Soft Matter* **11**, 7250 (2015).
- ²⁴K. Pearson, *Philos. Mag.* **2**, 559 (1901).
- ²⁵S. Wold, K. Esbensen, and P. Geladi, *Chemom. Intell. Lab. Syst.* **2**, 37 (1987).
- ²⁶G. A. Croes, *Oper. Res.* **6**, 791 (1958).
- ²⁷S. Lin, *Bell Syst. Tech. J.* **44**, 2245 (1965).
- ²⁸I. Jolliffe, *Principal Component Analysis* (Springer Verlag, New York, 2002).
- ²⁹G. Bradski, Dr. Dobb's J. Software Tools **25**, 120–125 (2000).
- ³⁰J. A. Anderson, J. Antonaglia, J. A. Millan, M. Engel, and S. C. Glotzer, *Phys. Rev. X* **7**, 021001 (2017).

- ³¹P. Palfy-Muhoray, E. G. Virga, and X. Zheng, *J. Phys. A: Math. Theor.* **47**, 415205 (2014).
- ³²P. I. C. Teixeira, A. J. Masters, and B. M. Mulder, *Mol. Cryst. Liq. Cryst. Sci. Technol., Sect. A* **323**, 167 (1998).
- ³³J. M. Taylor, *J. Phys. A: Math. Theor.* **52**, 095002 (2019).
- ³⁴Y. Martínez-Ratón and E. Velasco, *Phys. Rev. E* **79**, 011711 (2009).
- ³⁵Y. Martínez-Ratón, E. Velasco, and L. Mederos, *J. Chem. Phys.* **125**, 014501 (2006).
- ³⁶T. Müller, D. de las Heras, I. Rehberg, and K. Huang, *Phys. Rev. E* **91**, 062207 (2015).
- ³⁷L. Onsager, *Ann. N. Y. Acad. Sci.* **51**, 627 (1949).
- ³⁸C. S. Adorf, J. Antonaglia, J. Dshemuchadse, and S. C. Glotzer, *J. Chem. Phys.* **149**, 204102 (2018).
- ³⁹D. Klotsa, E. R. Chen, M. Engel, and S. C. Glotzer, *Soft Matter* **14**, 8692 (2018).
- ⁴⁰D. Wan, C. X. Du, G. van Anders, and S. C. Glotzer, preprint [arXiv:1901.09523](https://arxiv.org/abs/1901.09523) (2019).
- ⁴¹S. J. Wetzel, *Phys. Rev. E* **96**, 022140 (2017).
- ⁴²R. B. Jadrich, B. A. Lindquist, and T. M. Truskett, *J. Chem. Phys.* **149**, 194109 (2018).

The role of sample height in the stacking diagram of colloidal mixtures under gravity

Thomas Geigenfeind and Daniel de las Heras^{1,2}

Theoretische Physik II, Physikalisches Institut, Universität Bayreuth, D-95440 Bayreuth, Germany

E-mail: delasheras.daniel@gmail.com

Received 29 September 2016, revised 4 November 2016

Accepted for publication 16 November 2016

Published 21 December 2016



CrossMark

Abstract

Bulk phase separation is responsible for the occurrence of stacks of different layers in sedimentation of colloidal mixtures. A recently proposed theory (de las Heras and Schmidt 2013 *Soft Matter* **9** 8636) establishes a unique connection between the bulk phase behaviour and sedimentation-diffusion-equilibrium. The theory constructs a stacking diagram of all possible sequences of stacks under gravity in the limit of very high (infinite) sample heights. Here, we study the stacking diagrams of colloidal mixtures at finite sample height, h . We demonstrate that h plays a vital role in sedimentation-diffusion-equilibrium of colloidal mixtures. The region of the stacking diagram occupied by a given sequence of stacks depends on h . Hence, two samples with different heights but identical colloidal concentrations can develop different stacking sequences. In addition, the stacking diagrams for different heights can be qualitatively different since some stacking sequences occur only in a given interval of sample heights. We use the theory to investigate the stacking diagrams of both model bulk systems and mixtures of patchy particles that differ either by the number or by the types of patches.

Keywords: sedimentation, colloidal mixtures, gravity, patchy colloids, stacking diagram

(Some figures may appear in colour only in the online journal)

1. Introduction

Since the pioneer work of Perrin [1], sedimentation has become a central tool for investigating the phase behaviour in colloidal systems. The height-dependent colloidal concentration profile provides a direct measurement of the equation of state for monocomponent systems [2, 3]. Sedimentation experiments are also used to extract information from the bulk phase behaviour in binary colloidal mixtures, see e.g. [4–6]. However, thermal and gravitational energies are of the same order of magnitude for typical colloidal systems. This results in additional gravity-induced phenomenology not present in bulk systems. Examples are denser particles floating on top of

lighter colloids [7], a nematic layer sandwiched by isotropic layers in mixtures of platelets and spheres [8] and mixtures of thin and thick rods [9], and reentrant network formation in mixtures of patchy colloids [10]. It is also common to observe complex stacking sequences in sedimentation with three or more different layers, such as e.g. in mixtures of charged platelets and polymers [11], plate–plate binary systems [12], mixtures of spheres of different sizes [13], and colloidal rod–plate mixtures [14].

The relation between bulk phase behaviour and sedimentation-diffusion-equilibrium in mixtures is therefore intertwined with gravity-induced effects. From a theoretical viewpoint, a generalized Archimedes principle was formulated [7, 15] for the case where one of the components is very diluted. Sedimentation was also studied by analyzing the macroscopic osmotic equilibrium conditions [16, 17]. Recently, de las Heras and Schmidt have proposed a theory [18, 19] for obtaining the stacking diagram, i.e. the set of all possible stacking sequences under gravity, from the bulk

¹ www.danieldelasheras.com

² This article belongs to the special issue: *Emerging Leaders*, which features invited work from the best early-career researchers working within the scope of *Journal of Physics: Condensed Matter*. This project is part of the *Journal of Physics* series' 50th anniversary celebrations in 2017. Daniel de las Heras was selected by the Editorial Board of *Journal of Physics: Condensed Matter* as an Emerging Leader.

phase diagram of a given binary system. The theory is based on the concept of sedimentation paths. Each sedimentation path, which is a line in the plane of chemical potentials representation of the bulk phase diagram, describes the state of the mixture under gravity, in sedimentation-diffusion-equilibrium. Using this theory the stacking diagrams of mixtures of spheres and platelets [18] and mixtures of platelets and non-adsorbing polymers [19] were obtained. Also, very recently, van Roij and coworkers have obtained the stacking diagrams of mixtures of thin and thick colloidal rods [9]. Although in all these cases the bulk phase diagrams of the colloidal systems are relatively simple, the resulting stacking diagrams are extremely rich and show complex stacking sequences. These works are focused on the limit of very high (infinite) sample heights. This idealized limit is very relevant in experimental work since the height of the test tube is typically larger than the gravitational lengths of the colloids.

The interplay between micro confinement and colloidal sedimentation has been experimentally and theoretically investigated [20]. However, little attention has been paid to the influence of the total (macroscopic) sample height in colloidal sedimentation. A remarkable exception is the experimental work of Jamie *et al* [21], in which the properties of the gas-fluid interface of a polymer-colloid mixture are analyzed as a function of the overall height of the container. By systematically changing the total sample height while keeping the polymer-colloid concentrations fixed, the interfacial properties were found to move towards the critical point. Theoretically, it has been shown that varying the sample height might lead to a change in the stacking sequence in mixtures of colloids and nonadsorbing polymers [16, 19].

Here, we use the theory of [18, 19] to study sedimentation-diffusion-equilibrium of colloidal mixtures with finite height samples. We first give a full account of the theory for the case of finite height samples. Next, we systematically investigate the role of sample height in the stacking diagrams of colloidal mixtures. To this end, we apply the theory to model binary systems. That is, systems with generic bulk phase diagrams typical of model Hamiltonian which we however do not explicitly specify. Finally, and as an application of current interest, we study sedimentation in patchy colloidal mixtures. Patchy colloids are functionalized colloids that interact via a directional and valence-limited potential [22, 23]. In our systems the two species of the mixture differ in either the number or in the types of patches. The bulk phase diagrams of these mixtures have been previously analysed [24, 25] using Wertheim's theory [26]. Here, we obtain the stacking diagrams at different heights using only the bulk phase diagrams as input. The stacking diagrams are much richer than the corresponding bulk phase diagrams. Moreover, we show that the sample height is a crucial variable in sedimentation-diffusion-equilibrium of colloidal mixtures. The stacking diagrams for the same mixture but for different sample heights differ not only quantitatively but also qualitatively. For example, some stacking sequences occur only in a given range of sample heights.

2. Theory

2.1. The sedimentation path

Consider a colloidal mixture under gravity in a sedimentation vessel of sample height h . The gravitational potential for each species $i = 1, 2$ is $m_i g z$, where m_i is the buoyant mass of species i , g is the acceleration due to gravity, and z is the vertical coordinate (we set the origin of coordinates, $z = 0$, at the bottom of the sample). Using a local density approximation [8, 18, 19, 27], we define a height-dependent local chemical potential for $0 \leq z \leq h$ for each species

$$\begin{aligned}\mu_1(z) &= \mu_1^b - m_1 g z, \\ \mu_2(z) &= \mu_2^b - m_2 g z,\end{aligned}\quad (1)$$

where μ_i^b is the bulk chemical potential, i.e. the chemical potential in absence of gravity. The local density approximation assumes that for each z the state of the sample is analogous to a bulk system (no gravity) with chemical potentials given by (1). This constitutes a very good approximation provided that the correlation lengths are small compared to the gravitational lengths, $\xi_i = k_B T / m_i g$ with k_B the Boltzmann constant, and T the absolute temperature. Combining the expressions for the local chemical potentials, see (1), and eliminating the height variable z we find

$$\mu_2(\mu_1) = a + s \mu_1, \quad (2)$$

where both a and s are constants given by

$$\begin{aligned}a &= \mu_2^b - s \mu_1^b, \\ s &= m_2 / m_1 = \xi_1 / \xi_2.\end{aligned}\quad (3)$$

The finite size of the sample $0 \leq z \leq h$ is translated into a range for the local chemical potentials

$$0 \leq \frac{\mu_i^b - \mu_i}{m_i g h} \leq 1, \quad i = 1, 2. \quad (4)$$

Equations (2) and (4) represent a line segment, which we refer to as the sedimentation path, in the plane of chemical potentials. The sedimentation path describes how the local chemical potentials vary along the height coordinate in the vessel. Each point in the sedimentation path corresponds to the state of the sample at a given z .

The sedimentation path is directly related to the stacking sequence, i.e. the sequence of stacks of different phases that appear under gravity. If a path crosses a boundary between two phases in the phase diagram, e.g. a binodal, an interface appears in the vessel. The sedimentation path provides a direct link between the bulk phase diagram of the mixture and the stacking sequence. An example of a sedimentation path and its corresponding stacking sequence is shown in figure 1.

A sedimentation path is fully described by its (i) slope, (ii) location in the $\mu_1 - \mu_2$ plane specified by a point on the path, (iii) direction and (iv) length. The slope is fixed by the ratio of the buoyant masses, see (3). The position is determined by the bulk chemical potentials in absence of gravity, and hence by the overall colloidal composition and concentration via a

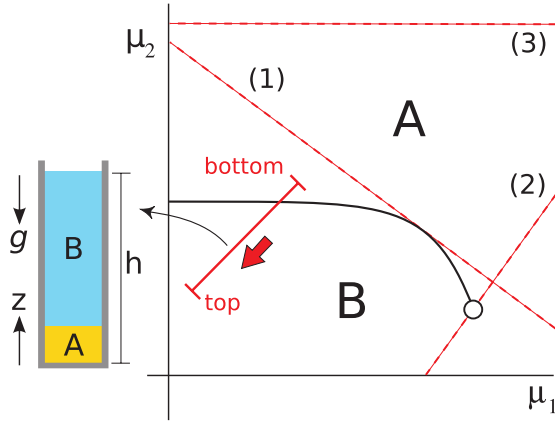


Figure 1. Bulk phase diagram (schematic) of a binary mixture in the plane of chemical potentials $\mu_1 - \mu_2$. Two phases A and B coexist at the binodal (solid black line). The binodal ends at a critical point (empty circle) and has a horizontal asymptote since the pure system of species 2 undergoes a phase transition. The solid red line represents the sedimentation path of the mixture in a vessel of height h under gravity. The arrow indicates the direction of the path from the bottom to the top of the sample. The corresponding stacking sequence is bottom A and top B, as shown in the sketch. The dashed red lines are selected sedimentation paths for infinite height: (1) a path tangent to the binodal, (2) a path that crosses an ending point of a binodal, (3) a path parallel to the asymptotic behaviour of the binodal.

change of variables using the equation of state of the mixture. The direction is given by the signs of the buoyant masses (note m_i can be negative if the mass density of the solvent is higher than the mass density of the colloids). Finally, the length of the path is proportional to the height of the vessel since the difference in chemical potentials between the top ($z = h$) and the bottom of the sample ($z = 0$) is

$$\Delta\mu_i = \mu_i(h) - \mu_i(0) = -m_i gh. \quad (5)$$

2.2. The stacking diagram

We have shown how each sedimentation path is associated to a stacking sequence. The phase stacking diagram is the set of all possible stacking sequences for a given mixture.

Infinite height. For standard colloidal particles in typical sedimentation vessels the length of the sedimentation path is of several $k_B T$ in the $\mu_1 - \mu_2$ plane. That is, the path extends over a big region of the bulk phase diagram of the mixture. Hence, a very relevant idealization is to consider the limit of very high (infinite) sample heights. Within this limit [18, 19] a sedimentation path is a straight line of infinite length (not a line segment) in the plane of chemical potentials. Hence, a sedimentation path can be fully described by using only the slope of the path s , and the crossing point between the path and the μ_2 axis a , see (3). The stacking diagram can then be represented in the $s - a$ plane. There are three types of boundaries between different stacking sequences in the stacking diagram. Here we only describe each one briefly, see [18, 19] for a full account:

- (i) *Sedimentation binodals.* The set of all sedimentation paths tangent to a binodal in the bulk phase diagram is a boundary between two phases in the stacking diagram. The path labeled as (1) in figure 1 is an example. An infinitesimally small change in one or in both variables of the path, a and s , can change the stacking sequence.
- (ii) *Terminal lines.* The set of all paths crossing an ending point of a binodal in the bulk phase diagram is a boundary in the stacking diagram that we call the terminal line. The sedimentation path (2) in figure 1 is an example. An infinitesimal change of a changes the stacking sequence. An ending point can be e.g. a critical point, triple point, critical end point, etc.
- (iii) *Asymptotic terminal lines.* The third type of boundaries in the stacking diagram is formed by those paths that are parallel to the asymptotic behaviour of a binodal. See the path (3) in figure 1. In this case, an infinitesimal change of the slope s alters the stacking sequence. Both the binodal and the path do not terminate at finite chemical potentials. Hence, the sedimentation path and the binodal can cross due to an infinitesimal change of the slope of the path.

A binodal is not the only possible boundary between two regions present in the bulk phase diagram. For example, a percolating line dividing the bulk phase diagram into percolated and nonpercolated states is another type of a boundary between phases. Any boundary present in the bulk phase diagram generates boundaries in the stacking diagram (sedimentation binodals, terminal lines and asymptotic terminal lines). For convenience we speak always of binodal lines but one should bear in mind that other lines also give rise to boundaries in the stacking diagram. The patchy colloid mixtures studied below feature such percolation lines.

Finite height. In this paper we focus on the stacking diagrams for finite height samples. There exist several possibilities to represent the stacking diagram for finite heights. In an experimental work one typically varies the concentration and composition of the mixture, while keeping the solvent and the mass density of the colloids unchanged. The sample height is, in principle, easy to adjust³ and hence forms a useful control parameter. Under these circumstances the slope and the length of the path in the $\mu_1 - \mu_2$ plane are fixed, see (3) and (5), and its position in the $\mu_1 - \mu_2$ plane varies. A sensible choice of variables for the stacking diagram is the plane of average local chemical potentials along the path $\bar{\mu}_1 - \bar{\mu}_2$. As the sedimentation paths are straight lines, the average local chemical potentials are just the local chemical potential evaluated at the middle of the sample $\bar{\mu}_i = \mu_i(z = h/2)$.

The stacking diagram for finite height samples in the $\bar{\mu}_1 - \bar{\mu}_2$ plane contains three possible types of boundaries between different stacking sequences. Two of them are sedimentation binodals originated from coexisting lines in the bulk phase diagrams and one boundary is due to the ending

³ Solvent evaporation might occur, changing the effective sample height and hence the concentration of colloids.

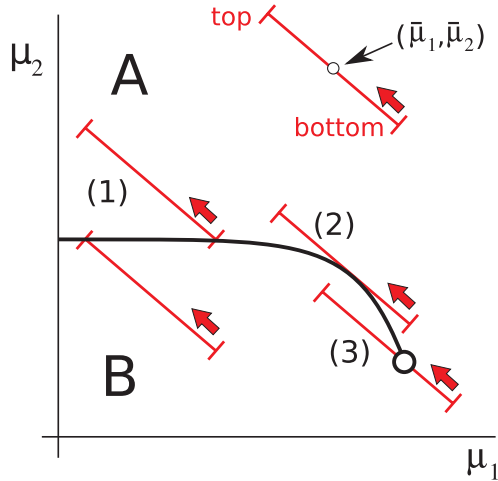


Figure 2. Schematic bulk phase diagram of a binary mixture in the plane of chemical potentials $\mu_1 - \mu_2$. Two phases A and B coexist at the binodal (solid black line). The binodal ends at a critical point (empty circle). The solid red lines are selected sedimentation paths (finite height). The arrow indicates the direction of the path from the bottom to the top of the sample. The coordinates of the middle point of the path are the average local chemical potentials $(\bar{\mu}_1, \bar{\mu}_2)$ as indicated in one of the paths. The top (bottom) path marked with (1) starts (ends) at the binodal. The path labeled as (2) is tangent to the binodal. The path (3) crosses the critical point.

points of the binodals. We describe each of them in detail in the following.

- (i) *Sedimentation binodal type I (SBI)*. The set of all sedimentation paths that either start or end at a binodal form a sedimentation binodal of type I. A path starts (ends) at a binodal if the bottom (top) of the sample is located at the binodal. The path labeled as (1) in figure 2 is an example. For each binodal in the bulk phase diagram there are two corresponding SBI in the stacking diagram. One SBI for those paths that end at the binodal and the other SBI for those paths that start at the binodal. Both SBI lines have the same shape as the bulk binodal. This type of boundary is not present in the case of infinite height because the paths do not have starting and ending points.

Let $\mu_{2,c}(\mu_1)$ be the parameterization of the chemical potential of species 2 at a bulk coexistence line, such as a binodal, as a function of μ_1 . Then, the two corresponding sedimentation binodals of type I are given by

$$\begin{aligned} \bar{\mu}_2(\bar{\mu}_1) &= \mu_{2,c}(\mu_1^-) + m_2g \frac{h}{2}, \\ \bar{\mu}_2(\bar{\mu}_1) &= \mu_{2,c}(\mu_1^+) - m_2g \frac{h}{2}, \end{aligned} \quad (6)$$

where

$$\mu_1^\pm = \bar{\mu}_1 \pm m_1g \frac{h}{2}. \quad (7)$$

Here, μ_1^+ (μ_1^-) is the local chemical potential of species 1 at the bottom (top) of the sample.

- (ii) *Sedimentation binodal type II (SBII)*. The set of all paths tangent to a bulk binodal is also a boundary (sedimentation binodal type II) in the stacking diagram. See the path (2) in figure 2. This boundary is analogous to the sedimentation binodals in the case of infinite height. The SBII boundaries are straight lines in the stacking diagram. A SBII line is present if and only if the slope of the path is the same as the slope of the binodal at some point(s). Each point of a binodal sharing the same slope as the path generates a SBII line.

Let $(\mu_{1,t}, \mu_{2,t})$ be the chemical potentials of a point on a bulk binodal. Let its local slope be that of the sedimentation path. That is

$$\left. \frac{d\mu_{2,c}}{d\mu_1} \right|_{\mu_{1,t}} = s. \quad (8)$$

Then, the associated SBII line is given by

$$\bar{\mu}_2(\bar{\mu}_1) = \mu_{2,t} + (\bar{\mu}_1 - \mu_{1,t})s. \quad (9)$$

The finite size of the path limits the range of $\bar{\mu}_1$ to

$$|\bar{\mu}_1 - \mu_{1,t}| \leq \left| m_1g \frac{h}{2} \right|. \quad (10)$$

- (iii) *Terminal lines (TL)*. The terminal lines are, as in the infinite height case, the set of all paths that cross an ending point of a binodal. See path (3) in figure 2. For each ending point in the bulk phase diagram there is one and only one TL in the stacking diagram. The TL is always a straight line.

Let $(\mu_{1,e}, \mu_{2,e})$ be the chemical potentials of an ending point in bulk, such as a critical point, a triple point, etc. The corresponding terminal line is

$$\bar{\mu}_2(\bar{\mu}_1) = \mu_{2,e} + (\bar{\mu}_1 - \mu_{1,e})s, \quad (11)$$

for

$$|\bar{\mu}_1 - \mu_{1,e}| \leq \left| m_1g \frac{h}{2} \right|. \quad (12)$$

In the three cases (i)–(iii) any infinitesimal displacement of the path changes the stacking sequence (except for the special case in which the displacement is such that the path moves along the boundary of the stacking diagram). The asymptotic terminal lines that occur in the case of infinite sample height do not appear at finite height since the slope of the sedimentation path is fixed and the paths are of finite length.

The three boundaries SBI, SBII, and TL divide the stacking diagram in different regions. Each region corresponds to a different stacking sequence. In order to identify each sequence we first select one point inside of the desired region. Next we plot the corresponding path in the bulk phase diagram such that we can determine the sequence by inspecting the crossings between the path and the binodals.

Once the stacking diagram has been calculated in the $\bar{\mu}_1 - \bar{\mu}_2$ plane, we can easily transform to any other set of variables provided that the equation of state of the mixture is known.

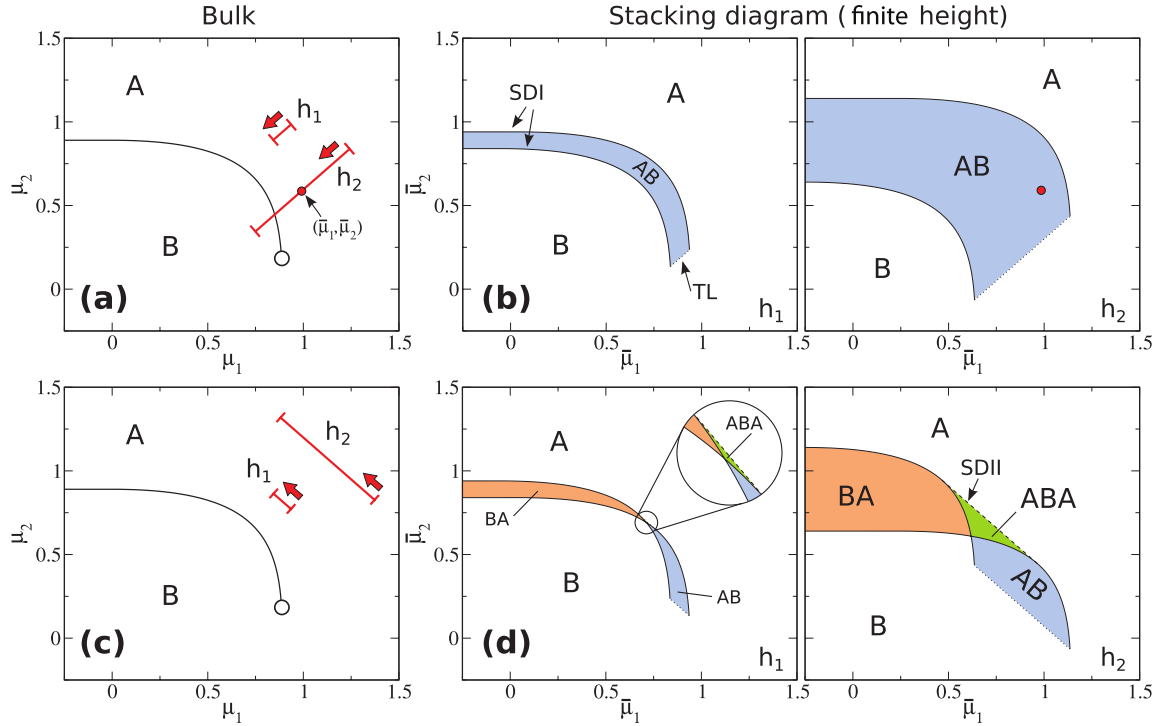


Figure 3. (a) Schematic bulk phase diagram of a binary mixture in the plane of chemical potentials $\mu_1 - \mu_2$. Two phases A and B coexist at the binodal (solid black line). The binodal ends at a critical point (empty circle). The solid red lines are representative sedimentation paths (finite height) corresponding to samples with two different heights, h_1 and $h_2 > h_1$, as indicated. The slope of the path is $s = 1$ in both cases. The arrow indicates the direction of the path from the bottom to the top of the sample. The red circle on the path h_2 is located at the center of the path. Its coordinates are the average local chemical potentials along the path. (b) Stacking diagrams for samples with heights h_1 (left) and h_2 (right). Sedimentation binodals of type I (SBI) are indicated by black solid lines and terminal lines (TL) by black dotted lines. Each region is coloured and labelled according to its stacking sequence (from bottom to top). The sedimentation path corresponding to the point highlighted with a red circle in panel (b) is represented in the bulk phase diagram (a). The lower panels (c) and (d) show the same diagrams for the case of sedimentation paths with slope $s = -1$. The sedimentation binodals of type II are indicated by black dashed lines. The inset on the left of panel (d) is a close view of a region of the stacking diagram.

In order to ease comparison to experimental work, a sensible choice of variables for the stacking diagram is the $\bar{\eta}_1 - \bar{\eta}_2$ plane, where $\bar{\eta}_i$ is the average packing fraction of species i ,

$$\bar{\eta}_i = \frac{1}{h} \int_0^h dz \eta_i(z). \quad (13)$$

Here, $\eta_i(z)$ is the local packing fraction of species i at a distance z from the bottom of the sample. To obtain $\eta_i(z)$ we first compute the local chemical potentials at z using equation (1), and then use the equation of state of the system $\eta_i = \eta_i(\mu_1, \mu_2)$. The phase diagram in the $\bar{\eta}_1 - \bar{\eta}_2$ plane is then obtained by transforming the coordinates of the boundaries in the stacking diagram from $(\bar{\mu}_1, \bar{\mu}_2)$ to $(\bar{\eta}_1, \bar{\eta}_2)$. Other representations of the stacking diagram such as for example average osmotic pressure versus average composition are also possible, following a similar transformation procedure.

3. Results

We first apply our theory to obtain the stacking diagrams at finite height of different bulk model phase diagrams (section 3.1). Although the bulk phase diagrams do not correspond to real microscopic

models, they are representative of the behaviour of typical colloidal mixtures. The model bulk phase diagrams provide relevant examples of possible topologies of the stacking diagrams. In section 3.2 we apply the theory to model binary mixtures of patchy colloids for which we use Wertheim's theory to obtain the bulk phase diagram. Finally, in section 3.3 we compare the stacking diagrams at finite and infinite sample heights.

3.1. Model bulk phase diagrams

One of the simplest possible bulk phase diagrams of a binary mixture is schematically represented in figure 3(a). There is a single binodal at which two phases A and B coexist. The binodal ends at a critical point. The species 2 undergoes an A-B phase transition. Hence, the binodal has a horizontal asymptote and tends to the value of μ_2 at the transition (chosen as $\lim_{\mu_1 \rightarrow -\infty} \mu_2 = 0.89$). This phase diagram might be representative of e.g. a mixture of spherical colloids (species 1) and anisotropic colloids undergoing an isotropic-nematic phase transition (species 2). A small degree of polydispersity in the spherical colloids could prevent a liquid-solid phase transition in the pure system of species 1⁴.

⁴This ignores phase coexistence phenomena in polydisperse systems.

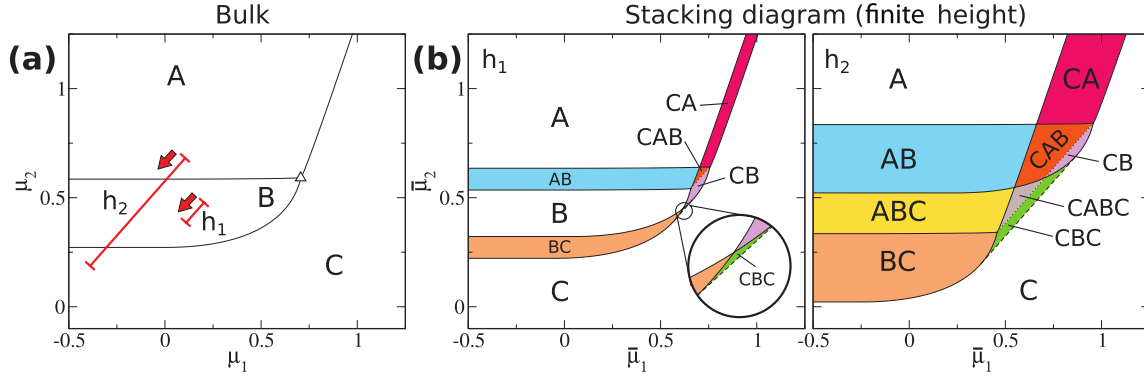


Figure 4. (a) Schematic bulk phase diagram of a binary mixture in the plane of chemical potentials $\mu_1 - \mu_2$. The solid black lines indicate binodals. Three phases A, B and C coexist at a triple point (triangle). The solid red lines are representative sedimentation paths of samples with two different finite heights, h_1 and h_2 , as indicated. The slope of each path is $s = 1$. The arrow indicates the direction of the path from the bottom to the top of the sample. (b) Stacking diagrams for samples with heights h_1 (left) and $h_2 > h_1$ (right). The SBI lines are indicated by black solid lines. The SBII lines are represented as black dashed lines. The TL are indicated by black dotted lines. Each region is coloured and labelled according to its stacking sequence (from bottom to top). The inset on the left of panel (b) is a close view of a region of the stacking diagram.

The stacking diagram of the chosen model bulk phase diagram for the case of infinite height is shown in figure 5 of [19]. Here we focus on the case of finite height. In figure 3(b) we represent the stacking diagram ($\bar{\mu}_1 - \bar{\mu}_2$ plane) for two different heights h_1 and h_2 with $h_2 > h_1$. In both cases the slope of the paths are the same, $s = m_2/m_1 = 1$, and both buoyant masses are positive such that both local chemical potentials decrease from the bottom to the top of the sample. We show representative sedimentation paths in figure 3(a). Each sedimentation path in the $\mu_1 - \mu_2$ plane in the bulk diagram is a point in the $\bar{\mu}_2 - \bar{\mu}_1$ plane of the stacking diagram (the coordinates of the middle point of the path). The stacking diagrams contain two sedimentation binodals of type I (generated by paths starting and ending at the bulk binodal) and one terminal line (paths crossing the critical point). There are three possible stacking sequences, namely A, B, and AB. We label the sequences according to the order of different stacks from bottom to top.

Next, we study the same model bulk phase diagram but for sedimentation paths with a different slope, $s = -1$. See representative paths in figure 3(c). Here $m_1 > 0$ and $m_2 < 0$ such that μ_1 (μ_2) decreases (increases) from the bottom to the top of the sample. The slope of the path is, in this case, compatible with the slope of the binodal in the sense that there is one point at the binodal whose derivative equals the slope of the path, see (8). Hence, the stacking diagram contains a sedimentation binodal of type II which is formed by the set of paths that are tangent to the binodal in bulk. The boundaries of the stacking diagrams (figure 3(d)) are: two SDI lines, one SDII line, and one TL. These boundaries split the stacking diagram into five regions. The possible stacking sequences are A, B, AB, ABA, and BA⁵. The ABA sequence appears when a path crosses the bulk binodal twice [8, 27].

This very simple example already shows the richness of the stacking diagram. It also suggests that the sample height plays

a major role. The size of the area of the stacking diagrams occupied by each stacking sequence depends strongly on the height of the sample. For example, the AB region substantially increases with h , see figure 3(b). Two samples of different height and different stacking sequences might have the same composition and concentration of colloids (we will see examples in the next section). The height of the sample might have an even stronger influence on the stacking diagram, as we will demonstrate in the following.

In figure 4(a) we show a further model bulk phase diagram. There are three different phases: A, B and C. Three binodals for A-B, A-C, and B-C coexistence meet at a triple point. A phase diagram like this might correspond to a mixture in which the species 1 represents spherical colloids and the species 2 consists of e.g. elongated colloidal particles. The elongated particles can undergo isotropic-nematic and nematic-smectic phase transitions.

The stacking diagrams for this mixture are depicted in figure 4(b) for two different heights, h_1 and h_2 , with $h_1 < h_2$. In both cases the slope of the path is $s = 1$ and both buoyant masses are positive. The boundaries in the stacking diagram are: six SDI lines (two for each of the three binodals), one SDII line (the slope of the path matches the slope of the B-C binodal at one point), and one TL line (originating from the triple point). The stacking diagrams for heights h_1 and h_2 differ substantially from each other, see left and right panels of figure 4(b), respectively. We observe two main differences between the diagrams for short and long samples:

First, the sedimentation paths for the small system (h_1) fit in the space between the A-B and B-C binodals of the bulk phase diagram, see an example in figure 4(a). Consequently the stacking sequence B occurs in the stacking diagram, figure 4(b) (left). In contrast, the stacking sequence B does not occur in the large samples (h_2). The B sequence is replaced by an ABC state, figure 4(b) (right). The sedimentation paths in this case are long enough such that they do not fit in the region

⁵ Note that sequences with a single stack, such as A, are actually one phase-systems and not proper sequences made of different stacks.

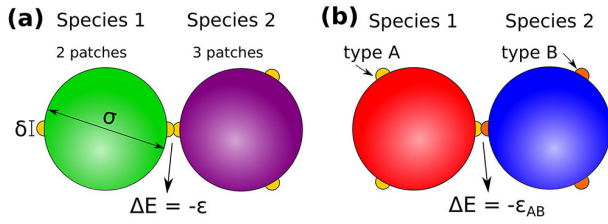


Figure 5. Schematic of the patchy colloidal particles. All colloids are modelled as hard spheres of diameter σ with patches on the surface (spheres of diameter $\delta \approx 0.12\sigma$). We study two types of mixtures. (a) Binary mixtures of particles with identical patches. The species 1 has 2 patches and the species 2 has 3 patches. (b) Binary mixture of particles with three patches of type A (species 1) and of type B (species 2). If two patches overlap the internal energy of the system decreases in a quantity given by the type of patches involved.

between the A-B and B-C binodals in bulk. Instead, the path must cross at least one of the binodals.

Second, the sequence CABC is generated by paths crossing the three binodals in bulk. This sequence is present only in the long samples, figure 4(b) (right). The paths corresponding to the short samples (h_1) are not long enough to cross the three binodals, and hence the CABC sequence is absent.

These examples illustrate how the stacking diagrams for different heights might differ qualitatively. By changing the overall height of the sample some stacking sequences are replaced by others (e.g. the B sequence for h_1 is replaced by ABC for h_2) and one also observes the occurrence of new sequences, such as the CABC sequence for h_2 .

3.2. Mixtures of patchy colloids

We next apply our theory to patchy colloidal binary mixtures. We study two cases in which the species differ either by the number or by the types of patches.

3.2.1. Different number of patches. We model the colloids by hard spheres of diameter σ with identical patches (spheres of size δ) on the surface, see figure 5(a). If two patches overlap the internal energy of the system decreases by ϵ . We use Wertheim's first order perturbation theory [26] and a generalization of the Flory-Stockmayer theory of polymerization [28, 29] to compute the bulk phase diagram of the mixture. We follow exactly the same implementation of the theory as in [24]. Theory and Monte Carlo simulations for the bulk phase behaviour are in semi-quantitative agreement with each other [30, 31].

The species 1 has two patches, and the species 2 has three patches. The colloids with three patches undergo a phase transition between two fluids with different densities. With only two patches present the particles of species 1 can form only chains. The absence of branching prevents phase separation and there is no fluid–fluid phase transition in the pure system of species 1. In the mixture the transition between high and low density fluids ends at a critical point. See the binodal in the bulk phase diagram of the mixture shown in figure 6(a) for scaled temperature $k_B T / \epsilon = 0.09$. In addition

to the binodal, the phase diagram contains a percolation line that divides percolated and non-percolated states. The system is percolated if the probability that a patch is bonded, f_b , is higher than the percolation threshold p_T . The percolation line intersects the binodal close to the critical point on the low density side. The high density phase (G) is an equilibrium gel or network fluid which is always percolated. The low density phase does not percolate (N) except for a very narrow region close to the critical point (G'). We refer the reader to [24, 30] for further details about the bulk phase behaviour of this mixture.

To proceed and to obtain the stacking diagrams we need to set the slope of the sedimentation paths and the height of the sample. We fix the gravitational lengths of the colloids to $\xi_1 = 5$ mm and $\xi_2 = 2$ mm (typical values for colloidal particles). Hence, the slope of the path is fixed to $s = \xi_1 / \xi_2 = 2.5$. The stacking diagrams in the $\bar{\mu}_1 - \bar{\mu}_2$ plane for three different heights $h = 1$ mm, 10 mm, and 25 mm are shown in figure 6(b). Each of them contains four SDI lines (two for the binodal and two for the percolation line) and two terminal lines (one for the critical point and one for the ending point of the percolation line). Six different stacking sequences are possible for this value of the slope: N, G, GN, G-N, G-G', and G-G'N. We use a dash between two stacks in the stacking sequence, like in the G-N sequence, to indicate that the sedimentation path crosses the binodal. The absence of a dash, e.g. in the GN sequence, indicates that the path crosses the percolation line.

Once the stacking diagrams in the plane of average chemical potentials have been computed, we can transform the variables using the procedure described at the end of section 2. In figure 6(c) we show the bulk phase diagram in the plane of packing fractions. The bulk phase diagram can be interpreted as the stacking diagram in the limit of zero sample height for which the sedimentation path is just a point. In figure 6(d) we present the stacking diagrams for $h = 1$ mm and $h = 10$ mm in the plane of average packing fractions.

The number and types of stacking sequences remain the same for the sample heights investigated here. However, the region of the phase space occupied by each sequence significantly depends on the value of the sample height. We show a specific example in figure 7 in which we plot the density profiles of two samples with the same average packing fractions ($\bar{\eta}_1 = 0.002$, and $\bar{\eta}_2 = 0.35$), but different heights ($h = 25$ mm and 10 mm). The corresponding state points are highlighted by green solid circles in the stacking diagrams of figure 6. Despite the average colloidal concentrations being the same, the stacking sequences differ: G-N for the sample with $h = 25$ mm and G for the case $h = 10$ mm. Other values of the sample height and the gravitational lengths will result in identical phenomenology provided that the ratios h/ξ_i with $i = 1, 2$, are unchanged.

3.2.2. Different types of patches. As a concluding example we study a binary mixture of patchy colloids with different types of patches. The species 1 (2) possesses three patches of type A (B), see figure 5(b) for an illustration. When two patches of type α and β with $\alpha, \beta = \{A, B\}$ overlap, the energy

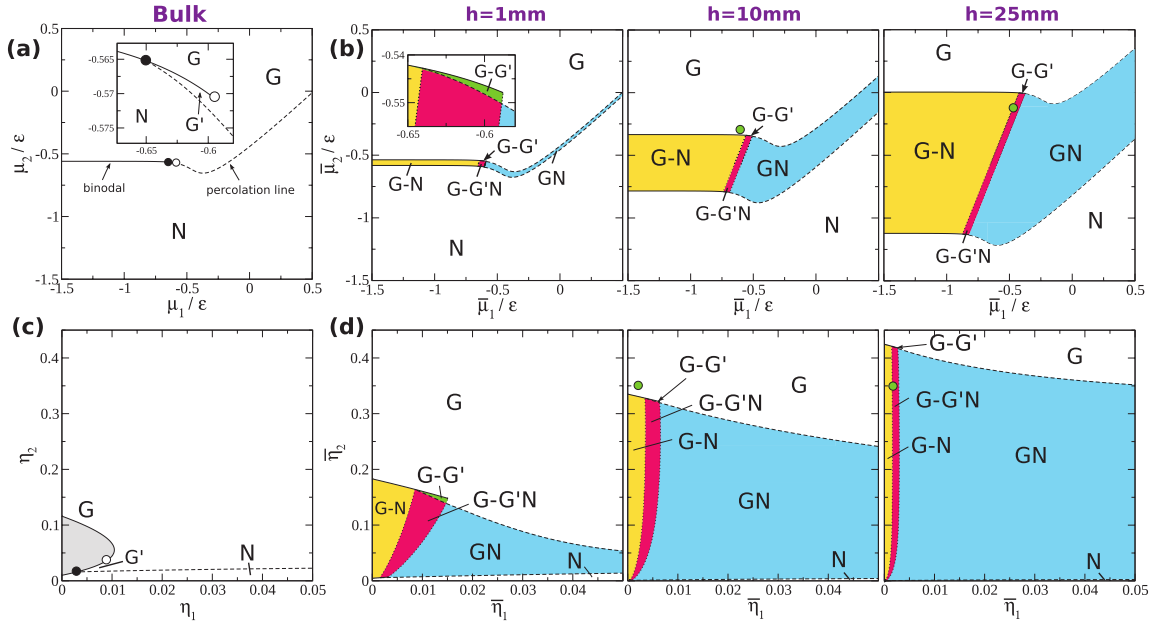


Figure 6. Bulk phase diagram of a binary mixture of patchy colloids with two (species 1) and three (species 2) identical patches in the plane of chemical potentials (a) and packing fractions (c). The temperature is $k_B T/\epsilon = 0.09$. The black solid line indicates the binodal. The dashed line is the percolation line of the mixture. The empty circle indicates the critical point. The black solid circle is the ending point of the percolation line. The inset in (a) is a close view of the region near the critical point. (b) and (d) show the stacking diagrams of the mixture under gravity in the plane of average chemical potentials (b) and average packing fractions (d) for three different sample heights, as indicated. A dash between two letters, like in the sequence G-N, indicates that the sedimentation path crosses the binodal. The absence of a dash, such as e.g. in GN, indicates that the path crosses the percolation line.

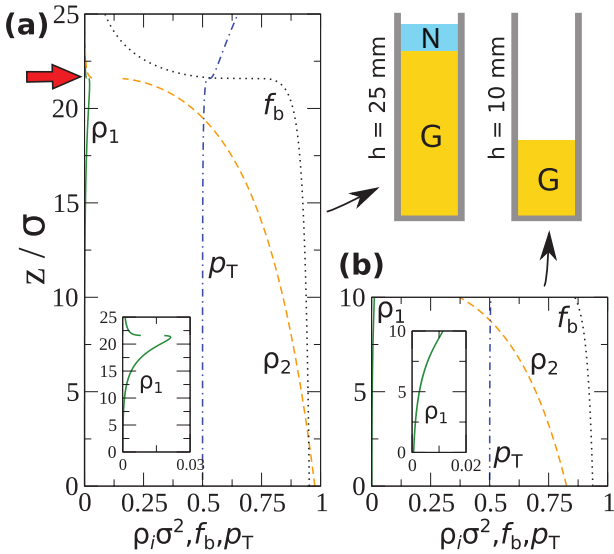


Figure 7. Density profiles ρ_i of species 1 (green solid line) and species 2 (orange dashed line), percolation threshold p_T (dot-dashed blue line), and bonding probability f_b (dotted black line) of a binary mixture of patchy particles with two (species 1) and three (species 2) patches under gravity. The height of the container is $h = 25$ mm (a) and 10 mm (b). The system is percolated if $f_b > p_T$. In both cases the average packing fractions of the colloids of each species are the same, $\bar{\eta}_1 = 0.002$, and $\bar{\eta}_2 = 0.35$. The stacking sequences are G-N (a) and G (b), schematically represented in the upper right corner of the figure. The insets in (a) and (b) are close views of the ρ_1 profile. The red arrow in panel (a) indicates the position of the G-N interface.

of the system decreases by $\epsilon_{\alpha\beta}$. The bulk phase diagram of this model has been studied theoretically [25] and by Monte Carlo simulations [31] for different values of the bonding energies $\epsilon_{\alpha\beta}$. The phenomenology that emerges is very rich as different types of gels can occur depending on the set of bonding energies. Here, we set $\epsilon_{BB} = \epsilon$ (energy scale), $\epsilon_{AA} = 0.80\epsilon$, and $\epsilon_{AB} = 0.85\epsilon$. We fix the scaled temperature, as in the previous case, to $k_B T/\epsilon = 0.09$.

The bulk phase diagrams in the planes of chemical potentials and of packing fractions are shown in figures 6(a) and (b), respectively. At the value of temperature considered only the species 2 (strongest bonds) undergoes a fluid–fluid phase transition. Hence, in the mixture there is only one binodal that ends at a critical point. In addition there are three percolation lines. One of these indicates whether the full mixture percolates, and the other two percolation lines indicate whether the individual species percolate. Although species 1 does not undergo a first order fluid–fluid phase transition at this temperature, it still undergoes a percolation transition. The percolation lines and the binodal divide the bulk phase diagram into five different regions. At low chemical potentials (and hence low densities) the system is non-percolated (N). The other four states are equilibrium percolated gels: (i) a mixed gel (M) in which the mixture percolates but none of the species percolates independently, (ii) a bicontinuous gel or bigel (B) in which the mixture and both species percolate, (iii) two gels (G_i , $i = 1, 2$) in which the mixture and the species i percolate. See [25, 31] for further details about the bulk behaviour.

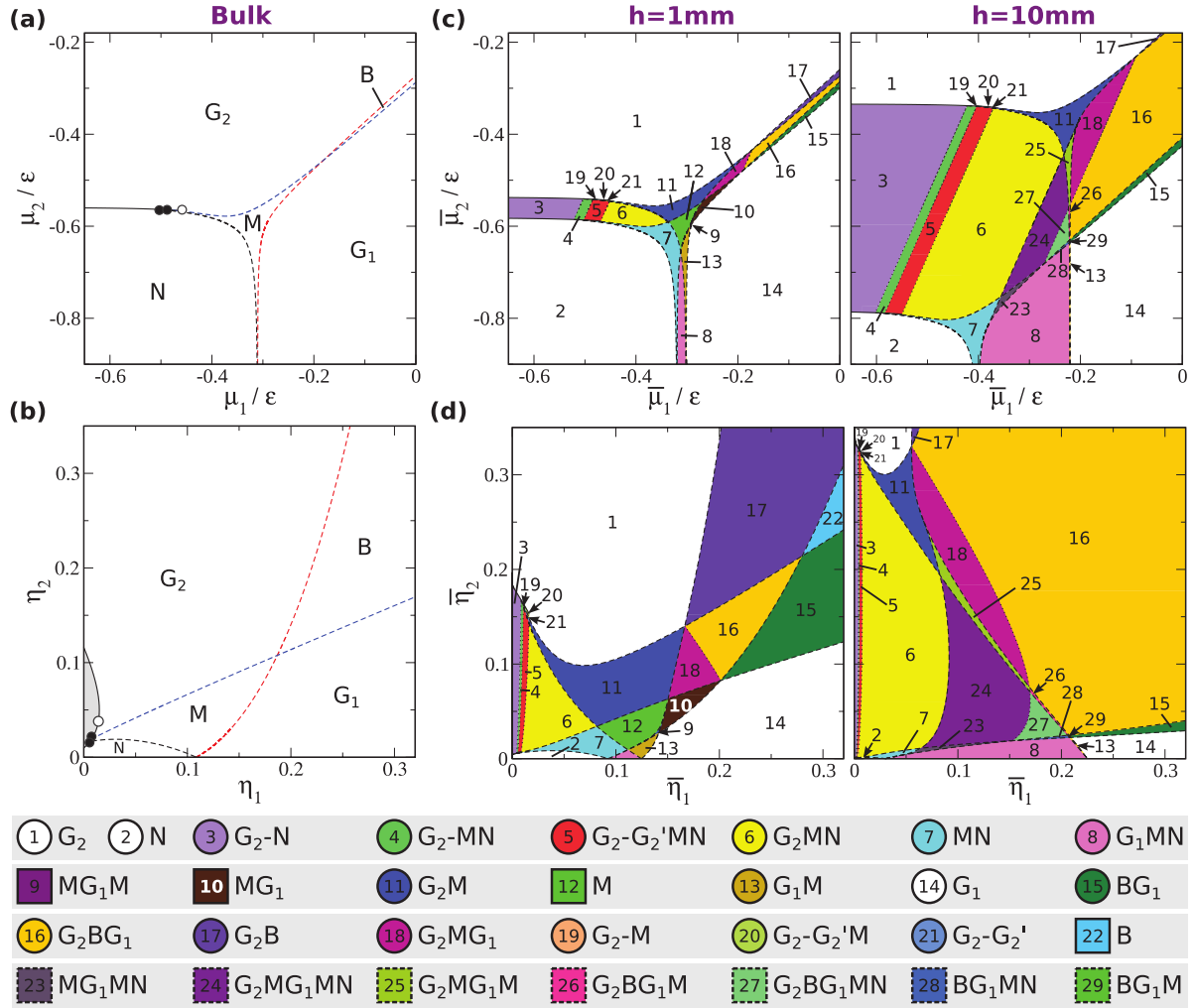


Figure 8. Bulk phase diagram of a binary mixture of patchy colloids with three patches of type A (species 1) and three patches of type B (species 2) in the plane of chemical potentials (a) and packing fractions (b). The black solid line indicates the binodal. The dashed lines are percolation lines of the mixture (black), of the species 1 (red), and of the species 2 (blue). The empty circle indicates the critical point. The black solid circles are the ending points of the percolation lines. Shown are the stacking diagrams of the mixture under gravity in the plane of average chemical potentials (c) and average packing fractions (d) for two different sample heights, as indicated. The legend shows the occurring stacking sequences. A dash between two letters, like in the sequence 3, G₂ – N indicates that the sedimentation path crosses the binodal. The absence of a dash, such as e.g. in 13 (G₁M) indicates that the path crosses a percolation line. The sequences marked with a circle in the legend are present at both sample heights. The sequences marked with a solid (dashed) square occur only for samples with $h = 1$ mm ($h = 10$ mm).

Here, we study sedimentation-diffusion-equilibrium. As in the example above we chose the gravitational lengths to be $\xi_1 = 5$ mm and $\xi_2 = 2$ mm, and study two different sample heights $h = 1$ mm and 10 mm. The resulting stacking diagrams are extremely rich, see figures 8(c) and (d), with more than 20 distinct stacking sequences. Again, the regions occupied for each stacking sequence depend on the sample height. In some cases the same stacking sequence occurs in a completely different range of average packing fractions when varying the sample height, see for example the sequence 11 (G₂M) in figure 8(d). Even more important is the fact that the stacking diagrams for $h = 1$ mm and $h = 10$ mm are *qualitatively* different. There are several stacking sequences that are present only in one of the selected sample heights. For example, the sequence MG₁ (number 10 in figure 8) is only present in

samples with $h = 1$ mm, and the sequence G₂MG₁M (number 25) occurs only for the case $h = 10$ mm.

3.3. Infinite versus finite height stacking diagrams

We conclude the section with several comments regarding the connection between the stacking diagrams for infinite and finite samples. The main effect is the occurrence of new sequences in the case of finite height samples. The new sequences are formed by the removal of one or more stacks of the sequences for $h \rightarrow \infty$. In general, a sequence observed at finite height might be a truncated sequence of the infinite system. This observation has strong implications for the correct interpretation of observed stacking sequences in finite height samples.

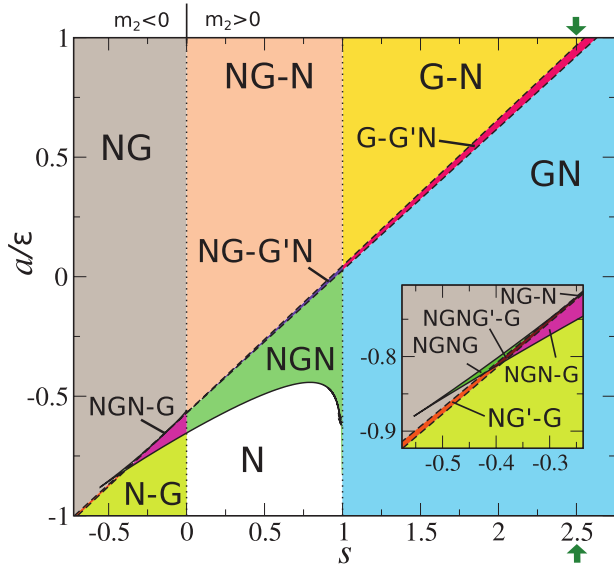


Figure 9. Stacking diagram (infinite height) in the $s - a$ plane of a binary mixture of patchy colloids with two and three patches at $k_B T/\epsilon = 0.09$. The inset is a close view of a small region. Each coloured region is a different stacking sequence labelled from bottom to top of the sample. A dash in the label indicates the sedimentation path crosses the binodal. No dash indicates the path crosses a percolation line. The stacking diagram corresponds to the case $m_1 > 0$. The stacking diagram for the case $m_1 < 0$ can be obtained by just reversing the order of the stacks. The green arrows signal the slope $s = 2.5$ for which we have obtained the stacking diagrams at finite height, see figure 6. Sedimentation binodals are represented by solid lines. Terminal lines are shown as dashed lines. Asymptotic terminal lines are indicated by dotted lines.

In figure 9 we show the stacking diagram (infinite height) of the mixture of patchy colloids with two and three patches analyzed in section 3.2.1. The stacking diagram is represented in the $s - a$ plane, see (3). The diagram has been computed for $m_1 > 0$. Hence positive (negative) values of the slope $s = m_2/m_1$ correspond to positive (negative) values of m_2 . There exists an analogous diagram for $m_1 < 0$ in which the only difference is that the stacking sequences have the reverse order. There are two sedimentation binodals (one for the binodal and one for the percolation line), two terminal lines (critical point of the binodal and ending point of the percolation line), and two asymptotic terminal lines (asymptotic behaviour of the binodal and the percolation lines).

We have shown previously the diagrams at finite height for the slope $s = 2.5$, see figure 6. For this value of s only three sequences are possible at infinite height, see figure 9: GN, G-G'N, and G-N. The finite height diagram is richer with up to six different sequences. These are the same three as for $h \rightarrow \infty$ and three new truncated sequences of the infinite case (G, N, and G-G'). As expected, by increasing the height of the sample, the regions occupied by the new truncated sequences in the stacking diagrams shrink (see figure 6(d)). In this particular example, for $h = 25$ mm, the stacking diagram is already dominated by the stacking sequences of the infinite height case.

The infinite height stacking diagram provides the set of possible sequences for different values of s . Here, we have only analysed the value $s = 2.5$ of the slope for finite height samples. The infinite height stacking diagram shows that for other values of s further complex phenomenology occurs. For example, for negative values of the slope, i.e. $m_2 < 0$, it is possible to stabilize the sequence NGN-G which constitutes a reentrant percolation phenomenon. This sequence also occurs in two-dimensional binary mixtures of patchy colloids [10].

Experimentally one can change the slope of the path via the synthesis of colloids with cores of different materials [32, 33] or changing the mass density of the solvent. Hence, the full range of stacking sequences of a given colloidal mixture is, in principle, experimentally accessible.

4. Discussion and conclusions

Our theory is based on a local density approximation which assumes that for each z the state of the sample can be approximated by a bulk state. Non-local effects might modify the stacking diagrams. In particular, the theory neglects the surface tension of the interfaces between stacks in the stacking sequence. If one of the stacks is very narrow the surface tension of the upper and lower interfaces might be higher than the gain in free energy due to the formation of the stack, as observed in colloid-polymer model mixtures [27]. Under such circumstances, the final equilibrium stacking sequence might be different than that predicted by our local theory. This condition is analogue of capillary condensation/evaporation. Surface effects such as e.g. the occurrence of wetting and layering near the walls of the vessel might also modify the stacking diagrams.

Our theory can be easily extended to multicomponent systems since the sedimentation paths remain lines in the phase space of chemical potentials. Also, the theory is directly applicable to molecular systems. There, the gravitational lengths are orders of magnitude higher than in colloidal systems. Hence, to observe similar phenomenology one needs containers of considerable size, such as for example geological deposits.

We have obtained the stacking diagrams at constant sample height and fixed ratio of the buoyant masses. Other choices, such as for example keeping the colloidal concentrations fixed and varying the sample height, are also possible. A stacking diagram in which one of the variables is the height might be relevant to study the effects of slow solvent evaporation, which is a process that changes the total volume but keeps the particle number fixed.

We have shown that two samples with the same colloidal concentrations but placed in vessels of different heights might have different stacking sequences. We have also shown that the stacking diagrams might be qualitatively different for different heights. Therefore, the sample height plays a major role in sedimentation-diffusion-equilibrium experiments. This role is as important as for example the average colloidal concentrations. We conclude that the sample height should be carefully measured and specified in any sedimentation experiment.

We have focused on sedimentation-diffusion-equilibrium in colloidal mixtures. Future studies could consider the dynamics of sedimentation using dynamic density functional theory [34, 35] and power functional theory [36].

Acknowledgments

We thank Matthias Schmidt for very useful discussions and a careful reading of the manuscript. This work was supported in part by the Portuguese Foundation for Science and Technology (FCT) through project EXCL/FIS-NAN/0083/2012.

References

- [1] Perrin J 1916 *Atoms* (New York: D. Van Nostrand Company)
- [2] Piazza R, Bellini T and Degiorgio V 1993 *Phys. Rev. Lett.* **71** 4267
- [3] Biben T, Hansen J-P and Barrat J-L 1993 *J. Chem. Phys.* **98** 7330
- [4] Piazza R 2014 *Rep. Prog. Phys.* **77** 056602
- [5] Kleshchanok D, Meijer J M, Petukhov A V, Portale G and Lekkerkerker H N W 2012 *Soft Matter* **8** 191
- [6] Chen M, Li H, Chen Y, Mejia A F, Wang X and Cheng Z 2015 *Soft Matter* **11** 5775
- [7] Piazza R, Buzzaccaro S, Secchi E and Parola A 2012 *Soft Matter* **8** 7112
- [8] de las Heras D, Doshi N, Cosgrove T, Phipps J, Gittins D I, van Duijneveldt J S and Schmidt M 2012 *Sci. Rep.* **2** 789
- [9] Drwenski T, Hooijer P and van Roij R 2016 *Soft Matter* **12** 5684
- [10] de las Heras D, Treffenstädt L L and Schmidt M 2016 *Phys. Rev. E* **93** 030601
- [11] Luan L, Li W, Liu S and Sun D 2009 *Langmuir* **25** 6349
- [12] Nakato T, Yamashita Y, Mouri E and Kuroda K 2014 *Soft Matter* **10** 3161
- [13] Chen M, Cölfen H and Polarz S 2015 *ACS Nano* **9** 6944
- [14] Woolston P and van Duijneveldt J S 2015 *Langmuir* **31** 9290
- [15] Piazza R, Buzzaccaro S, Secchi E and Parola A 2013 *Phys. Biol.* **10** 045005
- [16] Wensink H H and Lekkerkerker H N W 2004 *Europhys. Lett.* **66** 125
- [17] Savenko S V and Dijkstra M 2004 *Phys. Rev. E* **70** 051401
- [18] de las Heras D and Schmidt M 2013 *Soft Matter* **9** 8636
- [19] de las Heras D and Schmidt M 2015 *J. Phys.: Condens. Matter* **27** 194115
- [20] Royall C P, Dzubiella J, Schmidt M and van Blaaderen A 2007 *Phys. Rev. Lett.* **98** 188304
- [21] Jamie E A G, Wensink H H and Aarts D G A L 2010 *Soft Matter* **6** 250
- [22] Bianchi E, Blaak R and Likos C N 2011 *Phys. Chem. Chem. Phys.* **13** 6397
- [23] Wang Y, Wang Y, Breed D R, Manoharan V N, Feng L, Hollingsworth A D, Weck M and Pine D J 2012 *Nature* **491** 51
- [24] de las Heras D, Tavares J M and Telo da Gama M M 2011 *Soft Matter* **7** 5615
- [25] de las Heras D, Tavares J M and Telo da Gama M M 2012 *Soft Matter* **8** 1785
- [26] Wertheim M 1986 *J. Stat. Phys.* **42** 459
- [27] Schmidt M, Dijkstra M and Hansen J-P 2004 *Phys. Rev. Lett.* **93** 088303
- [28] Flory P J 1941 *J. Am. Chem. Soc.* **63** 3083
- [29] Stockmayer W H 1943 *J. Chem. Phys.* **11** 45
- [30] Bianchi E, Largo J, Tartaglia P, Zaccarelli E and Sciortino F 2006 *Phys. Rev. Lett.* **97** 168301
- [31] Seiferling F, de las Heras D and Telo da Gama M M 2016 *J. Chem. Phys.* **145** 074903
- [32] Velikov K P and van Blaaderen A 2001 *Langmuir* **17** 4779
- [33] Peng B, van Blaaderen A and Imhof A 2013 *ACS Appl. Mater. Interfaces* **5** 4277
- [34] Evans R 1979 *Adv. Phys.* **28** 143
- [35] Marconi U M B and Tarazona P 1999 *J. Chem. Phys.* **110** 8032
- [36] Schmidt M and Brader J M 2013 *J. Chem. Phys.* **138** 214101

Superadiabatic demixing in nonequilibrium colloids

Thomas Geigenfeind,¹ Daniel de las Heras,^{1,*} and Matthias Schmidt^{1,†}

¹*Theoretische Physik II, Physikalisches Institut, Universität Bayreuth, D-95440 Bayreuth, Germany*

(Dated: May 29, 2019)

We identify a unique demixing force density distribution that arises from repulsive interparticle interactions in driven binary colloidal fluids under overdamped Brownian dynamics. The demixing force density is resolved in space and in time and it counteracts diffusive currents which arise due to gradients of the local mixing entropy. We construct a power functional approximation that describes superadiabatic demixing, and apply the theory to colloidal lane formation in oppositely driven binary quasi-hard core mixtures. We find excellent agreement of the theoretical results with our Brownian dynamics computer simulation results for adiabatic, structural, drag and viscous force contributions. We show that the concept of superadiabatic demixing allows to rationalize the emergence of mixed, laned and jammed states in driven binary mixtures.

I. INTRODUCTION

The concept of mixing entropy in multi-component systems is profound for our understanding and quantitative description of complex systems. In equilibrium, mixing entropy can overcome strong energetic repulsion that arises due to internal interactions between the constituent particles. It is a driving mechanism, if not an antagonist, for a wide range of structuring and self-assembly phenomena. The systems and phenomena where mixing entropy plays a crucial role cover a broad range, from the fundamentals of liquid state theory, such as the determination of the equation of state of binary mixtures of hard spheres [1] to the determination of phase behaviour, such as entropy-driven phase transitions of colloid-polymer mixtures [2], understanding liquid-liquid immiscibility in polymer solutions [3], the demixing transition in athermal mixtures of colloids and flexible self-excluding polymers [4], liquid crystal physics, such as isotropic-nematic-nematic phase-separation for bidisperse rod-like particles [5], or rod-plate mixtures, where biaxiality competes with demixing [6], percolation in binary and ternary mixtures of patchy colloids [7], and selectivity in spatially inhomogeneous binary fluid mixtures [8]. Important technological applications where mixing entropy is relevant include the capacitive mixing for harvesting the free energy of solutions [9], and in 'blue energy' from ion adsorption and electrode charging in sea and river water [10]. Although in nonequilibrium the situation is much less clear, gradients of position-resolved mixing entropy fields were shown to be relevant e.g. for the dynamics of liquid films with soluble surfactant [11].

Here we identify and describe a competing effect that occurs in genuine nonequilibrium and that can counteract diffusive forces generated by the mixing entropy in a similar way that explicit interparticle repulsion does in equilibrium. We show that this effect is “superadia-

batic” in character, i.e. it acts above all effects that can be understood on the basis of an equilibrium (“adiabatic”) reference state and its free energy. As we show, superadiabatic demixing is a genuine nonequilibrium effect and a corresponding unique superadiabatic force density distribution can be identified that acts spatially and temporally resolved in nonequilibrium systems. As both a relevant application and a demonstration of the concept we revisit the well-studied phenomenon of colloidal lane formation in oppositely driven binary mixtures, where for the first time we are able to rationalize quantitatively, on the basis of a physical model of the underlying superadiabatic effect, the emergence of nonequilibrium structure formation in this system.

We show in Fig. 1 characteristic snapshots of a colloidal mixture of two species with repulsive interparticle interactions driven in opposite directions (details about the system are given below). At low driving, Fig. 1a, the diffusive forces generated by the entropy of mixing dominate and the system remains in a homogeneous state with both species flowing through each other. At high driving however the species segregate into two lanes, Fig. 1b. Lane formation constitutes a genuine nonequilibrium self-organization process that has attracted much interest in the literature since it occurs in strikingly different areas, ranging from colloidal systems [12–17], plasmas [18, 19], and lattice models [20], to different kinds of living systems, such as bacteria in channels [21], ant trails [22], and groups of pedestrians [23]. Laning has also been studied when the external driving directions of the two species are non-parallel to each other [24], have high shear rates [25], or other characteristics such as rotating magnetic field in channels, and periodic driving with different friction coefficients [26–28]. Studies were devoted to the influence of noise and of hydrodynamic interactions [29, 30] as well as the characteristics of the transition toward laning in two-dimensional systems [31]. Although the primary focus is on purely repulsive model systems, such as model suspensions of charged colloids, laning has also been shown to appear in systems governed by attractive [32] and by dipolar [33] interparticle interactions.

Physical mechanisms for laning were attributed to rec-

*Electronic address: delasheras.daniel@gmail.com; URL: www.danieldelasheras.com

†Electronic address: Matthias.Schmidt@uni-bayreuth.de

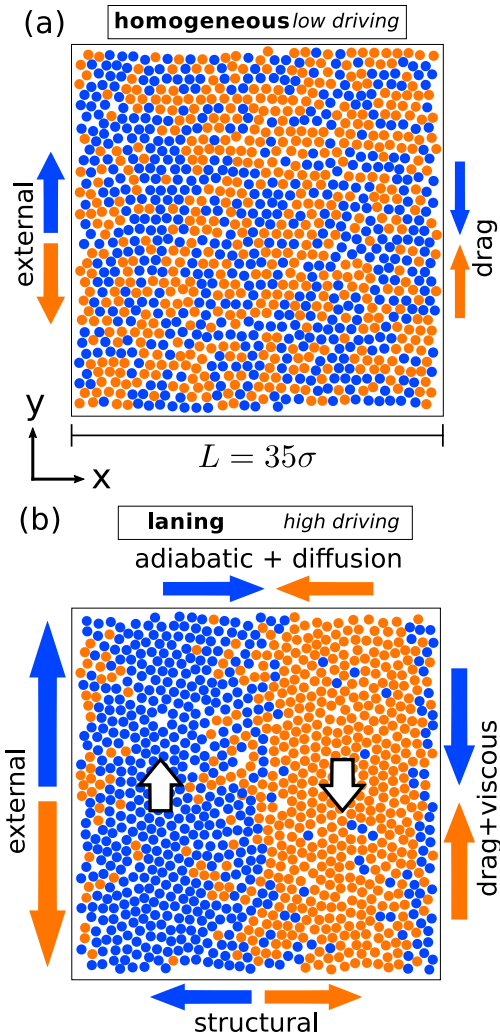


FIG. 1: Characteristic snapshots of a two-dimensional colloidal mixture in a homogeneous (gravitational) external field. Particles of species 1 (orange) possess a positive buoyant mass, i.e. the external force acting on them is directed downwards. Particles of species 2 (blue) have a negative buoyant mass and hence upwards directed external force acting on them. The arrows indicate the direction of the different forces in the system. The color of the arrow shows the species on which the forces act, and its size indicates the relative magnitude of the force as compared to the other forces. At low external driving (a) the system is homogeneous. Forces only act in the flow \hat{y} -direction. At high external driving (b) the system segregates into lanes. The forces acting in the gradient \hat{x} -direction (diffusive, adiabatic, and structural) balance each other. The small white arrows indicate the direction of the velocity inside the lanes.

tification of diffusion on the particle scale [34]. The pair correlation functions were considered to be the key observables to quantify the laning phenomenon [35]. Theoretical treatments have been scarce. Based on phenomenological versions of dynamical density functional

theory Chakrabarti and coauthors [13, 14] obtained a dynamical instability as a steady-state bifurcation of the density field around the onset of structural inhomogeneity in the simulations. Poncet et al [35] used linearized stochastic density functional theory for the pair correlation functions. Kohl et al [36] used a microscopic approach, based on Kirkwoods superposition approximation as a closure relation, to also calculate nonequilibrium pair correlations in strongly interacting driven binary mixtures. Wächtler et al [32] performed a stability analysis based on dynamical density functional theory. Despite this progress, a systematic theoretical framework that would describe laning has not yet been formulated. Here we present a comprehensive theory for driven binary mixtures that operates on the level of one-body correlation functions, such as (partial) density and current distributions. The general framework constitutes a closed theory, based on the power functional concept for mixtures [37, 38]. We present an approximate form of the superadiabatic free power functional, which is a functional generator of the nonequilibrium force distributions. Crucially, we demonstrate that the superadiabatic demixing force fields are kinematic functionals, i.e. depend not only on the density, but also on the flow fields. The theory allows us to quantitatively describe the stability of lane formation.

The paper is organized as follows. In Sec. II we develop a general theory for nonequilibrium mixtures on the level of one-body correlation functions, putting forward a unique splitting of the nonequilibrium one-body force contributions into those acting on the total motion and those acting on the differential motion (i.e. the counterflow of the two species). In Sec. II B we construct a power functional approximation based on generalizing the velocity gradient formalism [39] for mixtures. In Sec. III we describe results of Brownian dynamics computer simulations for the adiabatic and superadiabatic force fields. We consider an “ideal” binary mixture in which all particles share the same interparticle pair interaction potential, independent of the species. The chosen setup allows us to systematically identify the mixture contributions as consisting of drag and of superadiabatic demixing contributions. The total flow is governed by viscous and structural forces. Crucially, we demonstrate that non-gradient contributions involving the relative velocity of the two species generate the superadiabatic demixing effect. We demonstrate the quantitative agreement of theoretical results with simulation data. We conclude in Sec. IV.

II. DYNAMICAL ONE-BODY DESCRIPTION

A. General formulation

Let the positions of N particles in d spatial dimensions be indicated by $\mathbf{r}_1, \dots, \mathbf{r}_N \equiv \mathbf{r}^N$. We consider systems that are composed of different species, labelled by α .

The set \mathcal{N}_α contains all particle indices i that belong to species α . The dynamics of the system are governed by the coupled Langevin equations for overdamped Brownian motion,

$$\gamma \dot{\mathbf{r}}_i = -\nabla_i u(\mathbf{r}^N) + \mathbf{f}_{\text{ext},i}(\mathbf{r}_i, t) + \boldsymbol{\xi}_i(t), \quad (1)$$

where γ is the friction constant against the (implicit) solvent (which we consider to be the same for all particles), the overdot denotes a time derivative, ∇_i indicates the derivative with respect to \mathbf{r}_i , $u(\mathbf{r}^N)$ is the interparticle interaction potential, $\mathbf{f}_{\text{ext},i}(\mathbf{r}, t)$ is an external force field acting on particle i at position \mathbf{r} at time t ; here \mathbf{r} is a generic position coordinate. Furthermore $\boldsymbol{\xi}_i(t)$ is a stochastic white noise force with vanishing mean, $\langle \boldsymbol{\xi}_i(t) \rangle = 0$, and auto-correlation given by

$$\langle \boldsymbol{\xi}_i(t) \boldsymbol{\xi}_j(t') \rangle = 2\gamma k_B T \mathbf{1} \delta_{ij} \delta(t - t'), \quad (2)$$

where the angles denote an average over the realizations of the noise, k_B indicates the Boltzmann constant, T is absolute temperature, $\mathbf{1}$ is the $d \times d$ -unit matrix, and $\delta(\cdot)$ is the Dirac delta distribution. In practice, we discretize the equations of motion (1) with a finite time step Δt , and integrate in time using the Euler algorithm.

We define the one-body density and current distribution functions, respectively, for each species α as

$$\rho_\alpha(\mathbf{r}, t) = \left\langle \sum_{i \in \mathcal{N}_\alpha} \delta(\mathbf{r} - \mathbf{r}_i) \right\rangle, \quad (3)$$

$$\mathbf{J}_\alpha(\mathbf{r}, t) = \left\langle \sum_{i \in \mathcal{N}_\alpha} \delta(\mathbf{r} - \mathbf{r}_i) \mathbf{v}_i \right\rangle, \quad (4)$$

where the angles denote an average both over the noise as before, but also over the set of initial states; the velocity of particle i is given by a symmetric time derivative, $\mathbf{v}_i(t) = (\mathbf{r}_i(t + \Delta t) - \mathbf{r}_i(t - \Delta t)) / (2\Delta t)$ [40]. We obtain the microscopically resolved velocity profile of species α as the ratio

$$\mathbf{v}_\alpha(\mathbf{r}, t) = \frac{\mathbf{J}_\alpha(\mathbf{r}, t)}{\rho_\alpha(\mathbf{r}, t)}. \quad (5)$$

The continuity equation holds individually for each species,

$$\frac{\partial \rho_\alpha}{\partial t} = -\nabla \cdot \mathbf{J}_\alpha, \quad (6)$$

where ∇ indicates the derivative with respect to \mathbf{r} .

The one-body equation of motion translates the sum of all forces that act into local motion. The dynamics on the one-body level are specified by the (exact) force density balance relationship

$$\gamma \mathbf{J}_\alpha = -k_B T \nabla \rho_\alpha + \mathbf{F}_{\text{int}}^\alpha + \rho_\alpha \mathbf{f}_{\text{ext}}^\alpha, \quad (7)$$

where the three terms on the right hand side constitute the force densities due to thermal diffusion, internal interactions, and external influence. Due to the overdamped

character of the dynamics the sum of these forces directly induces a current, cf. the left hand side of (7). Here the internal force density field arises from the internal interaction potential $u(\mathbf{r}^N)$ and is defined via the average

$$\mathbf{F}_{\text{int}}^\alpha(\mathbf{r}, t) = -\left\langle \sum_{i \in \mathcal{N}_\alpha} \delta(\mathbf{r} - \mathbf{r}_i) \nabla_i u(\mathbf{r}^N) \right\rangle. \quad (8)$$

Furthermore the external force field $\mathbf{f}_{\text{ext}}^\alpha(\mathbf{r}, t)$ in (7) acts on particles of species α , hence the external force acting on particle $i \in \mathcal{N}_\alpha$, as appearing in the Langevin equation (1), is given by $\mathbf{f}_{\text{ext},i}(\mathbf{r}_i, t) = \mathbf{f}_{\text{ext}}^\alpha(\mathbf{r}_i, t)$.

The internal one-body force density distributions can be split into adiabatic and superadiabatic one-body contributions [37, 38, 41], according to

$$\mathbf{F}_{\text{int}}^\alpha = \mathbf{F}_{\text{ad}}^\alpha + \mathbf{F}_{\text{sup}}^\alpha. \quad (9)$$

Here the adiabatic force density distribution $\mathbf{F}_{\text{ad}}^\alpha(\mathbf{r}, t)$ is defined as the internal force density that occurs in a corresponding ‘‘adiabatic’’ equilibrium system that is defined by having the same partial density distributions as the nonequilibrium system, $\rho_\alpha^{\text{ad}}(\mathbf{r}) = \rho_\alpha(\mathbf{r}, t)$, $\forall \alpha$. The adiabatic force density is also defined by (8), but with the crucial alteration that the average is now taken over an equilibrium probability distribution (i.e. that of the adiabatic system). Here external ‘‘adiabatic’’ one-body potentials $V_{\text{ad}}^\alpha(\mathbf{r})$ act on species α in order to stabilize the given partial density distributions, via (conservative) force fields $-\nabla V_{\text{ad}}^\alpha(\mathbf{r})$.

The superadiabatic force density distribution $\mathbf{F}_{\text{sup}}^\alpha(\mathbf{r}, t)$ in (9) contains therefore all nonequilibrium effects which arise due to the presence of the flow in the system.

Dividing (7) by the partial densities ρ_α and using (9) we obtain the species resolved force balance equations:

$$\gamma \mathbf{v}_\alpha = -k_B T \nabla \ln \rho_\alpha + \mathbf{f}_{\text{ad}}^\alpha + \mathbf{f}_{\text{sup}}^\alpha + \mathbf{f}_{\text{ext}}^\alpha. \quad (10)$$

The total density profile $\rho(\mathbf{r}, t)$ and the total current distribution $\mathbf{J}(\mathbf{r}, t)$ can be obtained, respectively, by summation of (3) and (4) over all species, i.e.,

$$\rho(\mathbf{r}, t) = \sum_\alpha \rho_\alpha(\mathbf{r}, t), \quad (11)$$

$$\mathbf{J}(\mathbf{r}, t) = \sum_\alpha \mathbf{J}_\alpha(\mathbf{r}, t). \quad (12)$$

In analogy to the partial velocities (5) the mean total velocity is then obtained as

$$\mathbf{v}(\mathbf{r}, t) = \frac{\mathbf{J}(\mathbf{r}, t)}{\rho(\mathbf{r}, t)}. \quad (13)$$

Summing the species-resolved continuity equation (6) over all species and using (11) and (12) yields the total continuity relation as

$$\frac{\partial \rho}{\partial t} = -\nabla \cdot \mathbf{J}. \quad (14)$$

Analogously, summing the species-resolved force density balance (7) over all species yields the total force density balance,

$$\gamma \mathbf{J} = -k_B T \nabla \rho + \mathbf{F}_{\text{int}} + \mathbf{F}_{\text{ext}}, \quad (15)$$

where the total internal force density field is $\mathbf{F}_{\text{int}} = \sum_{\alpha} \mathbf{F}_{\text{int}}^{\alpha}$, with the force density $\mathbf{F}_{\text{int}}^{\alpha}$ acting on species α defined via (8) and the total external force density given by $\mathbf{F}_{\text{ext}} = \sum_{\alpha} \rho_{\alpha} \mathbf{f}_{\text{ext}}^{\alpha}$.

We next divide (15) by the total density profile $\rho(\mathbf{r}, t)$ and use the definition (13) of the total velocity profile in order to obtain

$$\gamma \mathbf{v} = -k_B T \nabla \ln \rho + \mathbf{f}_{\text{int}} + \mathbf{f}_{\text{ext}}, \quad (16)$$

where we have defined the total internal and external force fields, $\mathbf{f}_{\text{int}}(\mathbf{r}, t)$ and $\mathbf{f}_{\text{ext}}(\mathbf{r}, t)$, respectively, as

$$\mathbf{f}_{\text{int}} = \frac{\mathbf{F}_{\text{int}}}{\rho}, \quad (17)$$

$$\mathbf{f}_{\text{ext}} = \sum_{\alpha} \frac{\rho_{\alpha}}{\rho} \mathbf{f}_{\text{ext}}^{\alpha}. \quad (18)$$

As we demonstrate below $\mathbf{f}_{\text{int}}(\mathbf{r}, t)$ is one crucial one-body field that enables one to rationalize the nonequilibrium behaviour of driven mixtures.

We restrict ourselves in the following to binary mixtures such that the species are labelled by $\alpha = 1, 2$. We view the total force field \mathbf{f}_{int} to act on both species in the same way, and also introduce a *differential force density* $\mathbf{G}_{\text{int}}(\mathbf{r}, t)$ which drives the two species through and against each other. Hence using \mathbf{f}_{int} and \mathbf{G}_{int} we express the underlying species-resolved internal force density fields as

$$\mathbf{F}_{\text{int}}^1 = \rho_1 \mathbf{f}_{\text{int}} + \mathbf{G}_{\text{int}}, \quad (19)$$

$$\mathbf{F}_{\text{int}}^2 = \rho_2 \mathbf{f}_{\text{int}} - \mathbf{G}_{\text{int}}. \quad (20)$$

We can invert this relationship and use (17) to obtain

$$\mathbf{G}_{\text{int}} = \frac{\rho_2}{\rho} \mathbf{F}_{\text{int}}^1 - \frac{\rho_1}{\rho} \mathbf{F}_{\text{int}}^2. \quad (21)$$

Hence (17) and (21) express a variable transformation from the species-resolved force densities $\mathbf{F}_{\text{int}}^1(\mathbf{r}, t)$ and $\mathbf{F}_{\text{int}}^2(\mathbf{r}, t)$ to the total force field $\mathbf{f}_{\text{int}}(\mathbf{r}, t)$ and the differential force density $\mathbf{G}_{\text{int}}(\mathbf{r}, t)$. As we demonstrate below, each of the new one-body fields describes unique physical effects. Briefly, \mathbf{f}_{int} contains effects that are also present in a one-component system, while \mathbf{G}_{int} contains the genuine mixture contributions, such as drag and superdemixing, both absent in pure systems.

The dynamics of the total density field are still governed by (16). To describe the mixture contributions, we introduce the density difference ρ_{Δ} and the current difference \mathbf{J}_{Δ} , respectively, via

$$\rho_{\Delta} = \rho_2 - \rho_1, \quad (22)$$

$$\mathbf{J}_{\Delta} = \mathbf{J}_2 - \mathbf{J}_1, \quad (23)$$

where the continuity equation $\partial \rho_{\Delta} / \partial t = -\nabla \cdot \mathbf{J}_{\Delta}$ is readily obtained from the species-resolved continuity equation (6). We define the differential external force density as

$$\mathbf{F}_{\text{ext}}^{\Delta} = \mathbf{F}_{\text{ext}}^2 - \mathbf{F}_{\text{ext}}^1 \equiv \rho_2 \mathbf{f}_{\text{ext}}^2 - \rho_1 \mathbf{f}_{\text{ext}}^1. \quad (24)$$

The corresponding equation of motion is obtained by building the difference of the species-resolved one-body force density balance (7) for $\alpha = 1$ and 2, which yields

$$\gamma \mathbf{J}_{\Delta} = -k_B T \nabla \rho_{\Delta} + \mathbf{f}_{\text{int}} \rho_{\Delta} + 2\mathbf{G}_{\text{int}} + \mathbf{F}_{\text{ext}}^{\Delta}, \quad (25)$$

where as before $\mathbf{f}_{\text{int}}(\mathbf{r}, t)$ is given by (17) and $\mathbf{G}_{\text{int}}(\mathbf{r}, t)$ is given by (21). The structure of (25) is crucial for the dynamics of driven mixtures. The differential current (left hand side) emerges from four different types of force density (right hand side): the first term is the ideal diffusive force density field due to gradients in the density difference. The second term generates a transport effect on ρ_{Δ} which is induced by the presence of \mathbf{f}_{int} . The third term is a genuine mixture contribution that acts directly on the density difference; recall the definition (21) of \mathbf{G}_{int} . The fourth term is due to the external influence, cf. (24).

We next split the fields into adiabatic contributions (i.e. those that can be understood on the basis of a corresponding equilibrium system with the same partial density profiles) and superadiabatic contributions of genuine nonequilibrium character, according to

$$\mathbf{f}_{\text{int}} = \mathbf{f}_{\text{ad}} + \mathbf{f}_{\text{sup}}, \quad (26)$$

$$\mathbf{G}_{\text{int}} = \mathbf{G}_{\text{ad}} + \mathbf{G}_{\text{sup}}. \quad (27)$$

Due to linearity, the same variable transformation as before, (17) and (21), relates the terms on the right hand side with the species-resolved force densities (9). Hence for the adiabatic contributions:

$$\mathbf{f}_{\text{ad}} = \mathbf{F}_{\text{ad}} / \rho, \quad (28)$$

$$\mathbf{G}_{\text{ad}} = \frac{\rho_2}{\rho} \mathbf{F}_{\text{ad}}^1 - \frac{\rho_1}{\rho} \mathbf{F}_{\text{ad}}^2, \quad (29)$$

where the total adiabatic force density is defined as $\mathbf{F}_{\text{ad}} = \sum_{\alpha} \mathbf{F}_{\text{ad}}^{\alpha}$. For the superadiabatic contributions:

$$\mathbf{f}_{\text{sup}} = \mathbf{F}_{\text{sup}} / \rho, \quad (30)$$

$$\mathbf{G}_{\text{sup}} = \frac{\rho_2}{\rho} \mathbf{F}_{\text{sup}}^1 - \frac{\rho_1}{\rho} \mathbf{F}_{\text{sup}}^2, \quad (31)$$

where the total superadiabatic force density is defined as $\mathbf{F}_{\text{sup}} = \sum_{\alpha} \mathbf{F}_{\text{sup}}^{\alpha}$.

We summarize by inserting the adiabatic-superadiabatic splitting (26) and (27) into the velocity equation of motion (16) and into the differential current (25), which yields

$$\gamma \mathbf{v} = -k_B T \nabla \ln \rho + \mathbf{f}_{\text{ad}} + \mathbf{f}_{\text{sup}} + \mathbf{f}_{\text{ext}}, \quad (32)$$

$$\begin{aligned} \gamma \mathbf{J}_{\Delta} = & -k_B T \nabla \rho_{\Delta} + \rho_{\Delta} \mathbf{f}_{\text{ad}} + \rho_{\Delta} \mathbf{f}_{\text{sup}} \\ & + 2\mathbf{G}_{\text{ad}} + 2\mathbf{G}_{\text{sup}} + \mathbf{F}_{\text{ext}}^{\Delta}. \end{aligned} \quad (33)$$

Equations (32) and (33) form the basis of our subsequent classification of the different types of occurring physical effects.

Ideal mixture. In order to highlight the fundamental nonequilibrium effects, we particularize to an “ideal” mixture, in which the internal interactions do not depend on the type of particle. Formally, this implies that the value of the internal interaction potential $u(\mathbf{r}^N)$ is unchanged under permutation of the positions. For pair potentials (as we consider below) the inter-species pair potentials $\phi_{\alpha\alpha}(r)$ are identical to each other and are identical to the cross interaction potential $\phi_{\alpha\alpha'}(r)$ between particles of different species α and α' . Hence, $\phi_{\alpha\alpha'}(r) = \phi(r)$, where $\phi(r)$ is a universal function. Given that all the internal interactions are the same, the adiabatic force field only has a nontrivial component that acts $\mathbf{f}_{\text{ad}}^\alpha = \mathbf{f}_{\text{ad}}$. No differential component occurs in the adiabatic system, hence $\mathbf{G}_{\text{ad}} = 0$, which simplifies the dynamics, cf. (33). Importantly, this symmetry does not apply to the external force field. Hence, in general $\mathbf{f}_{\text{ext}}^\alpha(\mathbf{r}, t) \neq \mathbf{f}_{\text{ext}}^{\alpha'}(\mathbf{r}, t)$ for $\alpha \neq \alpha'$, which imprints differences into the kinematic one-body fields ρ_α and \mathbf{J}_α during the time evolution. Such driving is far from trivial. One might picture differently coloured particles being driven through each other.

Next, we consider a special simplifying situation consisting of steady states characterized by a single direction of the flow along which all vector fields point, i.e. $\mathbf{v}, \mathbf{v}_1, \mathbf{v}_2, \mathbf{J}, \mathbf{J}_1, \mathbf{J}_2$ are all colinear. In the simulation results shown below this is the $\hat{\mathbf{y}}$ -direction (the flow is in the “vertical” direction). All gradients in the system also share a common direction, which is orthogonal to the flow. In the simulations, this is the $\hat{\mathbf{x}}$ -direction (the system is “horizontally” inhomogeneous). Such “perpendicular flow” geometry forms a class of common nonequilibrium situation encompassing e.g. simple shear flow, steady flow between parallel plates etc.

We split the superadiabatic forces into viscous (subscript “visc”), drag, and structural (subscript “struc”) contributions according to

$$\mathbf{f}_{\text{sup}} = \mathbf{f}_{\text{visc}} + \mathbf{f}_{\text{struc}}, \quad (34)$$

$$\mathbf{G}_{\text{sup}} = \mathbf{G}_{\text{drag}} + \mathbf{G}_{\text{struc}}, \quad (35)$$

where, as we show, \mathbf{f}_{visc} is a viscous force field that arises from total shear motion, $\mathbf{f}_{\text{struc}}$ is a structural force field that sustains gradients of the total density distribution, \mathbf{G}_{drag} is a superadiabatic force density distribution that describes the friction effect that occurs due to counterflow (i.e. when $\mathbf{v}_\Delta \neq 0$), and $\mathbf{G}_{\text{struc}}$ is the superadiabatic demixing force density. We demonstrate the validity of this interpretation below. On a formal level, the splitting (34) and (35) is uniquely defined by \mathbf{f}_{visc} and \mathbf{G}_{drag} acting colinear with the flow, and $\mathbf{f}_{\text{struc}}$ and $\mathbf{G}_{\text{struc}}$ acting perpendicular to it.

We can now separate the equations of motion according to the direction of the forces. In the flow direction, using (34) and (35), we obtain from (32) and (33), re-

spectively,

$$\gamma \mathbf{v} = \mathbf{f}_{\text{visc}} + \mathbf{f}_{\text{ext}}, \quad (36)$$

$$\gamma \mathbf{J}_\Delta = \rho_\Delta \mathbf{f}_{\text{visc}} + 2\mathbf{G}_{\text{drag}} + \mathbf{F}_{\text{ext}}^\Delta, \quad (37)$$

which indicates that the total (scaled) flow ($\gamma \mathbf{v}$) arises from a competition of the external driving (\mathbf{f}_{ext}) and the viscous forces (\mathbf{f}_{visc}). The differential current ($\gamma \mathbf{J}_\Delta$) is counteracted by a transport effect that the viscous forces exert on the density difference ($\rho_\Delta \mathbf{f}_{\text{visc}}$), and the drag that any counterflow of the two species induces ($2\mathbf{G}_{\text{drag}}$), and it is driven by the external differential force density ($\mathbf{F}_{\text{ext}}^\Delta$).

In the gradient direction, we also use (32) and (33), respectively, to obtain

$$0 = -k_B T \nabla \ln \rho + \mathbf{f}_{\text{ad}} + \mathbf{f}_{\text{struc}} \quad (38)$$

$$0 = -k_B T \nabla \rho_\Delta + \rho_\Delta (\mathbf{f}_{\text{ad}} + \mathbf{f}_{\text{struc}}) + 2\mathbf{G}_{\text{struc}}. \quad (39)$$

Here, remarkably, the external forces do not appear explicitly. Equation (38) constitutes a force balance relationship, where the sum of the diffusive force, the adiabatic force, and the structural force cancel, such that no motion occurs. Equation (39) is crucial for understanding the physics of driven mixtures: The sum of the diffusive force density difference, $-k_B T \nabla \rho_\Delta$, and the effect of total adiabatic and structural force fields on the density difference, $\rho_\Delta (\mathbf{f}_{\text{ad}} + \mathbf{f}_{\text{struc}})$, is balanced by the structural differential force density, $2\mathbf{G}_{\text{struc}}$. This implies that $\mathbf{G}_{\text{struc}} \neq 0$ can induce a density contrast $\rho_\Delta \neq 0$ in the system.

We can now revert to the species-labelled description and start from the general relationship

$$\mathbf{v}_\alpha = \frac{\rho \mathbf{v} \pm \mathbf{J}_\Delta}{\rho \pm \rho_\Delta}, \quad (40)$$

where the upper sign (+) applies to species 1, and the lower sign (−) applies to species 2. Application to the perpendicular geometry results in the following balance relations in the flow direction and in the gradient direction

$$\gamma \mathbf{v}_\alpha = \mathbf{f}_{\text{visc}} \pm \frac{\mathbf{G}_{\text{drag}}}{\rho_\alpha} + \mathbf{f}_{\text{ext}}^\alpha \quad (\text{flow}), \quad (41)$$

$$0 = \mathbf{f}_{\text{ad}} + \mathbf{f}_{\text{struc}} \pm \frac{\mathbf{G}_{\text{struc}}}{\rho_\alpha} - k_B T \nabla \ln \rho_\alpha \quad (\text{grad}), \quad (42)$$

where again \pm corresponds to $\alpha = 1, 2$. As we have four equations for the four unknown superadiabatic fields, we can solve for these, with the results:

$$\mathbf{f}_{\text{visc}} = \gamma \mathbf{v} - \mathbf{f}_{\text{ext}}, \quad (43)$$

$$\mathbf{G}_{\text{drag}} = \frac{\gamma}{2} (\mathbf{J}_\Delta - \rho_\Delta \mathbf{v} + \rho_\Delta \mathbf{f}_{\text{ext}} - \mathbf{F}_{\text{ext}}^\Delta) \quad (44)$$

$$\mathbf{f}_{\text{struc}} = k_B T \nabla \ln \rho - \mathbf{f}_{\text{ad}}, \quad (45)$$

$$\mathbf{G}_{\text{struc}} = \frac{k_B T}{\rho} (\rho_1 \nabla \rho_2 - \rho_2 \nabla \rho_1), \quad (46)$$

where \mathbf{f}_{ext} is the total external force field given by the linear combination (18), and $\mathbf{F}_{\text{ext}}^{\Delta}$ is the differential external force density defined via (24); both fields depend on the partial density profiles. As all quantities on the right hand side of (43)-(46) are accessible in simulations, we have formulated a means to obtain a complete splitting of the nonequilibrium force contributions in the system.

The total species resolved superadiabatic force field is then given by

$$\mathbf{f}_{\text{sup}}^{\alpha} = \mathbf{f}_{\text{visc}} \pm \frac{\mathbf{G}_{\text{drag}}}{\rho_{\alpha}} + \mathbf{f}_{\text{struc}} \pm \frac{\mathbf{G}_{\text{struc}}}{\rho_{\alpha}}, \quad (47)$$

where the first (last) two terms in the right hand side act in flow (gradient) direction, and again \pm corresponds to $\alpha = 1, 2$.

In the results section we also analyze briefly a second case in ‘‘planar’’ geometry, in which there is only a single direction in the system (\mathbf{e}_y) along which the flow occurs and also all gradients point. The system is transitionally invariant in \mathbf{e}_x . As the flow occurs in the direction of the gradients, in general, such situations will be nonstationary, i.e. time-dependent.

B. Power functional approximation

Power functional theory [37] (PFT) is an exact variational approach to nonequilibrium dynamics in overdamped Brownian systems, which reduces to density functional theory in equilibrium. Within PFT, the superadiabatic force is obtained as a functional derivative with respect to the current

$$\mathbf{f}_{\text{sup}}^{\alpha} = -\frac{\delta P_{\text{exc}}[\{\rho_{\alpha'}, \mathbf{J}_{\alpha'}\}]}{\delta \mathbf{J}_{\alpha}}. \quad (48)$$

Here P_{exc} is the excess power functional [37], which is a functional of the density and current profiles of both species $\{\rho_{\alpha}, \mathbf{J}_{\alpha}\}$. The superadiabatic force is therefore also a functional of both types of one-body fields, density and current profiles.

Approximations for P_{exc} in monocomponent systems based on a series expansion of gradients of the velocity field have been proposed in Refs. [39, 42]. The resulting superadiabatic forces describe viscous [39] and structural effects [42]. In a binary mixture, besides the velocity gradients, the velocity difference between both species $\mathbf{v}_{\Delta} = \mathbf{v}_2 - \mathbf{v}_1$ is another key ingredient to construct approximated power functionals [43].

The following simple approximation for P_{exc} reproduces semiquantitatively all types of superadiabatic

forces in the system considered here:

$$P_{\text{exc}} = \frac{C_{\text{visc}}}{2} \int d\mathbf{r} \rho^2 (\nabla \times \mathbf{v})^2 \quad (49)$$

$$+ \frac{C_{\text{drag}}}{2} \int d\mathbf{r} \rho_1 \rho_2 \mathbf{v}_{\Delta}^2 \quad (50)$$

$$- C_{\text{struc}} \sum_{\alpha} \int d\mathbf{r} \rho^2 \mathbf{v}_{\Delta}^2 \nabla \cdot \mathbf{J}_{\alpha} \quad (51)$$

$$+ D_{\text{struc}} \sum_{\alpha} \int d\mathbf{r} \rho^2 [(\nabla \times \mathbf{v}_{\alpha}) \times \mathbf{v}_{\Delta}]' \cdot \mathbf{v}_{\Delta}. \quad (52)$$

The approximated, local in space and in time, functional contains four different terms, each one accounting of one type of superadiabatic force. The prefactors in front of each term are positive constants that represent the amplitudes of the superadiabatic force. We use these coefficients as fitting parameters. In reality, these prefactors depend on microscopic features of the model as the interparticle potential and are, in general, functionals of the density. The prime in Eq. (52) indicates the following time integral

$$[(\nabla \times \mathbf{v}_{\alpha}) \times \mathbf{v}_{\Delta}]' = \int_0^t dt' K(t-t') (\nabla \times \mathbf{v}'_{\alpha}) \times \mathbf{v}'_{\Delta}, \quad (53)$$

with $K(t)$ a temporal kernel, and the primes on the right hand side indicate dependence on t' .

The viscosity term (49) is the lowest order term in a power series expansion in the velocity gradient [39] and accounts for the Stokes-like viscous force. A similar term containing the square of the divergence of the average velocity instead of the square of the curl does not produce any force in the current setup since the flow, i.e. velocity profile, is free of divergence. The superadiabatic viscous force that results from differentiating Eq. (49) is species-independent

$$\mathbf{f}_{\text{visc}} = \frac{C_{\text{visc}}}{\rho} (\nabla \rho^2 \cdot \nabla \mathbf{v} - \nabla \cdot \rho^2 (\nabla \mathbf{v})^{\top}) \quad (54)$$

$$= \frac{C_{\text{visc}}}{\rho} \nabla_x (\rho^2 \nabla_x v_y(x)) \hat{\mathbf{y}}, \quad (55)$$

where the leftmost derivatives act on each entire expression, and the second equation (55) has been particularized for our current setup $\mathbf{v}(\mathbf{r}) = v_y(x) \hat{\mathbf{y}}$ and results in a force in flow direction.

The second term, Eq. (50), describes the drag of particles of one species due to the flow of particles of the other species [43]. The resulting superadiabatic force is species-dependent. The corresponding force density is:

$$\mathbf{G}_{\text{drag}} = C_{\text{drag}} \rho_1 \rho_2 \mathbf{v}_{\Delta}. \quad (56)$$

The structural superadiabatic force generated by the third term, Eq. (51), is species-independent

$$\mathbf{f}_{\text{struc}} = -C_{\text{struc}} \nabla (\rho \mathbf{v}_{\Delta})^2. \quad (57)$$

As we will see, this force cancels the sum of the adiabatic force and the diffusive force of the total density gradient.

The last term, Eq. (52), is also structural and the only one responsible of the superdemixing. The force density obtained via functional differentiation of Eq. (52) is

$$\mathbf{G}_{\text{struc}} = -D_{\text{struc}}\rho^2 \sum_{\alpha} [(\nabla \times \mathbf{v}_{\alpha}) \times \mathbf{v}_{\Delta}]', \quad (58)$$

where only the functional derivative with respect to unprimed velocity difference in (52) produces a force due to the structure of (53).

III. RESULTS

A. Model binary mixture

In the following we explicitly consider an equimolar two-dimensional binary mixture with a total of $N = 1066$ particles ($\mathcal{N}_1 = \mathcal{N}_2 = 532$) interacting via the same quasi-hard core pair potential $\phi(r) = \epsilon(\sigma/r)^{36}$. Here, σ denotes the characteristic particle length which sets the length scale, and ϵ sets the energy scale. The particles are subject to a homogeneous gravitational field in $\hat{\mathbf{y}}$ -direction,

$$\mathbf{f}_{\text{ext}}^{\alpha} = -m_{\alpha}g\hat{\mathbf{e}}_y, \quad (59)$$

where g is the acceleration due to gravity, $\hat{\mathbf{e}}_y$ is a unit vector along the vertical $\hat{\mathbf{y}}$ -direction, and m_{α} is the buoyant mass of species α . The only difference between the two species is that they have opposite buoyant masses, i.e., $m_1 = -m_2$. Although we make use of a gravitational field to illustrate the process of lane formation, other external fields such as magnetic and electric fields can also be used.

We simulate the system using Brownian dynamics simulations performed in a square simulation box of length $L/\sigma = 35$ with periodic boundary conditions in both directions. The total bulk density is hence $\rho_b\sigma^2 = N/L^2 = 0.87$. The temperature is fixed to $k_B T/\epsilon = 0.5$ and the friction coefficient is $\gamma = 1$. The particle trajectories are integrated in time via the Euler algorithm with a discrete time step $\Delta t/\tau = 3.0 \cdot 10^{-5}$ in units of the reduced time $\tau = \sigma^2\gamma/\epsilon$. The simulations of the laned state are initialized with the particles randomly located in a homogeneous state. Once the steady state is reached the system is sampled for a total time of $\sim 10^6 \tau$.

B. Laned state

The magnitude of the external force driving the two species against each other, $m_{\alpha}g$, highly influences the behaviour of the system. Without gravity, particles of both species form an effectively homogeneous one component system in equilibrium in which the only difference between the species is an arbitrary label. At low values of gravity, the steady state remains homogeneously mixed, and the particles are driven slowly through each other,

see a characteristic snapshot in Fig. 1a for a value of the external field $m_1g = 0.05 \epsilon/\sigma$. No forces act in the $\hat{\mathbf{x}}$ -direction. The internal interactions lead to weak superadiabatic drag forces in the flow $\hat{\mathbf{y}}$ -direction that partially counteract the external force.

For sufficiently high external driving, such as e.g. $m_1g = 1 \epsilon/\sigma$, the two species segregate into two lanes, see Fig. 1b. Each lane is characterized by the concentration of one species being significantly higher than that of the other (minority) species. In each lane there is a current of particles parallel to the external force corresponding to the dominant species. As shown in Sec. II there are superadiabatic drag and viscous forces opposing the external forces, see (36) and (37). Additionally, in the gradient $\hat{\mathbf{x}}$ -direction there is a balance of forces, see (38) and (39). The sum of the ideal diffusion and the adiabatic force tries to mix the two species. These forces are, however, canceled by structural superadiabatic forces that keep the system in the demixed laned steady state.

The density profiles of the laned state are shown in figure 2a. There, the right lane ($x > 0$) is dominated by species 1 that possesses a positive buoyant mass, i.e. the external force is directed downwards. In the left lane ($x < 0$) the majority of particles belongs to species 2 with negative buoyant mass and therefore an upwards directed external force. Although here species 1 predominantly occupies the right lane, the state is degenerated in the sense that a swap of the two lanes can be compensated by a shift by $L/2$ in the $\hat{\mathbf{x}}$ -direction (due to periodic boundary conditions). The total density profile, Fig. 2a, increases toward the centers of the lanes and decreases at the interfaces, although it is quite homogeneous as compared to the single species density profiles.

In Fig. 2b we show the velocity profiles. Only the flow component of the velocity profiles v_{α}^y does not vanish in steady state. The total velocity profile clearly shows the motion of particles in opposite directions in the two lanes, irrespective of the species. The total velocity is directed downwards in the right lane and upwards in the left lane, while being zero at the interfaces, as is consistent with the symmetry of the system.

Forces acting in flow direction. We focus first on the species resolved force balance equation (10). The flow components of the forces and the force densities are presented in Fig. 2c and 2d, respectively. In what follows we focus the discussion on species 1. Due to the symmetry of the system the behaviour of species 2 follows directly. Only two forces act in flow direction, the constant external force field $\mathbf{f}_{\text{ext}}^{\alpha}$ (59), and the superadiabatic force field due to interparticle interactions $\mathbf{f}_{\text{sup}}^{\alpha}$. Adiabatic $\mathbf{f}_{\text{ad}}^{\alpha}$ and diffusive $-k_B T \nabla \ln \rho_{\alpha}$ forces appear only when gradients of the density profile are present. As the system is homogeneous in the flow direction, such contributions do not occur in this direction. Therefore, the internal forces in flow direction are purely superadiabatic.

For those particles located in the lane for which its species is majority (e.g. species 1 in the right lane in Fig. 2b), the velocity and the external force are parallel,

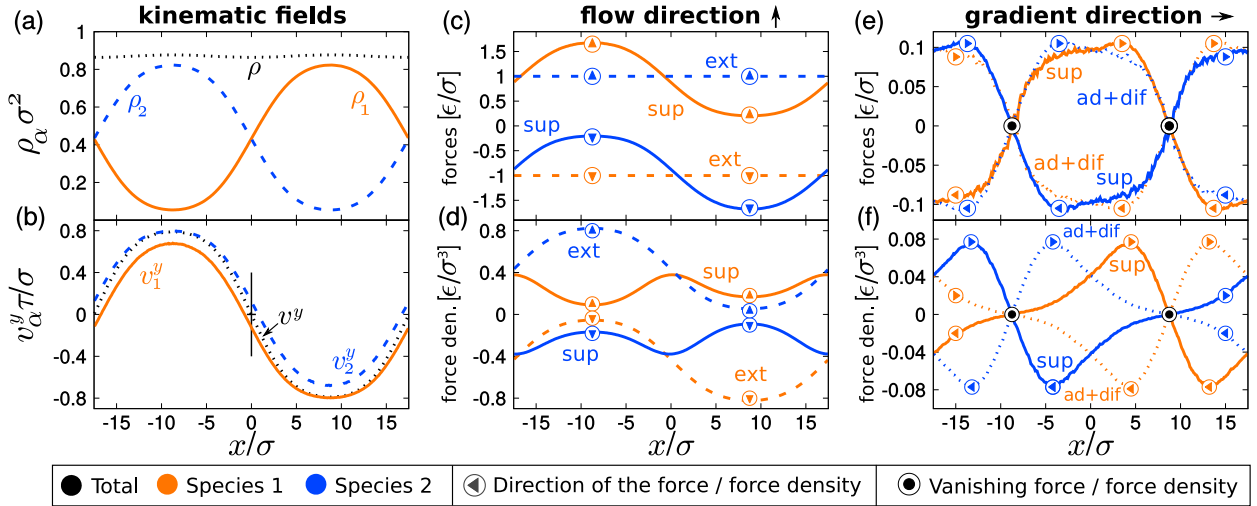


FIG. 2: Lane formation. Kinematic fields: (a) total density profile ρ (black dotted line) and partial density profiles ρ_1 (orange solid line) and ρ_2 (blue dashed line), (b) flow component of the total velocity profile v^y (black dotted line), see (13), and of the partial velocity profiles v_1^y (orange solid line) and v_2^y (blue dashed line). Species resolved forces (c) and force densities (d) acting in flow direction (10): external $\mathbf{f}_{\text{ext}}^\alpha$ (dashed lines), and superadiabatic $\mathbf{f}_{\text{sup}}^\alpha$ (solid lines), which is the sum of viscous and drag (47). Species resolved forces (e) and force densities (f) acting in gradient direction: sum of adiabatic and diffusive forces (dotted lines) and superadiabatic (solid lines), see (42). In all plots the line color indicates the species: orange (blue) for species 1 (2). The arrows indicate the direction of the force or force density. Black circles indicate points where the force or force density vanishes. All plots are for driving $m_1 g = 1.0\epsilon/\sigma$ and all values are presented as functions of the x -coordinate.

while the internal force opposes both. For those particles in the lane for which its species is minority (e.g. species 2 in the right lane in Fig. 2b) the velocity and the external force are antiparallel. This is caused by a strong internal force, mostly created by particles of the opposite species which dominates the lane, that drags the particles of the minority species. The force densities in flow direction are shown in Fig. 2d. The force densities are the actual contributions to the current of particles (up to a multiplicative constant given by the inverse friction coefficient) and are therefore a macroscopically accessible quantity.

Next, we split the species resolved superadiabatic forces (47) in flow direction in its species-dependent and species-independent contributions (41), which are the viscous \mathbf{f}_{visc} (43) and the drag $\pm\mathbf{G}_{\text{drag}}$ (44) superadiabatic contributions, respectively.

The results are shown in Fig. 3a (forces) and Fig. 3b (force densities). The species-dependent term $\pm\mathbf{G}_{\text{drag}}$ is the dominant part and describes the drag of one species due to motion of the other species. For example, for species 1 this force density is high in the lane of particles of species 2 (left lane) and points upwards. The species-independent force \mathbf{f}_{visc} points in the direction opposite to the total velocity \mathbf{v} , as corresponds to a viscous effect. The amplitude of the viscous force is relatively small as compared to that of the drag force. However, the maxima (absolute value) of \mathbf{f}_{visc} occur at the peaks of the partial densities. As a result, the viscous force density $\rho_\alpha \mathbf{f}_{\text{visc}}$ introduces a relevant correction to the dominant species-dependent force density, see Fig. 3b.

A comparison between the Stokes-like viscous force predicted by our power functional approximation (55) and the viscous force measured in simulations is shown in Fig. 3a (inset). The predicted force has the correct sign everywhere (opposite of the total flow). However, due to the spatially local approximation taken in (55) and the strong driving conditions, the agreement is not perfect. The drag force predicted by PFT, cf. (56), also shows a good agreement with the simulation data, see Fig. 3b.

Forces acting in gradient direction. In the gradient direction $\hat{\mathbf{x}}$, which is perpendicular to the flow, no external force is applied and the system is in steady state with no flow along this direction, cf. (42). The density modulation (formation of lanes), Fig. 2a, is solely created by the flow along $\hat{\mathbf{y}}$, Fig. 2b.

The species resolved net force balance (10) is zero in $\hat{\mathbf{x}}$, and both adiabatic $\mathbf{f}_{\text{ad}}^\alpha$ and superadiabatic $\mathbf{f}_{\text{sup}}^\alpha$ forces contribute to the internal force. For species 1 the sum of adiabatic and diffusive, $-k_B T \nabla \ln \rho_\alpha$, forces attempts to move particles in the center of the simulation box to the left and particles at the borders of the box to the right, see Figs. 2e and 2f. That is, as could be expected, the sum of the diffusive and the adiabatic forces pushes particles outside of the majority lane and therefore tries to mix the two species by eliminating density gradients. The superadiabatic force in gradient direction balances the diffusion and the adiabatic forces by pushing particles into their majority lane and out of their minority lane, Fig. 2e,f. The superadiabatic force is therefore the only force that creates and sustains the demixing and segre-

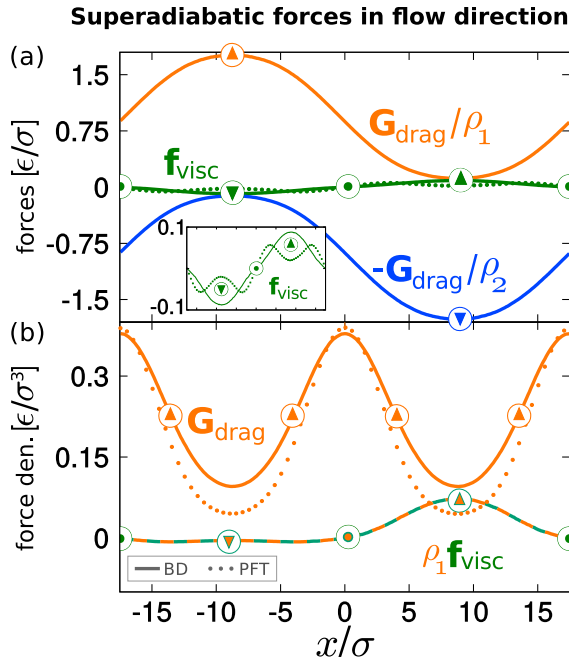


FIG. 3: Superadiabatic forces in flow directions as a function of the x -coordinate. (a) Species-independent superadiabatic force \mathbf{f}_{visc} (dark solid green), species-dependent superadiabatic force acting on species 1 (solid orange), $\mathbf{G}_{\text{drag}}/\rho_1$, and 2 (solid blue), $-\mathbf{G}_{\text{drag}}/\rho_2$. (b) Species-dependent force density \mathbf{G}_{drag} acting on species 1 (solid orange), and species-independent force density acting on species 1 (orange-dark green), $\rho_1 \mathbf{f}_{\text{visc}}$. The arrows (colored according to the corresponding data set) indicate the direction of the force. The symbols show the theoretical predictions for the viscous force (a) force and the drag force density (b). We have set $C_{\text{visc}} = 2 \epsilon \tau \sigma^2$ and $C_{\text{drag}} = 8.5 \epsilon \tau$ in equations (55) and (56), respectively.

gation into lanes in steady state. Superadiabatic forces are therefore crucial for the description of lane formation, as expected given the nonequilibrium nature of the phenomenon.

The adiabatic forces are obtained by sampling the internal forces in the adiabatic equilibrium system. The adiabatic equilibrium system is also a symmetric mixture with the same quasi-hard interparticle interactions regardless of the species. The only difference between the real nonequilibrium and the adiabatic equilibrium systems is that the external nonconservative driving force is switched off in the adiabatic equilibrium system and replaced by conservative external forces generated by two potentials V_{ad}^α that reproduce the same density profiles as in nonequilibrium. The adiabatic potentials are obtained following the method described in Appendix A, which also shows for both species the adiabatic potentials and the density profiles in the adiabatic system.

In the adiabatic system the external potential counteracts both the ideal diffusive force $-k_B T \nabla \ln \rho_\alpha$ and the adiabatic force $\mathbf{f}_{\text{ad}}^\alpha$. The diffusive force and the adiabatic

force have two very distinct effects, which are schematically illustrated in Fig. 4a. Quantitative plots of both force and force density profiles are shown in Fig. 4b for species 1 and in Fig. 4c for species 2. The diffusive force is the only force that attempts to mix both species. In contrast, the adiabatic force field is the same for all particles, independently of the species, due to the symmetry of the internal interactions. That is $\mathbf{f}_{\text{ad}}^\alpha = \mathbf{f}_{\text{ad}}$, as discussed in Sec. II. The adiabatic force tries to eliminate the density gradients of the total density profile $\rho = \rho_1 + \rho_2$ by pushing particles of both species toward the interfaces between the two lanes.

We next split the species resolved superadiabatic forces (47) into the species-independent $\mathbf{f}_{\text{struc}}$ (45) and the species-dependent $\pm \mathbf{G}_{\text{struc}}$ (46) contributions in gradient direction. Both contributions are of the structural type in the sense that they sustain the density gradients and are non-dissipative. Fig. 5a illustrates schematically the different effects of $\mathbf{f}_{\text{struc}}$ and $\mathbf{G}_{\text{struc}}$. The actual profiles are displayed in Fig. 5b.

The species-independent superadiabatic force in gradient direction $\mathbf{f}_{\text{struc}}$ pushes particles from the interfaces toward the centers of the lanes, creating the total density modulation, see Fig. 5b (top). $\mathbf{f}_{\text{struc}}$ is almost the opposite of the adiabatic force \mathbf{f}_{ad} , as shown in Fig. 5c (top) where we plot the adiabatic force, and $-\mathbf{f}_{\text{struc}}$. These two terms, however, do not exactly cancel each other as the sum of $\mathbf{f}_{\text{struc}}$ and the adiabatic force shows a clear signal (see the bottom panel of Fig. 5c) that cancels exactly the diffusive force originated by the gradient of the total density profile, cf. (45). This diffusive term also describes a species-independent effect.

The species-dependent force density $+\mathbf{G}_{\text{struc}}$ transports particles of species 1 away from the left lane into the right lane, see Fig. 5b (bottom). The term $-\mathbf{G}_{\text{struc}}$ acts on particles of species 2 in the opposite way. This superadiabatic contribution is precisely the opposite of the contribution due to the local demixing, compare Fig. 5b (bottom) and the diffusive force density shown in Fig. 4b (bottom). Therefore, the species-dependent term $\mathbf{G}_{\text{struc}}$ sustains the demixing of the two species in two lanes in steady state.

The sum of both superadiabatic structural terms in gradient direction cancels the diffusive and the adiabatic contributions (42). Our power functional approximation, Eqs. (45) and (46), is in very good agreement with the simulation data for both $\mathbf{f}_{\text{struc}}$ and $\mathbf{G}_{\text{struc}}$ as shown in Figs. 5b and 5c, respectively.

C. Jammed state

We conclude the results section with a brief discussion of the jammed state, see Fig. 6a, that can be found at intermediate values of gravity, and in which flow and gradient directions coincide. This state occurs if the two species block each other during the diffusing process induced by the external field. The state is homogeneous in

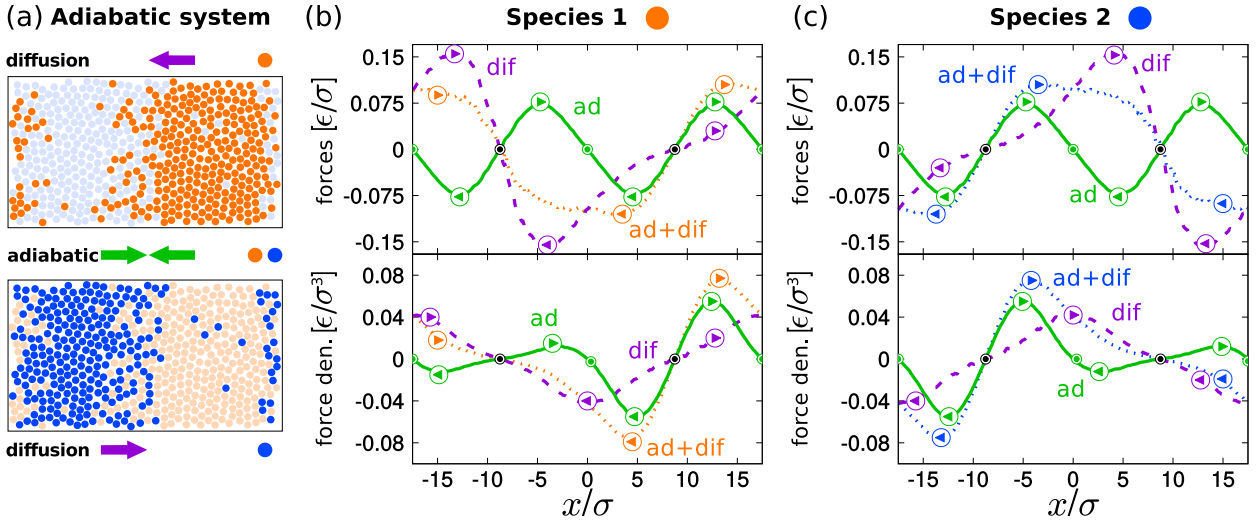


FIG. 4: Adiabatic forces. (a) Partial snapshots of the laned state at gravity $m_1g = 1.0\epsilon/\sigma$. The arrows indicate the direction of the adiabatic forces acting on species 1 (top) and 2 (bottom). The diffusive force field $-k_B T \nabla \ln \rho_\alpha$ (violet arrows) tries to mix both species. The adiabatic force field (green) is the same for both species. (b) Force (top panel) and force density (bottom panel) profiles acting on species 1 in \hat{x} -direction as a function of x : total force: adiabatic plus diffusion (orange dotted), diffusive force (violet dashed), and adiabatic force (green solid). (c) Same as panel (b) but for species 2: total force (blue dotted), diffusion (violet dashed), and adiabatic (green solid).

\hat{x} -direction, and it is characterized by a significant change of the total density in \hat{y} -direction. The opposite external driving of the two species leads to the formation of a compressed region with similar concentrations of both species, high total density, and incipient crystalline order. This region is surrounded by two regions rich in particles of only one species that press against the compressed area. In the jammed state strong superadiabatic forces act against the external fields. Additionally, the adiabatic and diffusive forces try to smooth the total density profile. In contrast to the laned state, the demixing in the jammed state occurs along the direction of the external driving force. In our simulations the jammed state is metastable but it stays for very long times allowing a systematic study of the forces.

To characterize the jammed state we set the gravity to $m_1g = 0.7\epsilon/\sigma$ and split the time evolution of the system in time windows of 20τ . Only those time windows in which the difference between the maximum and the minimum of the total density is higher than $0.2\sigma^2$ are considered to be in the jammed state. Using several simulations, we average over these relevant windows for a total sampling time of $10^5\tau$. The density profiles, Fig. 6b, show the demixing along the \hat{y} -axis. The particles of species 1 (2) accumulate at the top (bottom) of the simulation box. In the center of the box there is a region with similar concentrations of both species. The total density shows a small modulation with a global maximum located in the middle of the box (in each time window we translate the data such that the maximum density occurs in the middle of the box). The velocity profiles are shown in Fig. 6b. Only the \hat{y} -component of the velocity

is non-zero. The total velocity is almost negligible across the complete simulation box. The velocity of species 1 almost vanishes everywhere except at the bottom of the box, the region rich in particles of species 2. Here, the velocity of species 1 is negative. Hence, particles of species 1 move toward the top of the simulation box (we use periodic boundary conditions) where the species 1 dominates. Exactly the opposite behaviour is observed in species 2, as expected due to symmetry considerations.

The total current vanishes, see inset Fig. 6c, and the partial currents are small and indicate the system is still under compression. Given that the partial currents are not constant, it is clear the system is not in steady state. Nevertheless, the currents are very small and rather homogeneous, which justifies the assumption of a quasi-steady state. For other systems the jammed state has been observed to be steady. This is the case of a 2D hard disk system with very low opposite driving at zero temperature [44], and also on a square lattice model [20].

The species resolved forces in \hat{y} -direction split into diffusion, adiabatic, superadiabatic, and external, see (10). Plots of each contribution are shown in Fig. 6d. We compute the adiabatic force via the adiabatic potential, as described in the Appendix A.

The external force for both species points in opposite directions and it is constant in space. The sum of the thermal diffusion and the adiabatic force is for both species positive at the top and mostly negative at the bottom of the simulation box. Hence, this force field tries to smooth the density modulations by transporting particles away from the center toward the low density regions. The superadiabatic force for species 1 is every-

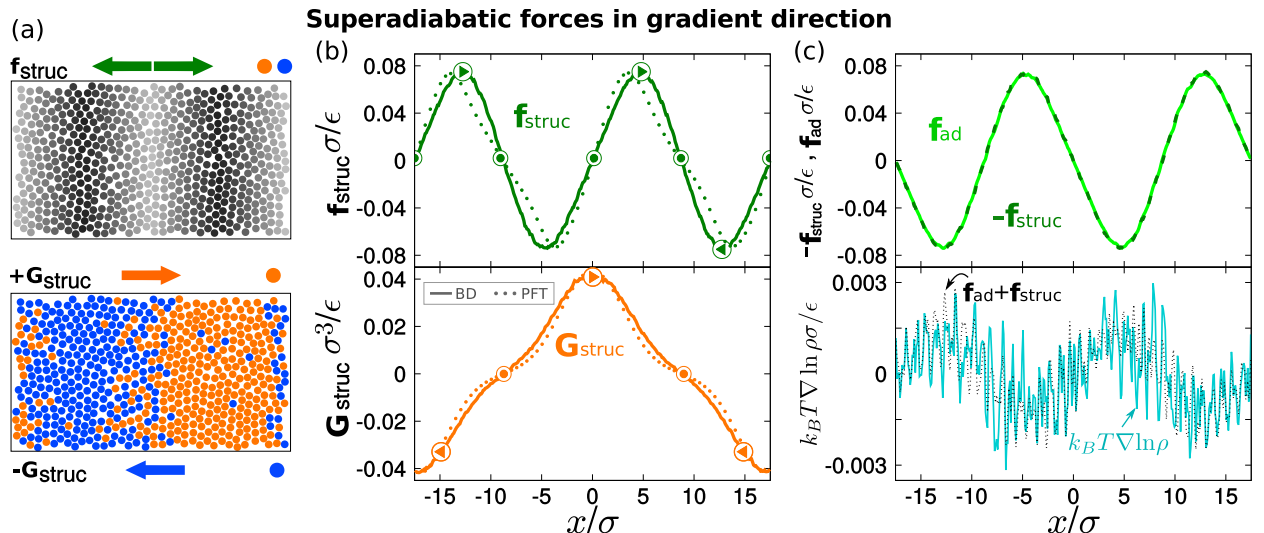


FIG. 5: Superadiabatic forces in gradient direction. (a) Partial snapshots of the laned state ($m_1 g = 1.0 \epsilon / \sigma$). The arrows indicate the direction of the species-independent $\mathbf{f}_{\text{struc}}$ (top) and dependent $\pm \mathbf{G}_{\text{struc}}$ (bottom) superadiabatic forces in gradient direction. In the top panel the brightness of the particles indicates the total density modulation (brighter regions are less dense). (b) Species-independent superadiabatic force $\mathbf{f}_{\text{struc}}$ (top panel) and species-dependent force density $\mathbf{G}_{\text{struc}}$ acting on species 1 (bottom panel). Lines are simulation data and symbols denote the power functional approximation given in Eqs. (45) and (46) with parameters $C_{\text{struc}} = 10.5 \epsilon \tau^2 \sigma^2$, and $D_{\text{struc}} = 0.73 \epsilon \tau^2$. (c) Top panel: Negative of the species-independent superadiabatic force $-\mathbf{f}_{\text{struc}}$ (dark green dashed) and the adiabatic excess force \mathbf{f}_{ad} (bright green solid). Bottom panel: Negative of the thermal diffusion force associated to the total density (blue) and sum of the species-independent superadiabatic force and the adiabatic force (black dotted).

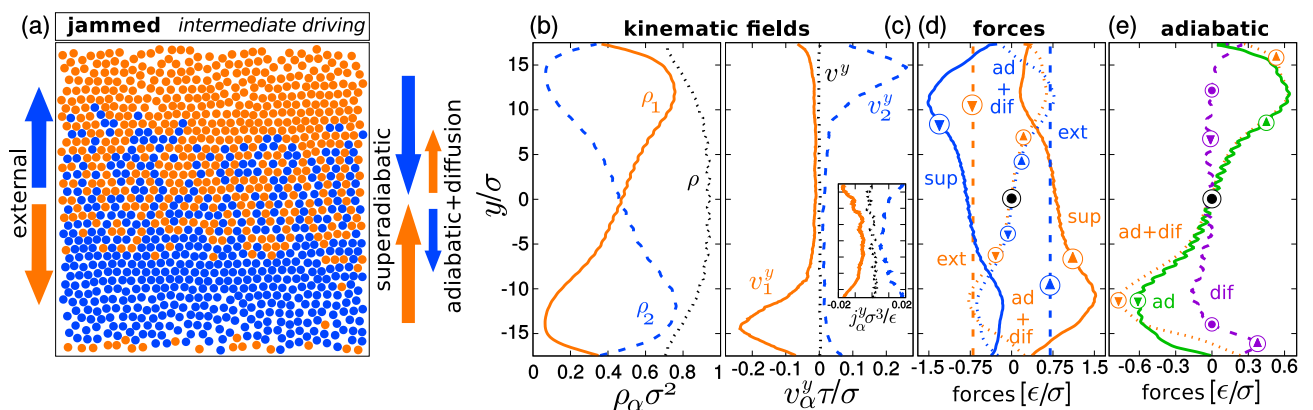


FIG. 6: Jammed state formed at intermediate values of the external driving. (a) Characteristic snapshot. The orange (blue) arrows indicate the forces acting on species 1 (2). (b) Total density profile ρ (black dotted line), and partial density profiles ρ_1 (solid orange) and ρ_2 (blue dashed). (c) Total velocity profile v (black dotted), and partial velocity profiles v_1 (orange solid) and v_2 (blue dashed). The inset shows the current profiles: total current profile j (black dotted), and partial current profiles j_1 (orange solid) and j_2 (blue dashed). (d) Forces acting in \hat{y} -direction: external (dashed), diffusive plus adiabatic (dotted), and superadiabatic (solid). The color indicates the species: orange (blue) for species 1 (2). (e) Adiabatic and diffusive forces acting in \hat{y} -direction acting on species 1: Sum of both forces (orange dotted), adiabatic (green solid), and ideal diffusion (purple dashed). Data obtained for a value of gravity $m_1 g = 0.7 \epsilon / \sigma$. All quantities are presented as a function of the y -coordinate.

where directed upwards against the external force and has a maximum at the bottom of the sample, the region dominated by species 2.

The thermal diffusion and the adiabatic force acting on species 1 are shown in Fig. 6e. The adiabatic force is

positive at the top of the box and negative at the bottom, moving particles away from the center in order to smooth the total density profile. Similarly, the ideal diffusion force tries to smooth the partial density profile of species 1.

Recall that in the laned state, the diffusive force is the only force counteracting the demixing, while the adiabatic force has a phenomenological irrelevant effect. In the jammed state, however, the adiabatic force has a prominent effect while the diffusion term is only a small contribution to the forces present in the adiabatic state. The flow in the jammed state is curl free instead of divergence free (which is the case in the laned state). Hence, the leading terms in the expansion of the excess free power for the viscous and the species-independent structural forces will differ from those in Eqs. (49) and (52), respectively.

IV. CONCLUSIONS

By splitting the nonequilibrium superadiabatic forces of a colloidal mixture into species-dependent and independent contributions, we have identified a structural force contribution that induces demixing of two different species in nonequilibrium. This superadiabatic force is responsible for the formation of lanes in oppositely driven binary colloidal systems. The force counteracts the ideal thermal diffusive force that arises as a consequence of the mixing entropy generated by a gradient in composition between the two lanes.

The entropy driven demixing that occurs in mixtures of hard bodies, see e.g. Ref. [45], is a well known phenomenon. There, the excess free energy (adiabatic force) originated from particle interactions counteracts the ideal entropy of mixing (diffusive force) and sustains the density gradients. The mechanism behind the demixing in lane formation is completely different. Here, the adiabatic force only leads to a minor modulation of the total density and does not attempt to demix the species. Although we have analysed ideal symmetric mixtures, we expect this to be true also in asymmetric mixtures that could be considered in future studies.

Lane formation is a purely superadiabatic effect. Consequently a direct theoretical description of laning via dynamical density functional theory [46–48], in which only adiabatic forces are considered, is not possible and phenomenological ad-hoc corrections must be included [13]. We have presented here a different approach based on power functional theory [37], an exact variational approach for nonequilibrium situations. Power functional theory incorporates superadiabatic effects via a functional of both density and velocity profiles. Our power functional approximation reproduces semiquantitatively all superadiabatic forces present in the system, and, to the best of our knowledge, it constitutes the first theoretical approach that describes lane formation from first principles.

Although we have focused our study on lane formation, our approach to analyse the force contributions and our power functional approximation are general and applicable to other out-of-equilibrium situations in multicomponent colloidal systems. In particular, our work paves the

way to study superadiabatic forces inside channels where ratchet-like wall shapes can determine the direction of the motion within the lanes [49], and the description using power functional theory of the complete dynamics of sedimentation of binary mixtures from an initial uniform state to the formation of the sedimentation-diffusion-equilibrium stacking sequence [50, 51]. The power functional approach presented here can also help to understand the differences and similarities between lane formation in oppositely driven mixtures and in one-component sheared systems [52, 53]. There, the formation of lanes in steady state is induced by a shear field and likely sustained by a superadiabatic force.

Appendix A: Adiabatic construction

The internal force field is a functional of the density and the velocity profiles and can be split into adiabatic and superadiabatic contributions. Mathematically, the adiabatic force is the term that depends only on the density profile. Physically, the adiabatic force represents the internal force of an equilibrium system that shares the same density profile(s) as the actual out-of-equilibrium system. In Ref. [41] Fortini et. al. presented the first simulation method for sampling the superadiabatic forces in a monocomponent BD nonequilibrium system. The method relies on numerically finding the adiabatic external potential that generates the desired density profile in equilibrium. A related and improved iterative (custom flow) method to numerically find the adiabatic potential is presented in Ref. [40]. We follow here another approach to find the adiabatic potential based on classical density functional theory (DFT) [46]. In DFT the adiabatic force is a functional of the one-body density profiles

$$\mathbf{f}_{\text{ad}}^{\alpha} = -\nabla \frac{\delta F_{\text{exc}}[\{\rho_{\alpha'}\}]}{\delta \rho_{\alpha}}, \quad (\text{A1})$$

where $F_{\text{exc}}[\{\rho_{\alpha'}\}]$ is the excess (over ideal) Helmholtz free energy functional.

The adiabatic system is obtained by finding the species-dependent conservative adiabatic potentials $V_{\text{ad}}^{\alpha}(x, t)$, which are constructed such that the equilibrium one-body densities for both species in the adiabatic (equilibrium) system equal those in the nonequilibrium system. For the laned system, the system is homogeneous in the flow $\hat{\mathbf{y}}$ -direction and therefore the adiabatic potentials can only depend on the x -coordinate. In the adiabatic (equilibrium) system, the force balance reads

$$-k_B T \nabla \ln \rho_{\alpha} + \mathbf{f}_{\text{ad}}^{\alpha}(x) - \nabla V_{\text{ad}}^{\alpha}(x) = 0. \quad (\text{A2})$$

In order to sample the adiabatic reference system of the laned state, we use Monte Carlo simulations with the same values of \mathcal{N}_{α} , L , and $k_B T$ as the nonequilibrium BD system. We initialize the adiabatic system with a configuration taken from the BD simulations and then equilibrate the system. The maximum displacement each

particle is allowed to move in one Monte Carlo step is set such that 25 – 30% of the moves are accepted. We then sample data for $\sim 10^{11}$ Monte Carlo sweeps (MCS). A MCS is defined as an attempt to individually move all particles in the system.

In Refs. [40, 41] iterative methods for finding the adiabatic potential that enters in Eq. (A2) are presented. An initial guess for the potential is iteratively adjusted until the density profile equals the corresponding counterpart in the nonequilibrium system. Here, we have to match two density profiles, one for each species. As the modulation of the total density is small, a calculation of the adiabatic potentials using a simple density functional based on the equation of state of scaled particle theory (SPT) for hard-disks yields excellent results. Within SPT the compressibility factor of an homogeneous system of hard disks is $Z = (1 - \eta)^{-2}$ [54], with $\eta = \rho_b \pi \sigma^2 / 4$ the total packing fraction of the system. Here ρ_b is the bulk density. An expression for the excess free energy per particle ψ_{exc} follows from Z via a volume integral [55]:

$$\psi_{\text{exc}}(\rho_b) = \int_0^\eta d\eta' \frac{Z - 1}{\eta'} = -\ln(1 - \eta) + \frac{\eta}{1 - \eta}. \quad (\text{A3})$$

Using the above expression we construct an approximation for the excess free energy functional

$$\beta F_{\text{exc}}[\rho] = \int dx \rho(x) \psi_{\text{exc}}(\bar{\rho}), \quad (\text{A4})$$

in which the excess free energy is evaluated in a weighted density given by

$$\bar{\rho}(x) = \frac{1}{\sigma} \int_{x-\sigma/2}^{x+\sigma/2} dx' \rho(x'). \quad (\text{A5})$$

Since the mixture is symmetric only the total density $\rho = \rho_1 + \rho_2$ enters the expression for the excess free energy. The resulting adiabatic force \mathbf{f}_{ad} via functional differentiation is species-independent and directed along the gradient direction

$$\mathbf{f}_{\text{ad}}(x) = \mathbf{f}_{\text{ad}}^\alpha(x) = -\nabla \frac{\partial F_{\text{exc}}[\rho]}{\partial \rho(x)}. \quad (\text{A6})$$

Eqs. (A2) and (A6) yield an expression for the species-dependent adiabatic potential

$$\beta V_{\text{ad}}^\alpha(x) = -\ln(\rho_\alpha \Lambda_\alpha) - \psi_{\text{exc}}(\bar{\rho}) \quad (\text{A7})$$

$$-\frac{1}{\sigma} \int dx' \rho(x') \frac{\partial \psi_{\text{exc}}(\bar{\rho})}{\partial \rho}, \quad (\text{A8})$$

where Λ_α is the (irrelevant) thermal wavelength of species α and the spatial argument of $\bar{\rho}$ and η was omitted for clarity.

Fig. 7a displays results for the adiabatic potentials. As expected, the potential for each species is high in the region of the respective minority lane and low in the majority lane, with a total difference between maximum and minimum of approximately 1.3ϵ (equal to $2.6k_B T$).

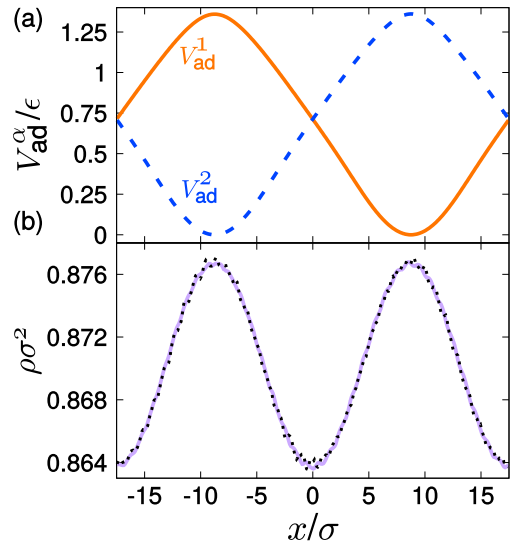


FIG. 7: Adiabatic potentials. (a) Adiabatic external potentials V_{ad}^α in the adiabatic (equilibrium) system for species 1 (orange solid) and species 2 (blue dashed) as a function of x . (b) Total density profile ρ sampled via BD in nonequilibrium steady state (black dotted) and via MC in the corresponding adiabatic equilibrium system (violet solid).

The external forces created by the two adiabatic potentials segregate the two species in the equilibrium system. In Fig. 7b we present the total density sampled in the adiabatic system and that in the nonequilibrium system. Both systems have almost the same density profiles, which shows the quality of the adiabatic construction. The species-dependent density profiles in the adiabatic system are also in very good agreement with those in out-of-equilibrium (not shown).

-
- [1] Binary mixtures of hard spheres: how far can one go with the virial equation of state? A. Y. Vlasov, A. J. Masters, Fluid Phase Equi. **212**, 183 (2003).
 [2] Entropy driven phase transitions in colloid-polymer suspensions: Tests of depletion theories, S. Ramakrishnan,

- M. Fuchs, K. S. Schweizer, and C. F. Zukoski, J. Chem. Phys. **116**, 2201, (2002)
 [3] Understanding liquid-liquid immiscibility and LCST behaviour in polymer solutions with a Wertheim TPT1 description, P. Paricaud, A. Galindo, and G. Jackson, Mol.

- Phys. **101**, 2575 (2003).
- [4] Study of the demixing transition in model athermal mixtures of colloids and flexible self-excluding polymers using the thermodynamic perturbation theory of Wertheim, P. Paricaud, S. Varga, and G. Jackson, *J. Chem. Phys.* **118**, 8525 (2003).
- [5] Theory of the isotropic nematic nematic phase-separation for a solution of bidisperse rodlike particles, G. J. Vroege, H. N. W. Lekkerkerker, *J. Phys. Chem.* **97**, 3601 (1993).
- [6] Phase behavior of symmetric rod-plate mixtures revisited: Biaxiality versus demixing, S. Varga, A. Galindo, G. Jackson, *J. Chem. Phys.* **117**, 10412 (2002).
- [7] Percolation in binary and ternary mixtures of patchy colloids, F. Seiferling, D. de las Heras, M. Telo da Gama, *J. Chem. Phys.* **145**, 074903 (2016).
- [8] Selectivity in binary fluid mixtures: Static and dynamical properties, R. Roth, M. Rauscher, A. J. Archer, *Phys. Rev. E* **80** 021409 (2009).
- [9] Capacitive Mixing for Harvesting the Free Energy of Solutions at Different Concentrations, R. A. Rica, R. Ziano, D. Salerno, F. Mantegazza, R. van Roij, D. Brogioli, *Entropy* **15**, 1388 (2013).
- [10] 'Blue energy' from ion adsorption and electrode charging in sea and river water, N. Boon, and R. van Roij, *Mol. Phys.* **109**, 1229 (2011).
- [11] Gradient dynamics models for liquid films with soluble surfactant, U. Thiele, A. J. Archer, and L. M. Pismen, *Phys. Rev. Fluids* **1**, 083903 (2016).
- [12] Lane formation in colloidal mixtures driven by an external field, J. Dzubiella, G. P. Hoffmann, and H. Löwen, *Phys. Rev. E* **65**, 021402 (2002).
- [13] Dynamical instability in driven colloids, J. Chakrabarti, J. Dzubiella, and H. Löwen, *Europhys. Lett.* **61**, 415 (2003).
- [14] Reentrance effect in the lane formation of driven colloids, J. Chakrabarti, J. Dzubiella, and H. Löwen, *Phys. Rev. E* **70**, 012401 (2004).
- [15] Ionic colloidal crystals of oppositely charged particles, M. E. Leunissen, C. G. Christova, A.-P. Hynninen, C. P. Royall, A. I. Campbell, A. Imhof, M. Dijkstra, R. van Roij, and A. van Blaaderen, *Nature* **437**, 235 (2005).
- [16] Lane formation in oppositely charged colloids driven by an electric field: Chaining and two-dimensional crystallization, M. Rex and H. Löwen, *Phys. Rev. E* **75**, 051402 (2007).
- [17] Lane formation in driven mixtures of oppositely charged colloids, T. Vissers, A. Wysocki, M. Rex, H. Löwen, C. P. Royall, A. Imhof, and A. van Blaaderen, *Soft Matter* **7**, 2352 (2011).
- [18] Dynamics of Lane Formation in Driven Binary Complex Plasmas, K. R. Sütterlin, A. Wysocki, A. V. Ivlev, C. Räh, H. M. Thomas, M. Rubin-Zuzic, W. J. Goedheer, V. E. Fortov, A. M. Lipaev, V. I. Molotkov, O. F. Petrov, G. E. Morfill, and H. Löwen, *Phys. Rev. Lett.* **102**, 085003 (2009).
- [19] Model experiment for studying lane formation in binary complex plasmas, C.-R. Du, K. R. Sütterlin, A. V. Ivlev, H. M. Thomas, and G. E. Morfill, *EPL (Europhysics Lett.)* **99**, 45001 (2012).
- [20] Lane formation in a lattice model for oppositely driven binary particles, H. Ohta, *EPL (Europhysics Lett.)* **99**, 40006 (2012).
- [21] Unidirectional laning and migrating cluster crystals in confined self-propelled particle systems, A. M. Menzel, *J. Phys. Condens. Matter* **25**, 505103 (2013).
- [22] Self-organized lane formation and optimized traffic flow in army ants, I. D. Couzin and N. R. Franks, *Proc. R. Soc. London B* **270**, 139 (2003).
- [23] Crossing pedestrian traffic flows, the diagonal stripe pattern, and the chevron effect, J. Cividini, H. Hilhorst, and C. Appert-Rolland, *J. Phys. A Math. Gen.* **46**, H5002 (2013).
- [24] Pattern formation in driven colloidal mixtures: tilted driving forces and re-entrant crystal freezing, J. Dzubiella and H. Löwen, *J. Phys. Condens. Matter* **14**, 9383 (2002).
- [25] Shear-induced laning transition in a confined colloidal film, S. Gerloff, T. A. Vezirov, and S. H. Klapp, *Phys. Rev. E* **95**, 062605 (2017).
- [26] Oscillatory driven colloidal binary mixtures: Axial segregation versus laning, A. Wysocki and H. Löwen, *Phys. Rev. E* **79**, 041408 (2009).
- [27] Flow generation by rotating colloids in planar microchannels, I. O. Götze and G. Gompper, *EPL* **92**, 64003 (2010).
- [28] Exploiting non-equilibrium phase separation for self-assembly, M. Grünwald, S. Tricard, G. M. Whitesides, and P. L. Geissler, *Soft Matter* **12**, 1517 (2016).
- [29] Influence of hydrodynamic interactions on lane formation in oppositely charged driven colloids, M. Rex and H. Löwen, *Eur. Phys. J. E* **26**, 143 (2008).
- [30] Should "lane formation" occur systematically in driven liquids and colloids? J. Delhomelle, *Phys. Rev. E* **71**, 016705 (2005).
- [31] The nature of the laning transition in two dimensions, T. Glanz and H. Löwen, *J. Phys. Condens. Matter* **24**, 464114 (2012).
- [32] Lane formation in a driven attractive fluid, C. W. Wächter, F. Kogler, and S. H. L. Klapp, *Phys. Rev. E* **94**, 052603 (2016).
- [33] Lane formation in a system of dipolar microswimmers, F. Kogler and S. H. Klapp, *EPL* **110**, 10004 (2015).
- [34] Microscopic origin and macroscopic implications of lane formation in mixtures of oppositely driven particles, K. Klymko, P. L. Geissler, and S. Whitlam, *Phys. Rev. E* **94**, 022608 (2016).
- [35] Universal Long Ranged Correlations in Driven Binary Mixtures, A. Poncet, O. Bénichou, V. Démery, and G. Oshanin, *Phys. Rev. Lett.* **118**, 118002 (2017).
- [36] Microscopic theory for anisotropic pair correlations in driven binary mixtures, M. Kohl, A. V. Ivlev, P. Brandt, G. E. Morfill, and H. Löwen, *J. Phys.: Condens. Matter* **24**, 464115 (2012).
- [37] Power functional theory for Brownian dynamics, M. Schmidt and J. M. Brader, *J. Chem. Phys.* **138**, 214101 (2013).
- [38] Power functional theory for the dynamic test particle limit, J. M. Brader, M. Schmidt, *J. Phys.: Condens. Matter* **27**, 194106 (2015).
- [39] Velocity gradient power functional for Brownian dynamics, D. de las Heras and M. Schmidt, *Phys. Rev. Lett.* **120**, 028001 (2018).
- [40] Custom flow in overdamped Brownian dynamics, D. de las Heras, J. Renner, and M. Schmidt, *Phys. Rev. E* **99**, 023306 (2019).
- [41] Superadiabatic forces in Brownian many-body dynamics, A. Fortini, D. de las Heras, J. M. Brader, and M. Schmidt, *Phys. Rev. Lett.* **113**, 167801 (2014).
- [42] Structural nonequilibrium forces in driven colloidal systems, N. C. X. Stuhmüller, T. Eckert, D. de las Heras,

- and M. Schmidt, Phys. Rev. Lett. **121**, 098002 (2018).
- [43] Nonequilibrium phase behaviour from minimization of free power dissipation, P. Krinninger, M. Schmidt, and J. M. Brader, Phys. Rev. Lett. **117**, 208003 (2016).
- [44] Velocity force curves, laning, and jamming for oppositely driven disk systems, C. Reichhardt and C. J. O. Reichhardt, Soft Matter **14**, 490 (2018).
- [45] Entropically driven microphase transitions in mixtures of colloidal rods and spheres, M. Adams, Z. Dogic, S. L. Keller, and S. Fraden, Nature **393**, 349 (1998).
- [46] The nature of the liquid-vapour interface and other topics in the statistical mechanics of non-uniform, classical fluids, R. Evans, Adv. Phys. **28**, 143 (1979).
- [47] Dynamic density functional theory of fluids, U. M. B. Marconi and P. Tarazona, J. Chem. Phys. **110**, 8032 (1999).
- [48] Dynamical density functional theory and its application to spinodal decomposition, A. J. Archer and R. Evans, J. Chem. Phys. **121**, 4246 (2004).
- [49] Keep-Left Behavior Induced by Asymmetrically Profiled Walls, C. L. Oliveira, A. P. Vieira, D. Helbing, J. S. Andrade, and H. J. Herrmann, Phys. Rev. X **6**, 011003 (2016).
- [50] Floating nematic phase in colloidal platelet-sphere mixtures, D. de las Heras, N. Doshi, T. Cosgrove, J. Phipps, D. I. Gittins, J. S. van Duijneveldt, and M. Schmidt, Sci. Rep. **2**, 789 (2012).
- [51] Phase stacking diagram of colloidal mixtures under gravity, D. de las Heras and M. Schmidt, Soft Matter **9**, 8636 (2013).
- [52] Dynamical density functional theory analysis of the laning instability in sheared soft matter, A. Scacchi, A. J. Archer, and J. M. Brader, Phys. Rev. E **96**, 062616 (2017).
- [53] Nonequilibrium phase transitions of sheared colloidal microphases: Results from dynamical density functional theory D. Stopper and R. Roth, Phys. Rev. E **97**, 062602 (2018).
- [54] Theory of the Two- and One-Dimensional Rigid Sphere Fluids, E. Helfand, H. L. Frisch, and J. L. Lebowitz, J. Chem. Phys. **34**, 1037 (1961).
- [55] J.-P. Hansen and I. R. McDonald, *Theory of Simple Liquids*, 4th ed. (Academic Press, London, 2013).



Cite this: *Soft Matter*, 2018, 14, 9411

Received 12th September 2018,
Accepted 5th November 2018

DOI: 10.1039/c8sm01867g

rsc.li/soft-matter-journal

Crossover from three- to six-fold symmetry of colloidal aggregates in circular traps

T. Geigenfeind,^a C. S. Dias,^{id}*^{bc} M. M. Telo da Gama,^{bc} D. de las Heras^{id}^a and N. A. M. Araújo^{id}^{bc}

At sufficiently low temperatures and high densities, repulsive spherical particles in two-dimensions (2d) form close-packed structures with six-fold symmetry. By contrast, when the interparticle interaction has an attractive anisotropic component, the structure may exhibit the symmetry of the interaction. We consider a suspension of spherical particles interacting through an isotropic repulsive potential and a three-fold symmetric attractive interaction, confined in circular potential traps in 2d. We find that, due to the competition between the interparticle and the external potentials, the particles self-organize into structures with three- or six-fold symmetry, depending on the width of the traps. For intermediate trap widths, a core-shell structure is formed, where the core has six-fold symmetry and the shell is three-fold symmetric. When the width of the trap changes periodically in time, the symmetry of the colloidal structure also changes, but it does not necessarily follow that of the corresponding static trap.

1 Introduction

The control over the self-organization of colloidal particles is a problem of both fundamental and practical interest.^{1–10} One promising approach is the use of chemically or otherwise patterned substrates, where the particle-substrate interaction is spatially dependent and may even change with time. Spatial patterns on substrates may be created using, for example, lithographic methods,^{11,12} magnetic domains,^{13,14} chemical coating,^{15–17} or DNA-mediated functionalization of interfaces.¹⁸

It has been shown that the equilibrium phases of colloidal particles are affected strongly by substrates with spatial patterns. For example, patterns may induce new surface phases¹⁹ and crystalline structures,²⁰ or affect the wetting properties of the surfaces.²¹ The collective (non-equilibrium) dynamical properties are also affected. For example, in the limit of irreversible adsorption, a simple pattern of pits distributed in a square-lattice arrangement induces either local or long-range order, depending on the size of the pits and the distance between them.²²

For simplicity, most of the previous works have considered isotropic particles but, in general, the interparticle interaction is anisotropic. Anisotropy may result, for example, from the

individual particle shape,^{23–27} heterogeneous distribution of charges,^{28–30} or functionalization of the particle surface.^{31–41} In these cases, the final structures should depend not only on the symmetries of the pattern but also on those of the interparticle potential. In a recent study the equilibrium properties of particles with three-fold symmetric attractive interaction adsorbed on patterned substrates were considered.⁴² The properties of the pattern strongly affect both the percolation properties and the type of network in which the particles self-assemble.

Here, we investigate how the dynamics of self-organization of colloidal particles with anisotropic interparticle interactions is affected by the presence of spatial patterns. These patterns result from a square lattice arrangement of (Gaussian) attractive traps with a characteristic width on an otherwise flat substrate. We show that, the structure of the colloidal aggregates, on the substrate, depends strongly on the width of the traps. We consider also traps with a time dependent width and show that the dynamics may differ significantly from that of the static traps.

We introduce the model and the relevant parameters in Section 2. In Section 3 we present the results and we draw some conclusions in Section 4.

2 Model

We consider a monodisperse suspension of spherical (colloidal) particles, where the particle-particle interaction is a superposition of an isotropic repulsion and a three-fold symmetric attraction. Following ref. 43, we describe this pairwise interaction by

^a *Theoretische Physik II, Physikalisches Institut, Universität Bayreuth, D-95440 Bayreuth, Germany*

^b *Departamento de Física, Faculdade de Ciências, Universidade de Lisboa, 1749-016 Lisboa, Portugal. E-mail: csdias@fc.ul.pt*

^c *Centro de Física Teórica e Computacional, Universidade de Lisboa, 1749-016 Lisboa, Portugal*

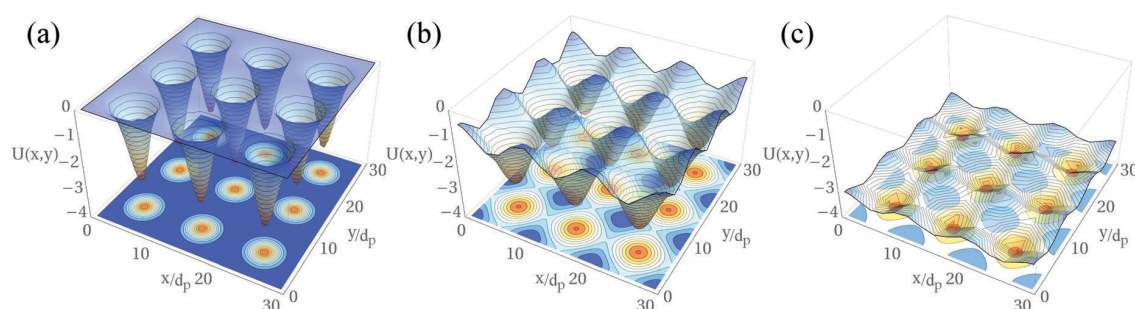


Fig. 1 Schematic representation of the attractive Gaussian potential traps distributed in a square-lattice arrangement. The traps are separated by a distance of ten particle diameters (d_p) and have a width (a) $R_W = 2$, (b) $R_W = 4$, and (c) $R_W = 6$ in units of the particle diameter (d_p). The potential strength is in units of ε .

decorating the surface of the spherical particles with three patches distributed along the equator. The patch–patch attractive interaction has a Gaussian form given by,

$$U_{\text{patch/patch}}(r_p) = -\varepsilon \exp[-(r_p/\sigma)^2], \quad (1)$$

where r_p is the distance between the center of the patches, ε is the interaction strength that sets the energy scale, and $\sigma = 0.1$ the width of the Gaussian in units of the effective particle diameter d_p (which sets the length scale).

The core–core interaction is repulsive and given by,

$$U_{\text{part/part}}(r) = \frac{A}{k} \exp[-k(r - d_p)], \quad (2)$$

where r is the distance between the center of the particles, $A = 0.25$ (in units of ε/d_p), and $k = 0.4$ is the screening length (in units of d_p).

To confine the particles to the surface of a planar substrate, we implemented the method described in ref. 43. The surface pattern consists of attractive potential traps, distributed in a square-lattice arrangement (see Fig. 1), with a Gaussian form,

$$U_{\text{part/trap}}(r) = -3\varepsilon \exp[-(r/R_W)^2], \quad (3)$$

where ε is the strength of the patch–patch interaction (see eqn (1)) and R_W is the width (range) of the trap. The potential is truncated at a distance of 10 particle diameters (d_p) from the center of the trap. As shown in Fig. 1, although the minimum of the traps is kept fixed, the effective potential landscape depends not only on R_W , but also on the distance between the center of the traps, as in some regions the particles interact simultaneously with more than one trap. Since the particle–trap interaction is always attractive, this implies that the net force acting on a particle is lower if the traps overlap. We impose periodic boundary conditions along the x - and y -directions. This pattern can be realized experimentally, for instance, using a setup of multiple optical tweezers arranged on a square array, by passing a laser beam through diffractive optical elements.⁴⁴

To resolve the trajectory of individual particles, we perform Langevin dynamics using the Large-scale Atomic/Molecular Massively Parallel Simulator (LAMMPS).⁴⁵ Particles are spherical with mass m and inertia I and the patches on their surface have negligible mass. The translational and rotational motion of the

particles is described by the following equations,

$$m\dot{\vec{v}}_i(t) = -\nabla_{\vec{r}_i} U - \frac{m}{\tau_t} \vec{v}_i(t) + \sqrt{\frac{2mk_B T}{\tau_t}} \vec{\zeta}_t^i(t), \quad (4)$$

and

$$I\dot{\vec{\omega}}_i(t) = -\nabla_{\vec{\theta}_i} U - \frac{I}{\tau_r} \vec{\omega}_i(t) + \sqrt{\frac{2Ik_B T}{\tau_r}} \vec{\zeta}_r^i(t), \quad (5)$$

where, \vec{v}_i and $\vec{\omega}_i$ are the translational and angular velocities of particle i . The translational and rotational damping times are given by $\tau_t = 0.02 \sqrt{(md_p^2/\varepsilon)}$ and $\tau_r = 10\tau_t/3$ for spherical colloids. $\vec{\zeta}_t^i(t)$ and $\vec{\zeta}_r^i(t)$ are stochastic terms taken from a truncated random distribution of zero mean and standard deviation of one unit.⁴⁶ U is the total potential with contributions from the particle–particle and particle–trap interactions, and therefore it depends on both the positions \vec{r}_i and orientations $\vec{\theta}_i$ of all particles $i = 1 \dots N$ in the system. Note that, although the particles are on a planar substrate, they can still rotate in three dimensions.

3 Results

Particles are initially distributed, without overlapping, uniformly at random on the substrate with a given particle number density ρ , defined as the number of particles per unit volume. Simulations were performed at a reduced temperature $T^* = k_B T/\varepsilon$, where T is the thermostat temperature, ε the strength of the patch–patch interaction and k_B the Boltzmann constant. Unless otherwise stated, we rescale the time by the Brownian time $\tau_B = d_p^2/D_t$, where D_t is the translational diffusion coefficient $D_t = k_B T \tau_t/m$. τ_B is related to the typical time taken by a particle to diffuse in an area d_p^2 , considering an overdamped regime.⁴⁷ All results are averages over (i) 10 different realizations and (ii) all traps in each realization.

To evaluate the local structure formed by the colloidal particles, we measure the local k -fold bond order parameter of the i -th particle,⁴⁸

$$\phi_{k=\{3,6\}}^{(i)} = \left| \frac{1}{\max\{N_i, k\}} \sum_{j=1}^{N_i} e^{-ik\theta_{ij}} \right|, \quad (6)$$

where N_i is the number of neighbors around the particle within a cut-off radius $r_{\text{cut}} = 13$ in units of the particle diameter (d_p). θ_{ij} is the angle between the vector connecting particles i and j and the x -direction (parallel to the substrate). k is a parameter related to the local symmetry such that, ϕ_6 is one for perfect six-fold symmetry and ϕ_3 is one for perfect three-fold symmetry. We then define n_k as the fraction of particles with a value of ϕ_k above a specific threshold that we set to 1/2.

In what follows, we analyze first the dynamics at a temperature $T^* = 0.0625$ which is below the 3D⁴⁹ and 2D⁵⁰ gas-liquid critical temperature (note that the 2D bulk phase diagram may be the most relevant for our system). Then, we consider traps with a time-dependent width at temperatures $T^* = \{0.0625, 0.075, 0.1, 0.125\}$, corresponding to a range of temperatures encompassing the limits of irreversible and reversible bonds.

3.1 Constant potential traps

Fig. 2 shows the time evolution of the fraction of particles with a local (a) three- (n_3) and (b) six-fold (n_6) symmetry, for different values of the width of the traps ($R_W = 2, 4$ and 6) but the same initial particle number density $\rho = 0.25$. This density was chosen to be well below the six-fold equilibrium configuration and also below the percolation threshold taken from ref. 42.

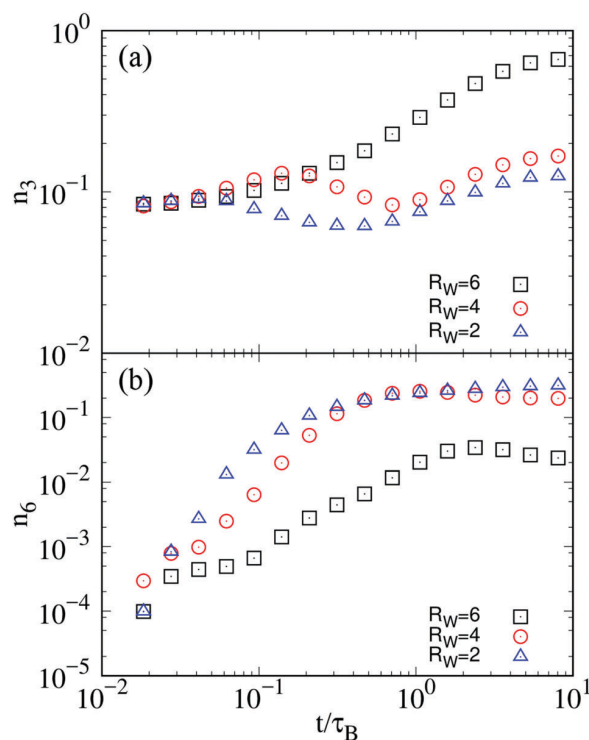


Fig. 2 Time dependence of the fraction of particles with a local (a) three- (n_3) and (b) six-fold (n_6) bond order parameter above 1/2 for different traps with different widths, namely, $R_W = \{2, 4, 6\}$. Simulations are performed on a substrate of linear size $L = 40$ (in units of the particle diameter d_p). The expected values of n_6 for isotropic colloids (no patches) and traps of width $R_W = \{2, 4, 6\}$ are, respectively, $n_6 = \{0.47, 0.40, 0.04\}$.

Let us focus on the case $R_W = 6$ (squares), which is the largest value that we have considered. Both n_3 and n_6 increase in time as the particles accumulate in the potential traps. However, the asymptotic value of n_3 is about two orders of magnitude larger than n_6 , as most particles have a local three-fold symmetry, in line with the symmetry of the patch-patch attractive potential. By contrast, when the width of the trap is reduced, the values of n_3 and n_6 are comparable. For $R_W = 2$, the fraction of particles with a local six-fold symmetry is even larger than that of particles with a three-fold symmetry (*i.e.*, $n_6 > n_3$). This can be explained by the following mechanism. Due to the particle-trap interaction, particles are dragged towards the center of the potential traps, increasing the local density there. The dragging forces are stronger at lower values of R_W (see eqn (3)). Thus, while for $R_W = 6$ the symmetry of the aggregates resembles that of the particle-particle attractive potential, at a lower pressure that corresponds to a lower packing, for $R_W = 2$, the attractive particle-trap forces favor an increase in the local density (packing), with a corresponding increase of the local pressure in the region of the trap, leading to the emergence of the six-fold symmetry.

Fig. 2 shows that the dynamics for traps with $R_W = 4$ exhibits a non-monotonic behavior of n_3 . Fig. 3 depicts snapshots of the

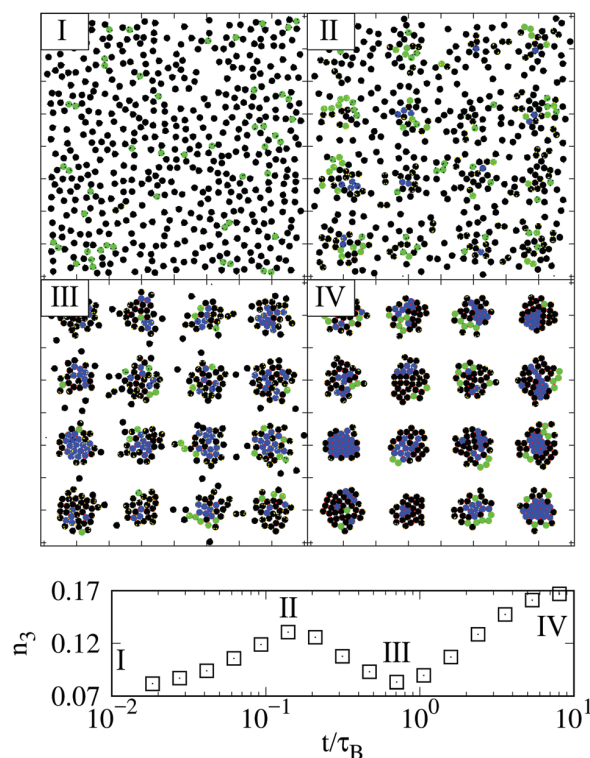


Fig. 3 Bottom: Time dependence of the fraction of particles (n_3) with a local three-fold bond order parameter above 1/2 for traps with $R_W = 4$ and particle number density $\rho = 0.25$. Simulations are performed on a substrate of linear size $L = 40$. Top: Snapshots of the structure at different times (as marked in the bottom plot). Blue and green particles have a local six- and three-fold bond order parameter above 1/2, respectively. In black are the particles with none of the two local bond order parameters above the threshold.

structure at different instants, as pointed out in the plot in the bottom of the same figure. Initially (in I), the particles are randomly distributed in space, without overlapping. As the potential traps are switched on, the particles are dragged towards the center of the traps, establishing bonds with other particles. The value of n_3 increases (from I to II), since the particle–particle attractive interaction favors three bonds per particle (green particles). As more particles are attracted to the traps (from II to III), the fraction of particles with six neighbors in the center of the trap (blue particles) increases and the value of n_3 decreases. As the aggregates grow (from III to IV), the outer particles are under weaker trap forces than the inner ones, favoring again the particle–particle bonds over packing.

When $R_W = 4$, the increase in n_6 is in fact a transient. As shown in Fig. 4, although n_6 initially increases due to packing, it eventually decreases at longer times. Particles in the aggregates relax slowly to form domains with six-fold symmetry with strong particle–particle bonds along the grain boundaries (see inset of Fig. 4). As a result, the fraction of particles with six-fold symmetry is reduced and the value of ϕ_k for a large fraction of the particles is below the threshold for both $k = 3$ and 6.

Fig. 5 shows the number density (ρ) of particles around the center of the trap for $R_W = 4$. Fig. 5(a) and (b) show $\rho(r, n_3)$ and

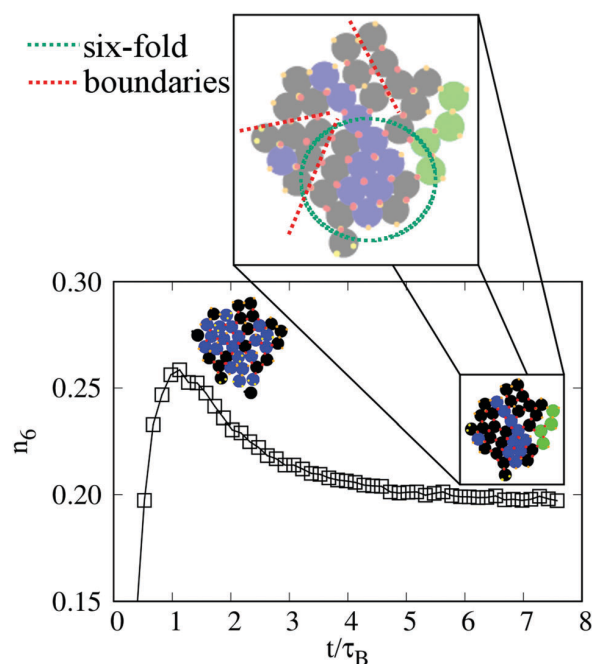


Fig. 4 Time dependence of the fraction of particles (n_6) with a local six-fold bond order parameter above 1/2 for traps with $R_W = 4$ and particle number density $\rho = 0.25$. Simulations are performed on a substrate of linear size $L = 40$. Snapshots are examples of clusters at the point where the maximum occurs (left) and at the end of the simulation (right). Blue and green particles have a local six- and three-fold bond order parameter above 1/2, respectively. In black are the particles where none of the two local order parameters are above threshold. The zoomed region at the top shows the lines of defects (red-dotted line) between six-fold regions (green-dotted line).

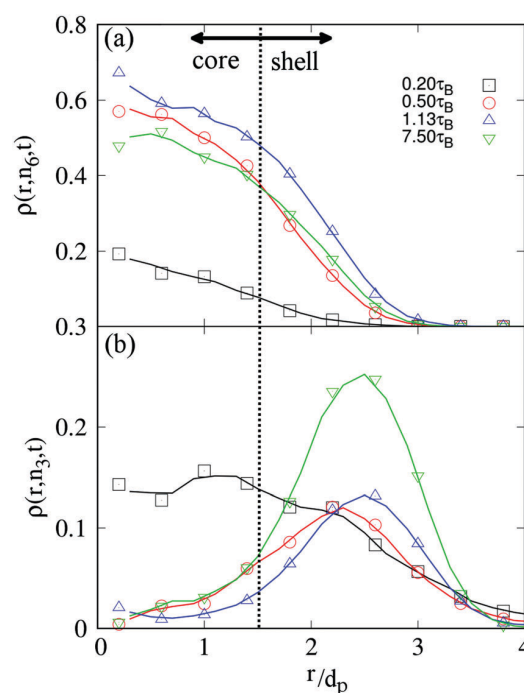


Fig. 5 (a) Number density of particles with a local six-fold bond order parameter above 1/2, measured from the center of the traps at times $t = \{0.20, 0.50, 1.13, 7.50\}\tau_B$. (b) Number density of particles with a local three-fold bond order parameter above 1/2, measured from the center of the traps at times $t = \{0.20, 0.50, 1.13, 7.50\}\tau_B$. Solid lines are averages over neighboring points on the left and right to show the overall tendency. Simulations were performed on a square substrate of size $L = 40$.

$\rho(r, n_6)$, respectively. Note that the maxima of n_3 and n_6 occur at different positions. This difference corroborates the hypothesis that the local three- and six-fold symmetric structures are formed in different regions. In the center of the trap, the particles self-organize (pack) with six-fold symmetry, while in the perimeter most particles form three bonds with other particles. The time evolution of the radial distribution function shows that, at early times, both structures form near the center of the trap independently. As time evolves, a separation of the structures is observed, with the six-fold structure in the center of the trap and the three fold one in the perimeter. Asymptotically, the six-fold peak of the radial distribution function decreases slightly due to the rearrangement discussed above.

3.2 Time-dependent potential traps

The results reported above suggest the design of a device, where the symmetry of the aggregates may be dynamically switched from three to six fold through the width of the potential traps. The effectiveness of such a device, however, depends on how the rate of the symmetry change compares to the different timescales involved, namely those related to bond breaking/formation and rotational/translational diffusion.^{47,51}

We considered time dependent trap widths, as shown in Fig. 6(a). We start with traps with $R_W = 2$ and periodically increase R_W linearly to $R_W = 6$ and then reduce it back (linearly)

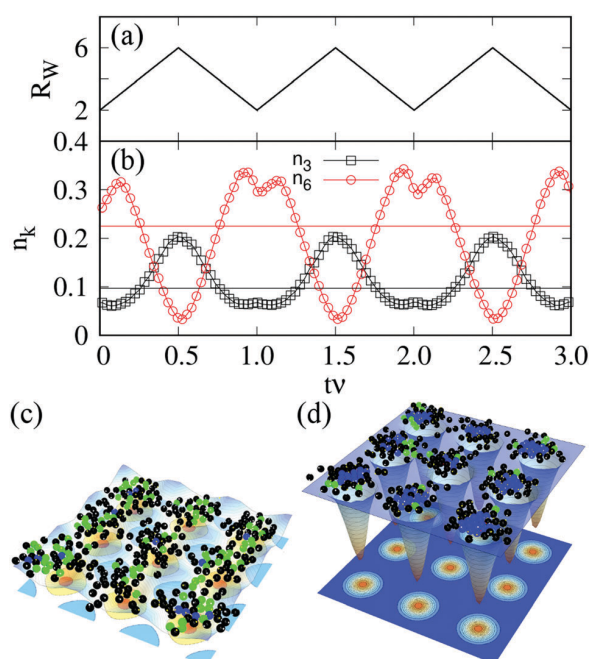


Fig. 6 (a) Time dependent width of the potential traps (R_W) that varies periodically between two and six. (b) Time dependence of the fraction of particles (n_k) with a local six-fold and (n_3) three-fold bond order parameter above $1/2$ for traps with the same oscillating width R_W , particle number density $\rho = 0.3$, and reduced temperature $T^* = 0.125$. Here, time is rescaled in units of the period of the oscillation. Simulations are performed on a square substrate of size $L = 40$. The solid line is the equilibrium order parameter for a potential of constant width $R_W = 4$. Simulation snapshots at the two limiting potential widths (c) $R_W = 6$ and (d) $R_W = 2$ for the oscillating traps. Blue and green particles have a local six- and three-fold bond order parameter above $1/2$, respectively. In black are the particles where none of the two local order parameters are above the threshold.

to $R_W = 2$. Let us discuss the dynamics at $T^* = 0.125$, the highest temperature considered here, here the oscillations have a period $\nu^{-1} = 20\tau_B$. In Fig. 6(b) we plot the fraction of particles with a local six- and three-fold symmetry, as a function of time. Here, for convenience, time is rescaled in units of the period of the oscillation of R_W (ν^{-1}). At this temperature, the local structure oscillates between three-fold and six-fold symmetry, with the same frequency and phase of R_W (see snapshots Fig. 6(c) and (d)). A local minimum in n_6 is observed at $R_W = 2$ indicating that the optimal width of the trap to promote local six-fold symmetry is around three particle diameters (d_p).

Fig. 7(b) shows the time dependence of n_6 (black squares) for the same oscillating R_W at a slightly lower temperature ($T^* = 0.1$). In this case, n_6 oscillates with a period $\nu^{-1} = 16\tau_B$, but the phase is shifted by approximately $1/4$ of the period. To investigate the dependence on the initial conditions, we applied the same oscillating trap R_W , starting at $R_W = 6$ (red circles in Fig. 7). The same shift is observed, and the periodic behavior at longer times is clearly independent of the initial conditions.

When the temperature is reduced further, namely, $T^* = \{0.0625, 0.075\}$ (corresponding to periods of $\nu^{-1} = \{10, 12\}\tau_B$), we observed a similar shift in the (weaker) oscillations and a marked dependence

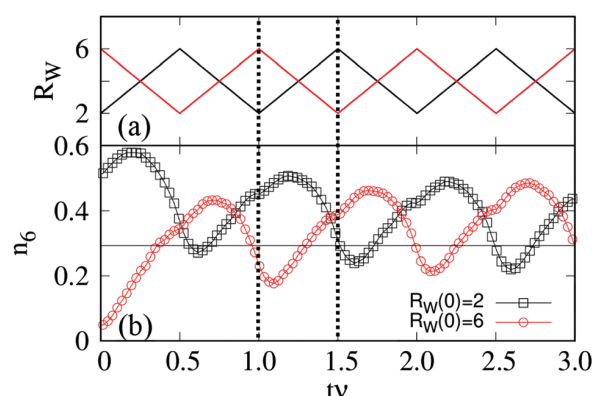


Fig. 7 (a) Time dependent width of the potential traps (R_W) which varies periodically between two to six. (b) Time dependence of the fraction of particles (n_6) with a local six-fold bond order parameter above $1/2$ for oscillating traps with initial widths $R_W(0) = 2$ (squares) and $R_W(0) = 6$ (circles) for a particle number density $\rho = 0.3$ and reduced temperature $T^* = 0.1$. Here, time is rescaled in units of the period of the oscillation. Simulations are performed on a square substrate of size $L = 40$. The solid line gives the equilibrium order parameter for a fixed potential of $R_W = 4$.

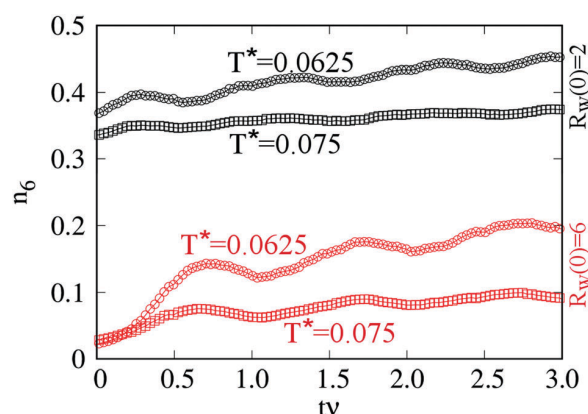


Fig. 8 Time dependence of the fraction of particles (n_6) with a local six-fold bond parameter above $1/2$ for traps with R_W varying periodically from two to six with initial trap widths $R_W(0) = 2$ and $R_W(0) = 6$ (same as Fig. 7(a)) and reduced temperatures $T^* = 0.0625$ (squares) and $T^* = 0.075$ (circles), for a particle number density $\rho = 0.3$. Here, time is rescaled in units of the period of the oscillation. Simulations are performed on a square substrate of size $L = 40$.

on the initial conditions. This is shown in Fig. 8, at different temperatures (different symbols) and initial conditions (top and bottom curves, respectively). The timescales of the relaxation mechanisms (bond break/formation and translation/rotational diffusion) depend strongly on temperature. Thus, at sufficiently low temperatures, the rate of change of R_W is too fast preventing the particles to relax to the structures expected for the corresponding static traps R_W .

4 Conclusions

We have studied the dynamics of spherical colloidal particles on a surface in the presence of circular potential traps. The attractive

interaction between the particles has three-fold symmetry. However, in the presence of potential traps, we observe a crossover from the expected local three-fold symmetry to a six-fold one when the width of the traps is reduced. For intermediate values of the trap width, we find a core-shell structure, where the symmetry in the core is six fold, while that in the shell is three fold. Note that, for a fixed distance between the centers of the traps, increasing the width of the traps corresponds to smoothing out the external potential landscape. Thus, we expect similar results when the strength of the potential is changed, at fixed width.

For traps with oscillating widths, we find that the final structure may deviate significantly from the thermodynamic one, when the relaxation timescales are comparable to the period of the oscillations. In this limit, the final structures depend on the rate of change of the trap width, the thermostat temperature, and the initial conditions.

Conflicts of interest

There are no conflicts to declare.

Acknowledgements

This work was partially funded by the Portuguese German FCT/DAAD project “Self-organization of colloidal particles on patterned substrates” (DAAD project id: 57339919). We also acknowledge financial support from the Portuguese Foundation for Science and Technology (FCT) under Contracts no. PTDC/FIS-MAC/28146/2017, UID/FIS/00618/2013, and SFRH/BPD/114839/2016.

References

- 1 S. Sacanna and D. J. Pine, *Curr. Opin. Colloid Interface Sci.*, 2011, **16**, 96.
- 2 Q. Chen, S. C. Bae and S. Granick, *Nature*, 2011, **469**, 381.
- 3 F. Romano and F. Sciortino, *Nat. Mater.*, 2011, **10**, 171.
- 4 D. Nykypanchuk, M. M. Maye, D. van der Lelie and O. Gang, *Nature*, 2008, **451**, 549.
- 5 W. J. Parak, *Science*, 2011, **334**, 1359.
- 6 S.-M. Yang, S.-H. Kim, J.-M. Lim and G.-R. Yi, *J. Mater. Chem.*, 2008, **18**, 2177.
- 7 E. M. Furst, *Proc. Natl. Acad. Sci. U. S. A.*, 2011, **108**, 20853.
- 8 V. N. Manoharan, *Science*, 2015, **349**, 1253751.
- 9 E. Duguet, A. Désert, A. Perro and S. Ravaine, *Chem. Soc. Rev.*, 2011, **40**, 941.
- 10 C. S. Dias, N. A. M. Araújo and M. M. Telo da Gama, *Adv. Colloid Interface Sci.*, 2017, **247**, 258.
- 11 I. B. Ramsteiner, K. E. Jensen, D. A. Weitz and F. Spaepen, *Phys. Rev. A: At., Mol., Opt. Phys.*, 2009, **79**, 011403.
- 12 D. Wang and H. Möhwald, *J. Mater. Chem.*, 2004, **14**, 459.
- 13 P. Tierno and T. M. Fischer, *Phys. Rev. Lett.*, 2014, **112**, 048302.
- 14 J. Loehr, D. de las Heras, A. Jarosz, M. Urbaniak, F. Stobiecki, A. Tomita, R. Huhnstock, I. Koch, A. Ehresmann, D. Holzinger and T. M. Fischer, *Commun. Phys.*, 2018, **1**, 4.
- 15 J. Aizenberg, A. J. Black and G. M. Whitesides, *Nature*, 1999, **398**, 495.
- 16 K. M. Chen, X. Jiang, L. C. Kimerling and P. T. Hammond, *Langmuir*, 2000, **16**, 7825.
- 17 Q. Guo, C. Arnoux and R. E. Palmer, *Langmuir*, 2001, **17**, 7150.
- 18 D. Joshi, D. Bargteil, A. Caciagli, J. Burelbach, Z. Xing, A. S. Nunes, D. E. P. Pinto, N. A. M. Araújo, J. Bruijck and E. Eiser, *Sci. Adv.*, 2016, **2**, e1600881.
- 19 M. Heni and H. Löwen, *Phys. Rev. Lett.*, 2000, **85**, 3668.
- 20 H. M. Harreis, M. Schmidt and H. Löwen, *Phys. Rev. E: Stat., Nonlinear, Soft Matter Phys.*, 2002, **65**, 041602.
- 21 C. Bauer and S. Dietrich, *Phys. Rev. E: Stat., Nonlinear, Soft Matter Phys.*, 1999, **60**, 6919.
- 22 A. Cadilhe, N. A. M. Araújo and V. Privman, *J. Phys.: Condens. Matter*, 2007, **19**, 065124.
- 23 S. Sacanna, D. J. Pine and G.-R. Yi, *Soft Matter*, 2013, **9**, 8096.
- 24 J. R. Wolters, G. Avvisati, F. Hagemans, T. Vissers, D. J. Kraft, M. Dijkstra and W. K. Kegel, *Soft Matter*, 2015, **11**, 1067.
- 25 S. C. Glotzer, *Nature*, 2012, **481**, 450.
- 26 P. J. Yunker, M. A. Lohr, T. Still, A. Borodin, D. J. Durian and A. G. Yodh, *Phys. Rev. Lett.*, 2013, **110**, 035501.
- 27 C. S. Dias, P. J. Yunker, A. G. Yodh, N. A. M. Araújo and M. M. Telo da Gama, *Soft Matter*, 2018, **14**, 1903.
- 28 P. Ilg and E. D. Gado, *Soft Matter*, 2011, **7**, 163.
- 29 A. Nych, U. Ognysta, M. Skarabot, M. Ravnik, S. Zumer and I. Muševič, *Nat. Commun.*, 2013, **4**, 1489.
- 30 S. H. L. Klapp, *Curr. Opin. Colloid Interface Sci.*, 2016, **21**, 76.
- 31 Y. Wang, Y. Wang, D. R. Breed, V. N. Manoharan, L. Feng, A. D. Hollingsworth, M. Weck and D. J. Pine, *Nature*, 2012, **491**, 51.
- 32 F. Smalenburg, L. Leibler and F. Sciortino, *Phys. Rev. Lett.*, 2013, **111**, 188002.
- 33 E. Bianchi, G. Kahl and C. N. Likos, *Soft Matter*, 2011, **7**, 8313.
- 34 C. S. Dias, N. A. M. Araújo and M. M. Telo da Gama, *EPL*, 2014, **107**, 56002.
- 35 S. Sokołowski and Y. V. Kalyuzhnyi, *J. Phys. Chem. B*, 2014, **118**, 9076.
- 36 E. Słyk, W. Rzyśko and P. Bryk, *Soft Matter*, 2016, **12**, 9538.
- 37 G.-R. Yi, D. J. Pine and S. Sacanna, *J. Phys.: Condens. Matter*, 2013, **25**, 193101.
- 38 Z. He and I. Kretzschmar, *Langmuir*, 2012, **28**, 9915.
- 39 D. J. Kraft, J. Hilhorst, M. A. P. Heinen, M. J. Hoogenraad, B. Luijckes and W. K. Kegel, *J. Phys. Chem. B*, 2011, **115**, 7175.
- 40 M. E. Cates, *Nat. Mater.*, 2013, **12**, 179.
- 41 T. Geigenfeind and D. de las Heras, *J. Phys.: Condens. Matter*, 2017, **29**, 064006.
- 42 L. L. Treffenstädt, N. A. M. Araújo and D. de las Heras, *Soft Matter*, 2018, **14**, 3572.

- 43 C. S. Dias, C. Braga, N. A. M. Araújo and M. M. Telo da Gama, *Soft Matter*, 2016, **12**, 1550.
- 44 E. R. Dufresne and D. G. Grier, *Rev. Sci. Instrum.*, 1998, **69**, 1974.
- 45 S. Plimpton, *J. Comp. Physiol.*, 1995, **117**, 1.
- 46 B. Dunweg and P. Wolfgang, *Int. J. Mod. Phys. C*, 1991, **2**, 817.
- 47 C. S. Dias, N. A. M. Araújo and M. M. Telo da Gama, *J. Phys.: Condens. Matter*, 2018, **30**, 014001.
- 48 A. S. Nunes, A. Gupta, N. A. M. Araújo and M. M. Telo da Gama, *Mol. Phys.*, 2018, **116**, 3224.
- 49 C. S. Dias, J. M. Tavares, N. A. M. Araújo and M. M. Telo da Gama, *Soft Matter*, 2018, **14**, 2744.
- 50 P. Tartaglia and F. Sciortino, *J. Phys.: Condens. Matter*, 2010, **22**, 104108.
- 51 J. M. Tavares, C. S. Dias, N. A. M. Araújo and M. M. Telo da Gama, *J. Phys. Chem. B*, 2018, **122**, 3514.